Structure and physical properties of silicon clusters and of vacancy clusters in bulk silicon

zur Erlangung des akademischen Grades
doctor rerum naturalium (Dr. rer. nat.)

vom

FACHBEREICH PHYSIK
der UNIVERSITÄT PADERBORN

genehmigte

DISSERTATION

von Dipl. Phys. Alexander Sieck

Eingereicht am 27. Juli 2000

Bibliographische Beschreibung und Inhaltsangabe

SIECK, ALEXANDER
Structure and physical properties of silicon clusters and of vacancy clusters in bulk silicon
Universität Paderborn, Fachbereich für Physik
Dissertation, 2000 (in englischer Sprache)
143 Seiten, 49 Abbildungen, 19 Tabellen, 138 Literaturzitate

In dieser Arbeit wird der Wachstumsprozess von freien Silizium Clustern und von Leerstellen-Clustern in kristallinem Silizium untersucht. Das Ziel ist u.a. den Übergang vom Cluster über Nanostrukturen bis zum Festkörper zu beschreiben und zu verstehen. Im Bereich zwischen Clustern und Festkörpern treten Silizium Strukturen mit neuen interessanten physikalischen Eigenschaften auf. Die Identifikation der Struktur und Funktion von Silizium Clustern ist nur durch eine Kombination von Theorie und Experiment möglich. Mittels verschiedener Optimierungsstrategien und einer auf Dichtefunktional-Theorie basierten "Tight-Binding" Methode werden Cluster-Strukturen mit besonders niedriger Bindungsenergie bestimmt. Für die stabilsten kleineren Cluster werden die Infrarot- und Raman-Spektren, sowie deren Polarisierbarkeiten im Rahmen selbst-konsistenter Dichtefunktional-Theorie berechnet. Für Cluster mit 25 bis 35 Atomen wird die Form der Cluster und deren Beweglichkeit in He-Gas analysiert. Die bei niedrigen Temperaturen im Experiment beobachteten Cluster werden anschließend anhand der Übereinstimmung von berechneten Eigenschaften mit den experimentellen Daten identifiziert. Silizium Cluster mit 10 bis 15 Atomen haben ein dreifach-gekapptes trigonales Prisma als gemeinsame Untereinheit. Bis zu Clustern mit etwa 25 Atomen geht der Wachstumsprozeß über prolate Strukturen. Im Bereich von 24- bis 30-atomigen Clustern verändert sich die Geometrie hin zu kompakten sphärischen Strukturen. Niedrig-energetische Cluster bestehend aus bis zu 240 Atomen weisen ein Bindungsmuster auf, das sehr stark von dem des Festkörpers abweicht. Dadurch weichen auch die elektrischen und optischen Eigenschaften der Strukturen mit Abmessungen im Ångström Bereich von denen im Festkörper ab. Die Berechnung der Stabilität verschiedener Leerstellen-Cluster in kristallinem Silizium und der zugehörigen Positronen-Lebensdauern weisen darauf hin, daß die in bestrahltem Silizium gemessenen Positronen-Lebensdauern von ca. 435 ps zu Clustern bestehend aus 9 oder 10 Leerstellen gehören. Die Leerstellen in diesen Clustern bilden benachbarte Sechser-Ringe und weisen somit eine minimale Anzahl hängender Bindungen auf.

Schlagwörter

Silizium Cluster, Leerstellen-Cluster, Dichtefunktional-Theorie, Tight-Binding, Infrarot-Spektrum, Raman-Spektrum, Beweglichkeiten, Positronen-Lebensdauern

Abstract

In this thesis the growth-pattern of free silicon clusters and vacancy clusters in bulk silicon is investigated. The aim is to describe and to better understand the cluster to bulk transition. Silicon structures in between clusters and solids feature new interesting physical properties. The structure and physical properties of silicon clusters can be revealed by a combination of theory and experiment, only. Low-energy clusters are determined with different optimization techniques and a density-functional based tight-binding method. Additionally, infrared and Raman spectra, and polarizabilities calculated within self-consistent field density-functional theory are provided for the smaller clusters. For clusters with 25 to 35 atoms an analysis of the shape of the clusters and the related mobilities in a buffer gas is given. Finally, the clusters observed in low-temperature experiments are identified via the best match between calculated properties and experimental data. Silicon clusters with 10 to 15 atoms have a tricapped trigonal prism as a common subunit. Clusters with up to about 25 atoms follow a prolate growth-path. In the range from 24 to 30 atoms the geometry of the clusters undergoes a transition towards compact spherical structures. Low-energy clusters with up to 240 atoms feature a bonding pattern strikingly different from the tetrahedral bonding in the solid. It follows that structures with dimensions of several Angström have electrical and optical properties different from the solid. The calculated stabilities and positron-lifetimes of vacancy clusters in bulk silicon indicate the positron-lifetimes of about 435 ps detected in irradiated silicon to be related to clusters of 9 or 10 vacancies. The vacancies in these clusters form neighboring hexa-rings and, therefore, minimize the number of dangling bonds.

Keywords

silicon clusters, vacancy clusters, density-functional theory, tight-binding, infrared-spectrum, Raman-spectrum, mobilities, positron-lifetimes

Contents

List of Figures

List of Tables

Chapter 1

Introduction and Motivation

1.1 Silicon structures with new physical properties

Silicon (Si) is by far the most important material in the semiconductor industry. Every microprocessor and memory chip in use today is built from silicon. Crystalline and amorphous silicon are widely used in the production of solar-cells. Silicon is semiconducting with an indirect band gap of 1.1 eV and its conductivity can be widely varied by doping. The most common acceptor type is Boron and the most common donator types are Phosphorus and Arsenic. Homo-nuclear silicon systems are much easier to handle than hetero-nuclear compound materials, like Gallium-Arsenide (GaAs) or Gallium-Nitride (GaN). Hence, they are more cost efficient. Silicon can be grown in single crystals more than 1 meter long and 30 cm across, weighting approximately 200 kg. The purity of the crystal and the number of electrically active defects are well under control. Silicon makes up 25.7% of the earths crust by weight, and is the second most abundant element, exceeded only by oxygen. It is found largely as silicon oxides such as sand (silica), quartz and rock crystal. There is normally no need to make silicon in the laboratory as it is readily available commercially. Silicon can be isolated through the treatment of silica, SiO_2, with coke in an electric furnace:

$$\mathrm{SiO_2} + 2\mathrm{C} \rightarrow \mathrm{Si} + 2\mathrm{CO}.$$

Single silicon crystals are grown as *floating-zone* crystals or in a *Czochralsky* process and clusters can be created by laser-vaporization from the solid.

In recent years the number of device components on a single chip has been increased from several hundred in 1970 by a factor of 64,000 to a fully integrated 64 megabit memory chip with more than one hundred million electronic components today (2000). The progress up to now is well described by "Moore's law". Gordon Moore predicted in 1965 that for each new generation of memory chip and microprocessor unit on the market, the device size would reduce by 33%, the chip size would increase by 50%, and the number of components of a chip would quadruple every three years. So far this trend has shown no sign of stopping. The critical device size is predicted to decrease from 200 nm in 1998 to 50 nm in 2012 [1]. A layer 50 nm thick corresponds to roughly 200 monolayers of silicon atoms. It is important to know which influence this down scaling has on the physical properties of the devices. To achieve this one needs to understand the physics on an atomic scale. The solid state structure of silicon is that of the diamond crystal. Every silicon atom is tetrahedrally bonded to four nearest neighbors. The nearest neighbor distance is $2.35\,\text{Å} = 2.35 \cdot 10^{-10}\,\text{m}$. The smallest silicon clusters (with less than 10 atoms) are known to have bonding patterns much different from the diamond structure. To identify the size regime in which the structure becomes different from the ideal crystal either one can investigate nanostructures of decreasing size or the growth pattern of smaller silicon clusters. Until recently, only the geometries of the smallest silicon clusters with up to eight atoms could be determined. The geometrical arrangement of, e.g., 20 silicon atoms at low temperatures was unknown. Still one does not know if a nanoparticle, consisting of several hundred to several thousand silicon atoms, is more closely related to disordered systems, to the (unstable) metallic phases of bulk-silicon, or to the diamond structure. The metallic phases (such as the simple-cubic structure) feature high coordination numbers, whereas the diamond structure and amorphous silicon feature sp^3-hybridized atoms. The geometry of the clusters determines the electronic structure and whether the gap between occupied and non-occupied states resembles that of a metall or that of a semiconductor (see Figure 1.1).

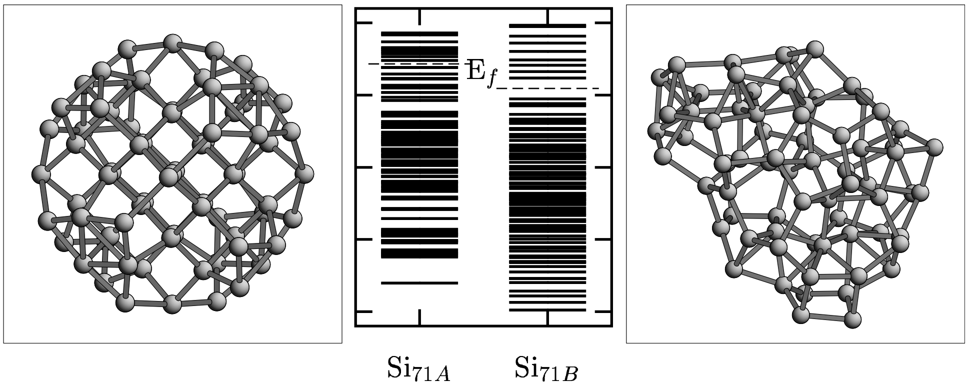

Figure 1.1: Two possible structures for Si_{71}. Si_{71A} (left) resembles the diamond structure, whereas Si_{71B} (right) is compact and disordered. The two geometries feature different electronic structures, and hence different optical properties.

In addition to understanding the cluster → bulk transition, the study of atomic clusters is of great interest for several other reasons. Clusters play a crucial role in a number of industrial applications such as catalysis or in the development of new semiconducting/magnetic devices. The experimental techniques for production and analysis of clusters have improved strongly in recent years, providing new and more accurate data about their electronic, chemical, and structural properties.

Looking at *Fullerenes* (especially stable cage-like structures of carbon), the question arises if similar "magic number" clusters do exist for silicon. Like carbon, silicon has four valence electrons, but because of the larger covalent radius, silicon in general does not form strong π-bonds. The strong π-bonds between carbon atoms in a graphite-plane are responsible for the high stability of graphite. Graphite is slightly more stable than diamond. For silicon, the graphite structure and fullerenes, having bonding patterns similar to a plane in graphite, are not stable. However, other more compact stable clusters are conceivable for silicon. Once remarkably stable silicon clusters, retaining under certain conditions their identity in a solid, are found, one could think of building cluster assembled materials with new unique physical properties. One of the top research goals in semiconductor physics is to find silicon based materials with a large direct band gap. This would allow for the combination of optical and electrical devices on a single chip without significantly changing the manufacturing process. Silicon nanocrystallites have been found to have gap-widths corresponding to absorption and emission lines in the optical spectrum. The gap-width varies with particle size and hence can be tuned to a desired color [2].

To determine the structure and physical properties of clusters a combined approach of theoretical and experimental methods has to be undertaken. The energies of many different structures are calculated to find stable clusters with a low energy. Then suitable physical properties also accessible by experiment are calculated for the lowest-energy clusters and are compared to the experimental data. The ground-state structures can be identified by the best match between theory and experiment. The geometry of a cluster is not directly accessible by experiment, but measured photoelectron, infrared (IR) or Raman spectra provide useful information about the physical properties and, indirectly, about the bonding pattern. The methods of quantum chemistry, developed during the last decades, make it possible to accurately calculate the geometries and energies of small atomic systems. For large systems *first principles* methods become very time consuming even on high performance parallel computers. Additionally, the number of locally stable isomers increases at least exponentially with cluster size. This requires fast approximate methods and statistical optimizing techniques, like "*Simulated Annealing*" or "*Genetic Algorithms*" to determine the lowest-energy isomers for a given cluster size. It turns out that the differences in energy between some low-energy isomers are very small and challenge even the most accurate methods. Therefore, the calculation of additional properties, accessible by experiment, is required. The method of choice depends on the system of interest. For small silicon clusters, photoelectron, IR, and Raman spectra are best suited. For larger clusters with more than 20 atoms the small abundance of clusters makes it difficult to obtain reliable IR and Raman spectra. Today only photoelectron spectra, chemical reactivities, and mobilities in a buffer gas have been measured for larger silicon clusters with up to 50 atoms. Little is known about even larger clusters. The measured mobilities yield information about the rotational-averaged geometrical cross-sections of the clusters. The detailed geometry of the clusters can be revealed by comparing the shape of the calculated low-energy strutures to the cross-sections from experiment.

Besides clusters, defects in crystalline silicon are very important in todays semiconductor research. Although the defect concentration in a silicon crystal is very small in modern production processes, the influence of defects becomes more severe with decreasing device size. Few defects, caused by electron irradiation or thermal treatment in the manufacturing process, may significantly change the physical properties of a device consisting only of several hundred atoms. Mono- and di-vacancies in sil-

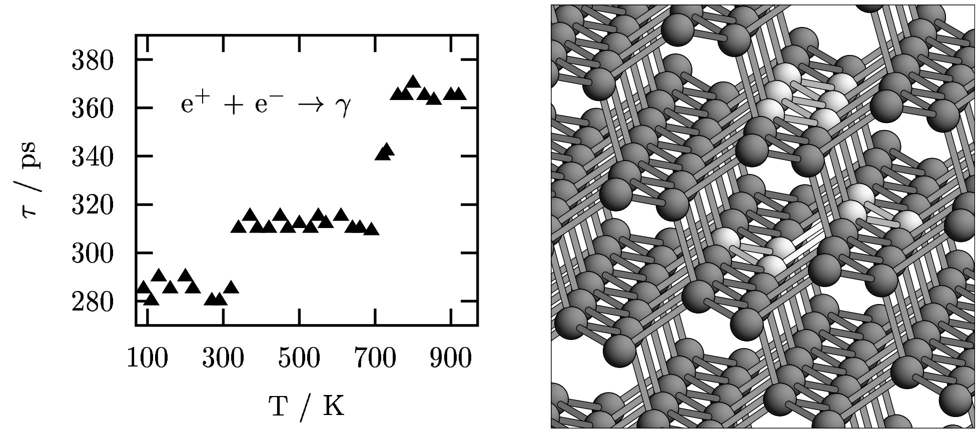

Figure 1.2: Positron annihilation spectroscopy in bulk-silicon indicates the existence of vacancy clusters for different temperature ranges (left). Theory can link the measured positron lifetimes τ to different vacancy structures, such as a zig-zag chain or a "hexagonal-ring" (right, white spheres represent vacancy sites).

icon are well characterized, even if their exact geometry is still debated. Much less is known about the structure of vacancy clusters. Vacancy clusters are assumed to serve as impurity-traps for oxygen or hydrogen. The presence of vacancy clusters is indicated by electron paramagnetic resonance (EPR) or positron annihilation spectroscopy (PAS). The advantage of PAS is that it provides information about the size of a defect. The positron lifetime depends on the electronic charge density at the defect and is longest for very large vacancy clusters. Positron annihilation spectroscopy is sensitive only to neutral or negatively charged defects. In a typical PAS experiment the samples are annealed before measuring the positron lifetimes. The annealing temperatures T give information about the stability of a defect related to a certain positron lifetime. This is schematically depicted in Figure 1.2.

The development of efficient and accurate approximate quantum mechanically methods allows to compute the stability of large silicon clusters and extended vacancy clusters in bulk silicon and to calculate additional physical properties for comparison with experimental data. Understanding the relationship between structure and physical properties is the key to developing new materials and devices.

1.2 Outline

In this thesis different silicon systems are investigated with the computational methods of quantum chemistry. Stable structures of silicon clusters and defects in bulk silicon are identified by comparing the cohesive energies of different geometrical arrangements. To allow for a comparison with experimental data various additional physical properties, infrared (IR) and Raman spectra or mobilities in a buffer gas for clusters and positron lifetimes for vacancy clusters in the bulk, are determined. All the calculations are based on *Density Functional Theory* (DFT), which is described in Chapter 2. To introduce the basic concepts of the theoretical treatment of many-electron systems along with the nomenclature also used in DFT, first the basic method of quantum chemistry, namely the *Hartree-Fock* (HF) method, is described. To treat large systems, as it is necessary for extended defects, or to perform *Molecular Dynamics* (MD) on clusters, an approximate density functional based *Tight-Binding* (DFTB) method is introduced at the end of Chapter 2.

IR and Raman spectroscopy are especially well suited to obtain information about the structure of smaller clusters. To extend density-functional theory to the calculation of IR and Raman spectra an external electric field has to be taken into account. The basic theory how to calculate vibrational frequencies along with IR and Raman spectra is outlined in Chapter 3.

The physical properties of smaller silicon clusters with less than 15 atoms are described in Chapter 4. Up to Si_8, different computational approaches and experiments yield a unique picture on the ground-state structures. For Si_9 to Si_{14} likely candidates for the ground-state are introduced along with their calculated IR and Raman spectra. All energies and intensities are calculated within self-consistent-field DFT. To find low energy structures for silicon clusters with more than 20 atoms a statistical search on many different geometries is necessary. One approach, known to work efficiently and reliable, is *Simulated Annealing.* This optimization technique and the specific parameters used are described in Chapter 5. The Simulated Annealing implemented with DFTB is applied to silicon clusters with 25, 29, and 35 atoms to investigate the experimentally indicated shape transition in this size regime in Chapter 6. The shapes of the lowest energy structures are analyzed and related to the measurements. A brief outlook on larger cluster sizes, namely Si_{71} and Si_{239}, and their bonding schemes compared to the tetrahedral bonding in the ideal diamond structure is presented at the end of this Chapter.

In Chapter 7 the DFTB method is used to compute the stability of vacancy clusters in bulk silicon. The formation and dissociation energies for several clusters consisting of up to 17 vacancies are determined. A simple model which explains the basic features of stable vacancy clusters is developed, as well. To allow for a comparison with experimental data the lifetimes of a positron trapped in a vacancy cluster are calculated. The calculated dissociation energies are related to the measured annealing-temperatures via transition-state theory. The computed energies and positron lifetimes combined with the measured annealing temperatures and lifetimes yield a consistent picture on the growth-process of vacancy clusters.

Appendix A contains a detailed description of the adoption of the DFTB method to silicon systems including results about energies, geometries and the electronic structure of some of the most important silicon structures. A brief summary of *Group-Theory* and its application to vibrational spectra is provided in Appendix B. Finally, model annealing curves obtained from transition-state theory are given in Appendix C.

Chapter 2

Theoretical treatment of many electron systems

Atomic systems with typical distances of several Angstrom ($1\,\text{Å} = 10^{-10}\,\text{m}$) have to be described by quantum theory. The fundamental equation of quantum theory is the *Schrödinger equation*, which describes a quantum mechanically system by a partial differential-equation of second order with respect to the electronic positions and of first order in time. The state of the system is represented by a time-dependent wavefunction, which also depends on the positions of the nuclei and of the electrons. For systems with more than two electrons no exact solution to the Schrödinger equation is known, but several sophisticated algorithms have been developed to obtain numerical solutions. The basic methods in Quantum Chemistry are the Hartree-Fock (HF) method and its extensions. After the introduction of Hartree Fock theory an alternative, but similar, method the Density Functional Theory (DFT) has been developed. In this theory an atomic system is described by its electronic density, in contrast to HF theory where the focus is on the wavefunction. Since both methods, Hartree-Fock and density functional theory, are computationally very demanding even for small systems, approximate methods have been developed to treat larger systems or to perform molecular dynamics. In this Chapter a brief introduction to the Hartree-Fock and density functional theories is provided and an approximate tight-binding method based on DFT is introduced. A detailed description of Hartree-Fock based methods along with useful hints for implementing them on a computer can be found in [3]. An overview of density-functional theory and its applications is given, for instance, in [4].

2.1 Hartree-Fock Theory

An atomic system with no explicit time-dependence consisting of M nuclei and N electrons is determined by the nonrelativistic[1] time-independent Schrödinger equation:

$$\hat{\mathrm{H}}|\Psi\rangle = E|\Psi\rangle. \tag{2.1}$$

---

[1] Relativistic corrections become necessary for heavier atom types.

Here, $\hat{\mathrm{H}}$ is the Hamilton operator of the atomic system and $|\Psi\rangle$ is the wave-function, which defines the state of the nuclei and electrons.

In atomic units, where lengths are given in Bohr (a_{B}) and energies in Hartree (H) with

$$\begin{aligned}
1\,a_{\mathrm{B}} &= \frac{4\pi\varepsilon_0\hbar^2}{m_{\mathrm{e}}e^2} = 0.52918 \cdot 10^{-10}\,\mathrm{m} \\
1\,\mathrm{H} &= m_{\mathrm{e}}\left(\frac{e^2}{4\pi\varepsilon_0\hbar}\right)^2 = 4.3598 \cdot 10^{-18}\,\mathrm{J} \\
&= 27.2114\ \mathrm{eV} = 627.090\ \mathrm{kcal/mol},
\end{aligned}$$

the Hamilton operator $\hat{\mathrm{H}}$ reads:

$$\begin{aligned}
\hat{\mathrm{H}} = &-\sum_{i=1}^{N}\frac{1}{2}\nabla_i^2 - \sum_{i=1}^{N}\sum_{\mu=1}^{M}\frac{Z_\mu}{|\vec{r}_i - \vec{R}_\mu|} + \sum_{i=1}^{N}\sum_{j>i}^{N}\frac{1}{|\vec{r}_i - \vec{r}_j|} \\
&-\sum_{\mu=1}^{M}\frac{m_{\mathrm{e}}}{2M_\mu}\nabla_\mu^2 + \sum_{\mu=1}^{M}\sum_{\nu>\mu}^{M}\frac{Z_\mu Z_\nu}{|\vec{R}_\mu - \vec{R}_\nu|}.
\end{aligned} \tag{2.2}$$

In the above equation $\vec{r}_i$ and $\vec{R}_\mu$ denote the position vectors of the i-th electron and of the μ-th nucleus, respectively. Furthermore, m_{e} is the mass of an electron, M_μ is the mass of the μ-th nucleus and Z_μ its atomic number. The Laplacian operators ∇_i^2 and ∇_μ^2 involve differentiation with respect to the coordinates of the i-th electron and the μ-th nucleus. The first term in equation 2.2 is the operator for the kinetic energy of the electrons; the second term represents the coulomb attraction between electrons and nuclei; the third term represents the coulomb repulsion between electrons; the fourth and fifth terms are the operators for the kinetic energy of the nuclei and the coulomb repulsion between nuclei, respectively.

The wavefunction $|\Psi\rangle$ is a function of the electronic and of the atomic positions. Because of the large ratio of the nuclear mass to the electronic mass, it is a reasonable approximation to separate the electronic and nuclear degrees of freedom with the ansatz:

$$|\Psi(\vec{r}_1,\ldots,\vec{r}_N,\vec{R}_1,\ldots,\vec{R}_M)\rangle \quad = \quad |\phi(\vec{r}_1,\ldots,\vec{r}_N)\rangle\,|\Phi(\vec{R}_1,\ldots,\vec{R}_M)\rangle.$$

There are three contributions to the kinetic energy: the motion of the nuclei, the motion of the electrons relative to the nuclei and the motion of the electrons together with the nuclei. The latter contribution enters the total kinetic energy with a pre-factor of $m_{\mathrm{e}}/M_\mu < 10^{-3}$. The separated treatment of the electronic and the nuclear system, known as *Born-Oppenheimer approximation*, corresponds to the neglection of this contribution. There exist some individual cases to which the Born-Oppenheimer approximation is not applicable.

In the Born-Oppenheimer approximation one first solves the electronic equation:

$$\hat{\mathrm{H}}_{\mathrm{el}}|\phi\rangle = E_{\mathrm{el}}|\phi\rangle, \tag{2.3}$$

which describes the motion of N electrons in the field of M *fixed* nuclei. The electronic wavefunction $|\phi\rangle$ explicitly depends on the electronic positions, but depends parametrically on the nuclear positions, as does the electronic energy E_{el}. The electronic Hamiltonian reads:

$$\hat{\text{H}}_{\text{el}} = -\sum_{i=1}^{N} \frac{1}{2}\nabla_i^2 - \sum_{i=1}^{N}\sum_{\mu=1}^{M} \frac{Z_\mu}{|\vec{r}_i - \vec{R}_\mu|} + \sum_{i=1}^{N}\sum_{j>i}^{N} \frac{1}{|\vec{r}_i - \vec{r}_j|}. \tag{2.4}$$

Subsequently it is possible to solve for the motion of the nuclei, which is described by:

$$\hat{\text{H}}_{\text{nuc}}|\Phi\rangle = E_{\text{tot}}|\Phi\rangle, \tag{2.5}$$

with

$$\hat{\text{H}}_{\text{nuc}} = -\sum_{\mu=1}^{M} \frac{1}{2M_\mu}\nabla_\mu^2 + \sum_{\mu=1}^{M}\sum_{\nu>\mu}^{M} \frac{Z_\mu Z_\nu}{|\vec{R}_\mu - \vec{R}_\nu|} + E_{\text{el}}(\{\vec{R}_\mu\}). \tag{2.6}$$

The Schrödinger equation for the electronic system is a $3N$-dimensional coupled differential-equation of second order. For any extended system consisting of numerous atoms this equation can be solved approximately, only. The level of approximation in the numerical treatment depends on the desired accuracy, the system size, and the available computer power to solve the problem numerically in a reasonable amount of time.

A widely used approximation is to apply a product-ansatz for the electronic wavefunction to obtain equations for a single independent electron in the averaged field of all other electrons:

$$\phi(\vec{r}_1, \ldots, \vec{r}_N) = \varphi(\vec{r}_1) \cdots \varphi(\vec{r}_N). \tag{2.7}$$

If the electronic Hamiltonian (2.4) can be written as a sum of terms depending solely on the position vector of one single electron, the electronic Schrödinger equation would decouple into N 3-dimensional differential equations. This being not the case, nevertheless one can try to find the best possible solution represented by a product ansatz of the form (2.7). The variational principle to find the minimum energy within this product ansatz leads to the *Hartree equations*:

$$\left[-\frac{\nabla^2}{2} + V_0(\vec{r}) + V_H(\vec{r})\right] \varphi_k(\vec{r}) = \varepsilon_k \varphi_k(\vec{r}), \tag{2.8}$$

with the external potential V_0 resulting from the M nuclear charges

$$V_0(\vec{r}) = \sum_{\mu=1}^{M} \frac{Z_\mu}{|\vec{r} - \vec{R}_\mu|}$$

and the *Hartree potential*

$$V_{\text{H}}(\vec{r}_i) = \sum_{i \neq j}^{N} \int d^3r_j\, \varphi_j^*(\vec{r}_j)\varphi_j(\vec{r}_j)\frac{1}{|\vec{r}_j - \vec{r}_i|}.$$

Since the Hartree potential itself depends on the wavefunctions φ_k, the Hartree equations 2.8 have to be solved iteratively until the input wavefunctions are equal (consistent) to the output wavefunctions. This is called a *self-consistent-field* (scf) algorithm.

Physically one cannot distinguish between different electrons. This leads to the additional requirement that the total wavefunction $\Phi(\vec{r}_1, \ldots, \vec{r}_N)$ be antisymmetric with respect to interchange of any two electrons, so that

$$\Phi(\ldots, \vec{r}_i, \ldots, \vec{r}_j, \ldots) = -\Phi(\ldots, \vec{r}_j, \ldots, \vec{r}_i, \ldots).$$

This requirement can be fulfilled by replacing the simple product ansatz (2.7) by a, so called, *Slater determinant*:

$$\tilde{\phi}(\vec{r}_1, \ldots, \vec{r}_N) = \frac{1}{\sqrt{N!}} \begin{vmatrix} \varphi_1(\vec{r}_1) & \cdots & \varphi_N(\vec{r}_1) \\ \vdots & & \vdots \\ \varphi_1(\vec{r}_N) & \cdots & \varphi_N(\vec{r}_N) \end{vmatrix}.$$

Application of the variational principle to find the minimum energy for a single Slater determinant leads to the *Hartree-Fock equations*:

$$\left[-\frac{\nabla^2}{2} + V_0(\vec{r}) + V_H(\vec{r}) \right] \phi_k(\vec{r}) - \sum_{l=1}^{N} \phi_l(\vec{r}) \int d^3r' \, \frac{\phi_l^*(\vec{r}')\phi_k(\vec{r}')}{|\vec{r} - \vec{r}'|} = \varepsilon_k \phi_k(\vec{r}), \tag{2.9}$$

containing an additional nonlocal term and adding the *exchange energy*

$$E_{\mathrm{X}} = \frac{1}{2} \sum_{i \neq j}^{N} \int d^3r_i \int d^3r_j \, \varphi_i^*(\vec{r}_i) \varphi_j^*(\vec{r}_j) \frac{1}{|\vec{r}_j - \vec{r}_i|} \varphi_i(\vec{r}_j) \varphi_j(\vec{r}_i) \tag{2.10}$$

to the total electronic energy.

The solution of the Hartree-Fock equations (2.9) yields a set $\{\varphi_k\}$ of orthonormal Hartree-Fock orbitals with orbital energies $\{\varepsilon_k\}$. The Slater determinant formed from the N orbitals with the lowest energies is the Hartree-Fock ground-state ϕ_0. In practice one expands the Hartree-Fock orbitals into a finite basis set which replaces the differential equations by algebraic equations. The larger and more complete the set of basis functions the lower will be the expectation value $E_0 = \langle \phi_0 | \hat{\mathrm{H}}_{\mathrm{HF}} | \phi_0 \rangle$. The limit for larger and larger basis sets is called the *Hartree-Fock limit.* The Hartree-Fock limit is *not* the correct energy of the many electron system, because the many electron wavefunction cannot be represented by a single Slater determinant. To obtain the correct energy one has to expand the many electron wavefunction into an infinite basis set. An arbitrary antisymmetric function of N variables can be expanded in terms of all unique determinants formed from a complete set of one-variable functions, e.g., the set of Hartree-Fock orbitals $\{\varphi_k\}$. The difference between the correct energy $\mathcal{E}_0$ and the Hartree-Fock limit E_0 is called the *correlation energy*

$$E_{\mathrm{corr}} = \mathcal{E}_0 - E_0,$$

since the motion of electrons with opposite spins is not correlated within the Hartree-Fock approximation.

One extension to the Hartree-Fock approximation taking correlation into account is called Hartree-Fock with *configuration interaction* (HF-CI) (see, e.g., [3]).

The physical significance of the orbital energies ε_k, i.e., the eigenvalues of the Hartree-Fock equations, is that they provide an approximation to the ionization potential and the electron affinity, as stated in *Koopmans' Theorem: "The energy ε_a belonging to an occupied orbital corresponds to the negative of the energy needed to produce an $(N-1)$-electron single Slater determinant with identical orbitals, obtained by removing an electron from orbital φ_a. The energy ε_r belonging to a non-occupied orbital corresponds to the energy gained to produce an $(N+1)$-electron single Slater determinant with identical orbitals obtained by adding an electron to orbital φ_r."* This "frozen orbital" approximation neglects relaxation of the orbitals caused by increasing or decreasing the number of electrons by one. The usage of a single determinant within HF theory, i.e., the neglection of correlation effects, leads to additional errors in the ionization potentials and electron affinities. In general, Koopmans ionization potentials are reasonable first approximations to experimental ionization potentials, whereas Koopmans electron affinities are often inaccurate.

The orbital energy ε_a includes coulomb and exchange interactions between an electron in φ_a and electrons in all other occupied orbitals (in particular φ_b). Since ε_b includes interactions between the electron in φ_b and φ_a, as well, the sum over all energy levels $\sum_i \varepsilon_i$ belonging to occupied orbitals contains the interaction between all electron pairs twice. Thus, the total energy of the electronic system equals the sum over all ε_i corresponding to occupied orbitals φ_i minus the double counted contribution.

$$\begin{aligned} E_0 &= \sum_i^N m_i\varepsilon_i - \frac{1}{2}\sum_{i=1}^N\sum_{j\neq i}^N \int d^3r_j \int d^3r_i \, \frac{\varphi_j^*(\vec{r}_j)\varphi_j(\vec{r}_j)\varphi_i^*(\vec{r}_i)\varphi_i(\vec{r}_i)}{|\vec{r}_j-\vec{r}_i|} \qquad (2.11) \\ &+\frac{1}{2}\sum_{i=1}^N\sum_{j\neq i}^N \int d^3r_j \int d^3r_i \, \frac{\varphi_i^*(\vec{r}_i)\varphi_j^*(\vec{r}_j)\varphi_i(\vec{r}_j)\varphi_j(\vec{r}_i)}{|\vec{r}_j-\vec{r}_i|} \\ &= \sum_i^N m_i\varepsilon_i - \frac{1}{2}E_\mathrm{H} + \frac{1}{2}E_\mathrm{xc}, \end{aligned}$$

where m_i denotes the occupation number for orbital φ_i.

2.2 Density-functional Theory

The calculation of the exchange energy (2.10) is quite time-consuming, because it involves the evaluation of four-center integrals. Therefore, after the development of Hartree-Fock theory different attempts to approximate it by the simple form

$$E_\mathrm{X} = \int d^3r \, \varepsilon_\mathrm{X}(n(\vec{r}))$$

occured, where $\varepsilon_\mathrm{X}(n)$ is the exchange energy density for a uniform electron gas of density n. This is given (see, for example, [5]) by

$$\varepsilon_\mathrm{X}(n) = -\frac{3}{4}e^2\left(\frac{3}{\pi}\right)^{1/3} n^{4/3}.$$

Then the variational principle leads to just the Hartree equations 2.8 with an additional exchange potential

$$V_{\mathrm{X}}(\vec{r}) = -e^2 \left(\frac{3}{\pi}\right)^{1/3} n^{1/3}(\vec{r}).$$

A similar approach was given by the X_α-method of Slater [6]. The same theory had been developed as an extension of Thomas-Fermi theory.

Instead of expressing only the exchange energy in terms of the electron density one can try to express the total energy in terms of it. The mathematical foundation to this attempt is given by the theorem of Hohenberg and Kohn [7]:

The energy E_g of an electronic system in its nondegenerate ground-state is a unique functional of the ground-state electronic density n: $E_g = E[n]$. For a nondegenerate ground-state the energy functional under variation of n is minimal at the ground-state electronic density.

While the Hohenberg-Kohn theorem is not directly useful, because it does not indicate how to obtain n nor how to calculate the total energy from a given n, Kohn and Sham [8] suggested a feasible algorithm to obtain an approximate solution:

The energy functional can be written as:

$$E[n] = T_0[n] + E_{\mathrm{ext}}[n] + E_{\mathrm{H}}[n] + E_{\mathrm{xc}}[n], \tag{2.12}$$

where E_{ext} is the contribution due to the external potential, e.g., the coulomb potential due to the nuclei:

$$E_{\mathrm{ext}}[n] = \int d^3r\, n(\vec{r}) V_{\mathrm{ext}}(\vec{r})$$

and E_{H} is the electronic coulomb or Hartree contribution:

$$E_{\mathrm{H}}[n] = \frac{1}{2}\int d^3r\, n(\vec{r}) V_{\mathrm{H}}(\vec{r}) = \frac{1}{2}\int d^3r\, n(\vec{r}) \int d^3r' \frac{n(\vec{r}')}{|\vec{r}-\vec{r}'|}.$$

The term T_0 corresponds to the kinetic energy of a *non-interacting* inhomogeneous electron gas with density n. The last term E_{xc} in (2.12) is defined by the three other terms, i.e., it contains all other contributions to the total ground-state energy, namely the exchange and correlation energies and the corrections to the kinetic energy caused by the electronic interaction. The exact functional dependence on n is not known and has to be approximated.

Kohn and Sham suggested to represent the density n in terms of normalized single electron orbitals φ_i with occupation numbers m_i:

$$n(\vec{r}) = \sum_i^M m_i |\varphi_i(\vec{r})|^2, \quad \text{with} \sum_i^M m_i = N.$$

The total energy expressed in terms of the single electron orbitals reads:

$$E = \sum_i^M m_i \int d^3r\, \varphi_i^*(\vec{r}) \left(-\frac{\nabla^2}{2} + V_{\mathrm{ext}}(\vec{r}) + \frac{1}{2} V_{\mathrm{H}}[n(\vec{r})]\right) \varphi_i(\vec{r}) + E_{\mathrm{xc}}[n]. \tag{2.13}$$

Because of the Hohenberg-Kohn theorem the variation of the energy with respect to the density must vanish at the ground-state density:

$$\frac{\delta}{\delta\varphi_i^*(\vec{r})}\left[E[\{\varphi_j^*\}]-\sum_{j,k}^{M}\lambda_{j,k}\int d^3r'\,\varphi_j^*(\vec{r}')\varphi_k(\vec{r}')\right]=0,$$

where the Lagrange multipliers $\lambda_{j,k}$ take into account the normalization of the φ_j. This leads to the *Kohn-Sham equations*:

$$\left[-\frac{\nabla^2}{2}+V_{\text{ext}}(\vec{r})+V_{\text{H}}[n(\vec{r})]+V_{\text{xc}}[n(\vec{r})]\right]\varphi_i(\vec{r})=\varepsilon_i\varphi_i(\vec{r}). \tag{2.14}$$

The exchange-correlation potential V_{xc} is defined as the functional derivative of the exchange-correlation energy:

$$V_{\text{xc}}[n]=\frac{\delta E_{\text{xc}}[n]}{\delta n}.$$

The operator acting on the orbitals φ_i in the above Kohn-Sham equations depends on the density n and thus on the orbitals themselves. Hence, the Kohn-Sham equations have to be solved iteratively. One starts with a reasonable density to obtain the orbitals which determine a new density. This new density is substituted into the operator until the differences between successive densities can be neglected. Like in Hartree-Fock theory this algorithm is called self-consistent-field (scf) algorithm.

The total energy in density-functional theory can be written as a sum over the eigenvalues belonging to occupied orbitals plus a correction for the double counted electron-electron interaction (similar to Hartree-Fock theory).

$$E[n]=\sum_{i}^{M}m_i\varepsilon_i-E_{\text{H}}[n]-\int d^3r\,n(\vec{r})V_{\text{xc}}[n(\vec{r})]+E_{\text{xc}}[n]. \tag{2.15}$$

An alternative expression can be obtained by substitution of the sum over the eigenvalues after multiplying the Kohn-Sham equations from the left with φ_i^* and summing over all occupied states. This yields:

$$E[n]=-\frac{1}{2}\sum_{i}^{M}\int d^3r\,\varphi_i^*(\vec{r})\nabla^2\varphi_i(\vec{r})+\int d^3r\,n(\vec{r})V_{\text{ext}}(\vec{r})+E_{\text{H}}[n]+E_{\text{xc}}[n]. \tag{2.16}$$

For spin-polarized systems the total electron density has to be divided into a spin-up and a spin-down density. For each of both densities separate Kohn-Sham equations must be solved. The Kohn-Sham operator in both equations is dependent on both, the spin-up and the spin-down density.

The eigenvalues in the Kohn-sham equation correspond to the first-order change of the total energy with respect to changes of the occupation numbers m_i:

$$\frac{\partial E[n]}{\partial m_i}=\int d^3r\,\varphi_i^*(\vec{r})\left(-\frac{\nabla^2}{2}+V_{\text{ext}}(\vec{r})+V_{\text{H}}[n(\vec{r})]+V_{\text{xc}}[n(\vec{r})]\right)\varphi_i(\vec{r})=\varepsilon_i.$$

This equation is known as *Janaks Theorem.* In the exact density-functional formalism the highest eigenvalue gives the ionization energy for a molecule or the work function for a metal (see [4]). For most approximate functionals, however, this is not valid and even in the exact DF formalism it is valid only for the eigenvalue of the highest occupied state. The cooresponding theorem to Koopmans Theorem is, in general, not applicable in DFT.

2.2.1 Approximations for the Exchange-Correlation Energy

The exact functional form of the exchange-correlation energy E_{XC} in (2.12) is not known and has to be approximated. The simplest approximation is the *Local-Density-Approximation (LDA).* Here, one replaces the exchange-correlation energy of a small volume element dV at location $\vec{r}$ by the corresponding exchange-correlation energy of the homogenous electron gas of density $n(\vec{r})$. The exchange contribution to the exchange-correlation energy per electron for the homogenous electron gas with given density n can be calculated exactly within Hartree-Fock theory:

$$\varepsilon_{\mathrm{X}}(n) = -\frac{3}{4}\left(\frac{3}{\pi}\right)^{1/3} n^{1/3}.$$

The correlation energy as a function of the electron density can be obtained as the difference between the total energy calculated with an accurate numerical method including correlation effects and the Hartree-Fock energy. This was done by Ceperley and Alder [9]. The exchange-correlation energy per electron $\varepsilon_{\mathrm{XC}}$ is just the sum of the exchange and the correlation energy per electron:

$$\varepsilon_{\mathrm{XC}}(n) = \varepsilon_{\mathrm{X}}(n) + \varepsilon_{\mathrm{C}}(n).$$

It follows that the exchange-correlation energy of an electronic system with inhomogeneous density n within the Local-Density-Approximation is given by:

$$E_{\mathrm{XC}}^{\mathrm{LDA}}[n] = \int d^3r\, n(\vec{r})\varepsilon_{\mathrm{XC}}(n(\vec{r})), \tag{2.17}$$

and the corresponding exchange-correlation potential reads:

$$V_{\mathrm{XC}}^{\mathrm{LDA}}[n](\vec{r}) = \frac{\delta E_{\mathrm{XC}}^{\mathrm{LDA}}[n]}{\delta n(\vec{r})} = \varepsilon_{\mathrm{XC}}(n(\vec{r})) + \left.\frac{d\varepsilon_{\mathrm{XC}}(n)}{dn}\right|_{n=n(\vec{r})} n(\vec{r}). \tag{2.18}$$

The Local-Density-Approximation gives quite satisfactory results for the density, energy and other derived physical properties of many molecular and crystalline systems. This is despite the fact that these systems exhibit a strongly varying density, very different from the density of a homogenous electron gas. One deficiency of the LDA is the tendency to overestimate the total energy of a stable system in comparison to its separated atomic parts. Partly, this is due to too high an energy in the single atom calculations. For some metastable transition states with a large number of bonds, this overestimation is especially large. Therefore, cohesive energies for stable configurations are often too negative, whereas reaction barriers are often too small. This systematic error is known as *LDA over-binding.*

One way to improve this and some other shortcomings of the Local-Density-Approximation is to take into account the dependency of the exchange-correlation energy on the density-gradient in addition to just on the density:

$$E_{\mathrm{xc}}^{\mathrm{GGA}}[n, \nabla n] = \int d^3r\, n(\vec{r})\varepsilon_{\mathrm{xc}}(n(\vec{r}), \nabla n(\vec{r})).$$

This *Generalized-Gradient-Approximation (GGA)* makes the method more flexible, but also introduces more parameters to be determined. In general the GGA improves cohesive energies, transition state barriers, and, in some cases, infrared absorption intensities.

There exist several parametrizations of the exchange-correlation potential within the LDA and the GGA. In general deviations in the results obtained with two different parametrizations are small. Two common parametrizations implemented in the computer codes used for this thesis are from Perdew-Wang '91 (PW-91) [10] and from Perdew-Burke-Ernzerhof (PBE) [11].

2.2.2 Basis Set Expansion of the Kohn-Sham orbitals

In order to solve the Kohn-Sham equation in practice one needs a suitable representation for the Kohn-Sham orbitals. They can be represented directly on a fine real-space grid and the Kohn-Sham equation can be solved by direct numerical integration. More common is the expansion of the Kohn-Sham orbitals into a finite basis-set which transforms the integro-differential equation into an algebraic equation. The basis-set expansion of the Kohn-Sham orbitals φ_i:

$$\varphi_i(\vec{r}) = \sum_{\mu=1}^{N_b} c_{\mu i}\chi_\mu(\vec{r}) \tag{2.19}$$

is determined by the fixed basis functions χ_μ. The expansion coefficients $c_{\mu i}$ have to be determined. The electronic energy can be expressed in terms of the basis functions χ_μ as follows:

$$E(\{\chi_\mu\}) = \sum_{\mu=1}^{N_b}\sum_{\nu=1}^{N_b} P_{\mu\nu} \int d^3r\, \chi_\mu^*(\vec{r}) \left[-\frac{\nabla^2}{2} + V_{\mathrm{ext}}(\vec{r}) + \frac{1}{2}V_{\mathrm{H}}[n(\vec{r})]\right] \chi_\nu(\vec{r}) + E_{\mathrm{xc}}[n(\vec{r})], \tag{2.20}$$

with

$$n(\vec{r}) = \sum_{\mu=1}^{N_b}\sum_{\nu=1}^{N_b} P_{\mu\nu}\chi_\mu^*(\vec{r})\chi_\nu(\vec{r}), \quad P_{\mu\nu} = \sum_{i=1}^{M} m_i c_{\mu i}^* c_{\nu i}. \tag{2.21}$$

The $P_{mu\nu}$ are the elements of the *density matrix* P and N_b is the number of basis functions.

The requirement on the expansion coefficients $c_{\mu i}$ to minimize the energy leads via the variational principle:

$$\frac{\partial}{\partial c_{\mu i}^*}\left[E[\{\chi_\mu\}] - \sum_{j=1}^{M} m_j\varepsilon_j \left(\sum_{\mu=1}^{N_b}\sum_{\nu=1}^{N_b} c_{\mu j}^* c_{\nu j} \int d^3r \chi_\mu^*(\vec{r})\chi_\nu(\vec{r}) - 1\right)\right] = 0 \tag{2.22}$$

to an algebraic generalized eigenvalue problem:

$$\sum_{\nu=1}^{N_b} (H_{\mu\nu} - \varepsilon_i S_{\mu\nu})\, c_{\nu i} = 0, \quad \mu, i = 1, \ldots, N_b. \tag{2.23}$$

The Hamiltonian matrix elements are defined by

$$H_{\mu\nu} = \int d^3r\, \chi_\mu^*(\vec{r}) \left[-\frac{\nabla^2}{2} + V_{\text{ext}}(\vec{r}) + +V_{\text{H}}[n(\vec{r})] + V_{\text{XC}}[n(\vec{r})] \right] \chi_\nu(\vec{r}) \tag{2.24}$$

and the overlap matrix elements are defined by

$$S_{\mu\nu} = \int d^3r\, \chi_\mu^*(\vec{r}) \chi_\nu(\vec{r}). \tag{2.25}$$

Solving the generalized eigenvalue problem (2.23) yields the coefficients $c_{\nu i}$, which together with the basis functions χ_ν determine the ground-state density n according to equation (2.21). To optimize the geometry or to perform molecular dynamics one needs to calculate the nuclear forces, i.e., the derivatives of the total energy with respect to the nuclear coordinates $\vec{R}_k$. The nuclear forces depend on the external potential V_{ext}, the basis set (if atom centered localized basis functions are used), and the total electronic energy, which depends parametrically on the nuclear coordinates:

$$\begin{aligned} \vec{F}_k = {} & \frac{\partial}{\partial \vec{R}_k} \int d^3r\, \frac{Z_k n(\vec{r})}{|\vec{r} - \vec{R}_k|} - 2\mathcal{R}e \left\{ \sum_{i=1}^{M} m_i \sum_{\mu=1}^{N_b} \sum_{\nu=1}^{N_b} c_{\mu i}^* c_{\nu i} \int d^3r\, \frac{\partial \chi_\mu(\vec{r})}{\partial \vec{R}_k} \right. \\ & \left. \left(-\frac{\nabla^2}{2} - \sum_{l+1}^{N_{\text{at}}} \frac{Z_l}{|\vec{R} - \vec{R}_l|} + V_{\text{H}}[n(\vec{r})] + V_{\text{XC}}[n(\vec{r})] - \varepsilon_i \right) \chi_\nu(\vec{r}) \right\}. \end{aligned} \tag{2.26}$$

The first term in the equation above is due to the explicit dependence of the external potential on the nuclear coordinates and is called *Hellmann-Feynman force.* The second term is the *Pulay correction* resulting from the explicit dependence on the (atom centered) basis functions [12].

2.3 Density-functional based Tight-Binding method

The self-consistent solution of the full-potential Kohn-Sham equation with a converged basis set requires a vast number of mathematical operations. Today a generic workstation with about one billion floating point operations per second (1 GFLOP) needs 10 to 100 hours to find the equilibrium geometry of a system with about 10 atoms (100 electrons). To treat larger systems with hundreds of atoms or to perform molecular dynamics even on small systems one has to use approximate methods, which try to decrease the computational expense without loosing too much accuracy. The required accuracy depends on the problem to solve. E.g., to determine the lowest energy structure from several given isomers the error in cohesive energy must be smaller than the energy differences, but not necessarily much smaller. Furthermore, often relative energies are more important than absolute ones, again the determination of low energy structures provides a good example.

There are several possibilities to approximate the full solution of the Kohn-Sham equation (or of Hartree-Fock based equations):

- Small basis set: For many physical properties like geometries and relative energies numerical complete basis sets and fully converged energies are not necessary.
- Replacement of core electrons by pseudo-potentials or frozen cores: Chemical bonding and many physical properties are mainly determined by the valence electrons.
- Neglection of multi-center integrals: Depending on the representation of the potential and the density the contribution to the total energy of some of these integrals can be neglected.
- Approximation to the full potential: An expansion of the potential into atom centered radial functions and spherical harmonics up to low angular momentums takes into account the most important contributions.
- Anticipation of self-consistent iteration: A superposition of atomic densities leads to changes in the density during the scf iteration which are similar for many different systems. These general changes (e.g. contraction of the atomic densities) can be anticipated in the start density to accelerate or omit the scf-iteration.

The approximate density-functional based tight-binding (DFTB) method used in this work is based on the work of Seifert, Eschrig and Bieger [13]. In contrast to empirical tight-binding methods the Hamilton and overlap matrix elements between atoms at two different center are calculated within scf-DFT from approximate two-center potentials and modified atomic wave-functions.

The tight-binding method can be viewed as an approximation to the energy expression in density-functional theory. If the ground-state electron-density n is known, the Kohn-Sham orbitals φ_i and eigenvalues ε_i along with the corresponding total energy can be determined in one step from the Kohn-Sham equation (2.14) and the DFT energy expression (2.12). Since the ground-state energy is variational with respect to variation of n, the error in the total energy $E[n_0]$ introduced by making a clever guess n_0 to the correct density n (the one resulting from a sophisticated full scf iteration), is of second order in $\delta n := n - n_0$. The error in the energy is small, if $\delta n(\vec{r})$ is small for all $\vec{r}$ [14, 15]:

$$\begin{aligned}
E[n] &= E[n_0] + \frac{1}{2}\int\int' \frac{\delta^2 E}{\delta n(\vec{r})\delta n(\vec{r}')}\Big|_{n_0} \delta n(\vec{r})\delta n(\vec{r}') + \mathcal{O}(3) \qquad (2.27)\\
&= \sum_i^{occ} m_i \left\langle \varphi_i \left| -\frac{\Delta}{2} + V_{ext}(\vec{r}) + \int d^3r' \, \frac{n_0(\vec{r}')}{|\vec{r}-\vec{r}'|} + V_{\mathrm{XC}}[n_0] \right| \varphi_i \right\rangle \\
&\quad -\frac{1}{2}\int d^3r \int d^3r' \, \frac{n_0(\vec{r}')n_0(\vec{r})}{|\vec{r}-\vec{r}'|} + E_{\mathrm{XC}}[n_0] - \int d^3r \, n_0(\vec{r}) V_{\mathrm{XC}}[n_0(\vec{r})]
\end{aligned}$$

$$+\frac{1}{2}\int d^3r \int d^3r' \left(\frac{1}{|\vec{r}-\vec{r}'|} + \frac{\delta^2 V_{\mathrm{xc}}[n]}{\delta n(\vec{r})\delta n(\vec{r}')}\Big|_{n_0}\right) \delta n(\vec{r})\delta n(\vec{r}') + \mathcal{O}(3).$$

By expanding the many-atom potential based on the self-consistent ground-state electronic density into atom-centered local potentials, one notices that the many-atom potential can be approximated better if the atomic potentials are based on contracted atomic densities rather than free atomic densities [16]. The contracted atomic densities can be obtained by solving the Kohn-Sham equation for a free single atom with the additional potential

$$V_{\mathrm{ad}}(\vec{r}) = \left(\frac{|\vec{r}|}{|\vec{r}_0|}\right)^n, \quad n = 2. \tag{2.28}$$

This potential forces the electrons to avoid regions far from the center and consequently increases the density in the region where $|\vec{r}|$ is small. The self-consistent solution of the single atom Kohn-Sham equation with the additional potential yields contracted atomic densities n_{psat}, so called *pseudo-atomic densities*. The superposition of these pseudo-atomic densities yields in general a good approximation to the electronic density for systems consisting of several atoms. Since the contraction parameter r_0 is fixed, not all conceivable atomic arrangements are properly described. The contraction parameter is chosen such that systems with a generic bonding pattern (generic number of bonds and generic bond-lengths) are accurately described. The method might fail to accurately describe extraordinary systems like dissociated or highly coordinated systems.

Within standard DFTB the electronic density n of the many atom system is approximated by the superposition n_0 of the pseudo-atomic densities and the energy expression (2.27) is expanded to first order with respect to δn. The DFTB method has also been extended to calculate the charge transfer between atoms with different net-charges in a self-consistent way [15]. This corresponds to an approximation of the second order term in (2.27) and is referred to as self-consistent-charge (SCC)-DFTB.

Within standard DFTB the term for total energy (2.27) of an system consisting of many atoms is represented as

$$E_{\mathrm{DFTB}} = \sum_i^{\mathrm{occ}} \varepsilon_i + \sum_{k,l\neq k}^{M} V_{\mathrm{rep}}(|\vec{R}_k - \vec{R}_l|). \tag{2.29}$$

The eigenvalues ε_i are obtained from the solution of the generalized eigenvalue equation (2.23). The second term approximates the double counting and coulomb terms defined in (2.15) by a summation over short-ranged pairwise potentials.

The energy expression within SCC-DFTB additionally contains the approximation to the second order term in (2.27):

$$E_{\mathrm{DFTB}}^{\mathrm{SCC}} = \sum_i^{\mathrm{occ}} \varepsilon_i + \frac{1}{2}\sum_{k,l\neq k}^{M} \gamma_{kl}\Delta q_k \Delta q_l + \sum_{k,l\neq k}^{M} V_{\mathrm{rep}}(|\vec{R}_k - \vec{R}_l|). \tag{2.30}$$

The functional γ_{kl} denotes the approximation to the integral in the second order term in (2.27) and Δ_k denotes the charge fluctuation on site k (see Ref. [15]).

Equivalent to full DFT, the Kohn-Sham orbitals φ_i are represented as a *Linear Combination of Atomic Orbitals* (LCAO) centered at the atomic positions $\vec{R}_k$ to transform the Kohn-Sham equation into an algebraic eigenvalue equation (cf. Eq. 2.23):

$$\varphi_i(\vec{r}) = \sum_{\mu=1}^{N_b} c_{\mu i}\chi_\mu(\vec{r}-\vec{R}_k)$$

The eigenfunctions of a free atom have quite long tails and, therefore, do not provide optimal basis functions for solid systems. More suitable basis functions can be obtained by solving the single atom Kohn-Sham equation with the additional contracting potential (2.28)

$$\left[\hat{T} + V^{\text{at}}(r) + \left(\frac{r}{r_0}\right)^n\right]\chi_\mu(\vec{r}) = \tilde{\varepsilon}_\mu\chi_\mu(\vec{r}).$$

To allow for an efficient implementation only one- and two-center integrals are considered in the setup of the Hamiltonian matrix. This approximation is supported by the usage of contracted atomic densities, because the contraction causes the small three-center contributions to become further reduced.

The following contributions to the Hamilton matrix (2.24) are neglected:

$$\langle\chi_\mu^A|V^B|\chi_\nu^A\rangle = 0, \quad \mu \neq \nu \vee \mu = \nu \tag{2.31}$$

$$\langle\chi_\mu^A|V^C|\chi_\nu^B\rangle = 0, \quad C \neq A \wedge C \neq B. \tag{2.32}$$

Here χ_μ^A denotes the basis function of type μ = 1s, 2s, 2p$_x$, ... centered at atom A and V^A denotes the atomic potential of atom A. In general, only the valence orbitals are taken into account and the *frozen core* approximation is applied, i.e., core orthogonalization effects are not explicitly considered. The first of the equations above corresponds to the neglection of the so called *crystal field integrals*, the second equation corresponds to the neglection of three-center integrals. Furthermore, the diagonal elements are replaced by the eigenvalues of the free atom (instead of using the eigenvalues of the pseudo-atom):

$$\langle\chi_\mu^A|\hat{T} + V^A|\chi_\mu^A\rangle = \varepsilon_\mu^A, \quad \text{(free atom)}. \tag{2.33}$$

Because of the two-center approach, the Hamilton and overlap integrals need to be calculated only once for each pair of atom types and a given set of two-center distances $R = |\vec{R}^A - \vec{R}^B|$.

The potential V^{AB} of a system of two atoms A and B with pseudo-atomic densities n_{psat}^A and n_{psat}^B at center $\vec{R}^A$ and $\vec{R}^B$ is given by

$$\begin{aligned} V^{AB}(\vec{r}) = & -\frac{Z^A}{|\vec{r}-\vec{R}^A|} + V_{\text{H}}[n_{\text{psat}}^A(\vec{r}-\vec{R}^A)] \\ & -\frac{Z^B}{|\vec{r}-\vec{R}^B|} + V_{\text{H}}[n_{\text{psat}}^B(\vec{r}-\vec{R}^B)] \\ & +V_{\text{xc}}\left[n_{\text{psat}}^A(\vec{r}-\vec{R}^A) + n_{\text{psat}}^B(\vec{r}-\vec{R}^B)\right]. \end{aligned} \tag{2.34}$$

For the calculation of the exchange-correlation potential V_{xc} the density of the two center is superposed first and then the nonlinear V_{xc} is calculated for the combined density. This approach is different from earlier works with DFTB, where the many atom potential was represented as a linear superposition of spherical single atom potentials [17].

The solution of the generalized eigenvalue equation (2.23) with the approximated Hamiltonian yields the eigenvalues ε_i and wavefunction coefficients $c_{\mu i}$. From the eigenvalues one obtains the DFTB band-structure energy $E_{\text{BS}} = \sum_i^{\text{occ}} \varepsilon_i$. To obtain the total energy one needs to determine the repulsive potential V_{rep} for any combination of atom types as a function of internuclear distance. The repulsive energy is obtained from the difference between the total energy $E_{\text{tot}}^{\text{scf}}$ calculated within scf-DFT and the DFTB band-structure energy E_{BS}:

$$E_{\text{rep}} = E_{\text{tot}}^{\text{scf}} - E_{\text{BS}} \tag{2.35}$$

for an appropriate reference structure. This structure must have only one unique bond type. E.g., the diamond structure, the dimer or $\text{Si}_5(\text{T}_d)$ are suitable structures for silicon. V_{rep} in equation (2.29) equals E_{rep} per bond, because it is added for each nonequivalent atom-pair.

The DFTB method has already been applied to a variety of systems [18] containing several atomic types, such as silicon (Chapters 4 and 7) [19, 20, 21], carbon [22, 23], silicon-carbide [24, 25, 26, 27], gallium-arsenide [28], and gallium-nitride [29].

The explicit calculation of the Hamilton- and overlap-matrix elements and of the repulsive potential for silicon is described in more detail in Appendix A.

Chapter 3

Vibrational spectroscopy

It is very difficult to determine the geometry of a cluster or molecule directly by experiment. Therefore, it is not possible to compare a theoretically determined structure to experiment, if only the bond lengths and angles have been calculated. Instead the calculation of additional measurable properties is necessary. Infrared (IR) and Raman spectroscopy belong to the most commonly applied methods for the classification of clusters and molecules. The vibrational frequencies provide an unique fingerprint for different structures. Since the selection rules for IR absorption and Raman scattering are different, both methods complement each other. Infrared spectroscopy is based on the absorption of a photon to excite a vibrational mode, whereas in non-resonant Raman spectroscopy a photon the frequency of which is higher than that of the vibrational modes is inelastically scattered. Other useful methods to link theory to experiment are ultraviolet photo-electron spectroscopy (UPS), UV spectroscopy which detects excited electronic states, or Nuclear Magnetic Resonance (NMR) spectroscopy, which measures the interaction of the nuclear spin with the electronic charge. A somewhat different method is the determination of cluster mobilities, which is described in Chapter 6.

3.1 Vibrational frequencies and normal modes

The equilibrium geometry of a cluster at zero temperature corresponds to the global minimum of the energy surface spanning the $3M$-dimensional space of the nuclear coordinates. The atoms perform a zero point vibration around the equilibrium position. This is equivalent to the quantum mechanical harmonic oscillator, where the lowest state corresponds to an oscillation and not to a fixed position, in agreement with Heisenbergs uncertainty law. Adding energy to the system by increasing the temperature or supplying light of appropriate wavelength can induce transitions to higher vibrational states. The vibrational frequencies depend on the curvature of the potential surface at the equilibrium position, i.e., on how much the potential changes during small displacements of the atoms.

A system consisting of M atoms has $3M$ degrees of freedom. Since 3 degrees describe translation and another 3 degrees describe rotation of the whole system, there are

$3M-6$ internal degrees of freedom corresponding to vibrations of the atoms around their equilibrium positions. Linear molecules have only two rotational degrees of freedom and, therefore, have $3M-5$ internal degrees of freedom.

In classical terms, the energy of an atomic system with respect to the nuclear coordinates $\vec{R}_k$ reads:

$$E_M(\vec{R}_1,\ldots,\vec{R}_M) = \sum_{k=1}^{M} \frac{m_k}{2} \dot{\vec{R}_k}^2 + V(\vec{R}_1,\ldots,\vec{R}_M), \tag{3.1}$$

where V represents the total energy of the electronic system in its ground state plus the coulomb potential of the nuclei. A dot denotes the derivative with respect to time.

Denoting the set of nuclear coordinates $(\vec{R}_1,\ldots,\vec{R}_M)$ as

$$\vec{R} = (R_1, R_2, R_3, \ldots, R_{3M-2}, R_{3M-1}, R_{3M})$$

to simplify notation, the potential in the vicinity of the equilibrium point $\vec{R}^0$ can be expanded in a Taylor series:

$$\begin{aligned} V(\vec{R}) &= V(\vec{R}^0) + \sum_{j=1}^{3M} \frac{\partial V}{\partial R_j}\Big|_{\vec{R}^0} (R_j - R_j^0) \\ &+ \frac{1}{2} \sum_{i=1}^{3M} \sum_{j=1}^{3M} \frac{\partial^2 V}{\partial R_i \partial R_j}\Big|_{\vec{R}^0} (R_i - R_i^0)(R_j - R_j^0) + \mathcal{O}(3) \\ &= V(\vec{R}^0) - \sum_{j=1}^{3M} F_j^0 (R_j - R_j^0) + \frac{1}{2} \sum_{i=1}^{3M} \sum_{j=1}^{3M} H_{ij}^0 (R_i - R_i^0)(R_j - R_j^0) + \mathcal{O}(3). \end{aligned}$$

Here, F_j^0 and H_{ij}^0 denote the components of the forces and the so called *Hessian matrix*, respectively. The matrix H^0 is real and symmetric and, therefore, has only real eigenvalues and can always be transformed into diagonal form. The forces $\vec{F}^0$ vanish at the equilibrium point $\vec{R}^0$ and the 3rd and higher order terms are small in the vicinity of $\vec{R}^0$. In the harmonic approximation, where one neglects these higher order terms, the energy expression (3.1) reads:

$$\begin{aligned} E_M(\vec{R}_1,\ldots,\vec{R}_M) &= \sum_{k=1}^{M} \frac{m_k}{2} \dot{\vec{R}_k}^2 + V(\vec{R}^0) \\ &+ \frac{1}{2} \sum_{i=1}^{3M} \sum_{j=1}^{3M} H_{ij}^0 (R_i - R_i^0)(R_j - R_j^0). \end{aligned} \tag{3.2}$$

The classical equation of motion for the moving nuclei is

$$\sum_{j=1}^{3M} \delta_{ij} \frac{d^2 R_j}{dt^2} + \sum_{j=1}^{3M} H_{ij}^0 R_j = 0, \quad i = 1, 2, \ldots, 3M. \tag{3.3}$$

Within the Cartesian coordinates R_j the $3M$ degrees of freedom are coupled. To decouple the system, one has to find the eigenvectors $\vec{X}_i$ of the Hessian matrix by solving the symmetric eigenvalue equation:

$$\sum_{k=1}^{3M} H^0_{jk} X_{ki} = \omega_i^2 m_j X_{ji} \quad , \; i,j = 1,\ldots,3M. \tag{3.4}$$

$3M - 6$ of the $3M$ eigenvectors, also denoted as normal mode vectors, describe the directions in which the atoms move during the i-th normal mode vibration. For the 6 normal mode vectors[1], which describe translation and rotation the corresponding eigenvalues, denoted as ω_i^2, are zero. If imaginary eigenmodes with $\omega_i^2 < 0$ occur, the structure is not in a local minimum, but in a metastable transition state, e.g., a saddle-point.

The set of cartesian coordinates $\vec{R}$ can be transformed into a set of normal coordinates $\vec{Q} = (Q_1, \ldots, Q_{3M})$ via

$$Q_j = \sum_{i=1}^{3M} X_{ij}(R_i - R_i^0).$$

With respect to the normal coordinates the system of equations 3.3 decouples into a set of independent equations:

$$\frac{d^2 Q_i}{dt^2} + \omega_i^2 Q_i = 0. \tag{3.5}$$

Each of these equations has the solution:

$$Q_i = A_i \cos(\omega_i t + \delta_i),$$

where A_i and δ_i denote the amplitude and phase of the harmonic oscillation.

In quantum mechanics the motion of the nuclei is described by the Hamilton operator (2.6). With respect to the normal mode coordinates Q_i and in the harmonic approximation the nuclear Hamiltonian $\hat{H}_{\text{nuc}}$ decouples into a sum over independent terms, which solely depend on one normal coordinate:

$$\hat{H}_{\text{nuc}} = V^0 + \frac{1}{2}\sum_{i=1}^{3M}\left[-\hbar^2 \frac{\partial^2}{\partial Q_i^2} + \omega_i^2 Q_i^2\right].$$

By using the product-Ansatz

$$\Psi(Q_1, \ldots, Q_{3M}) = \prod_{i=1}^{3M} \psi_{n_i}(Q_i)$$

and setting V^0 to zero one obtains $3M$ independent equations which correspond to the Schrödinger equation of the one-dimensional harmonic oscillator:

$$\frac{1}{2}\left[-\hbar^2 \frac{\partial^2}{\partial Q_i^2} + \omega_i^2 Q_i^2\right] \psi_{n_i}(Q_i) = E_{n_i} \psi_{n_i}(Q_i) \quad , \; n_i = 0, 1, 2, \ldots. \tag{3.6}$$

---

[1] 5 for linear structures

The solutions[2] are of the form:

$$\psi_{n_i}(Q_i) = \frac{1}{\sqrt{Q_i^0}} H_n\left(\frac{Q_i}{Q_i^0}\right) e^{-\frac{1}{2}\left(\frac{Q_i}{Q_i^0}\right)^2} \quad , \; Q_i^0 := \sqrt{\frac{\hbar}{\omega_i}} \tag{3.7}$$

where H_n is the n-th *Hermite polynomial* with

$$H_0(x) = 1 \tag{3.8}$$
$$H_1(x) = 2x. \tag{3.9}$$

The eigenvalues E_{n_i} of the one-dimensional harmonic oscillator are given by

$$E_{n_i} = \hbar\omega_i \left(n_i + \frac{1}{2}\right).$$

The energy of the atomic system described by $3M - 6$ harmonic oscillators in the state $(n_1, \ldots, n_{3M})$ equals

$$E(n_1, \ldots, n_{3M}) = V(\vec{R}^0) + \hbar \sum_{i=1}^{3M} \omega_i \left(n_i + \frac{1}{2}\right).$$

The energy spectrum is discrete and in the vibrational ground state, $(n_1, \ldots, n_{3M}) = (0, \ldots, 0)$, the vibrational energy is greater than zero, this is referred to as *zero-point energy.*

3.2 Infrared absorption and Raman scattering spectra

A cluster or molecule may exchange energy with a photon by changing its vibrational (or rotational) state. The corresponding frequencies typically lie in the IR region and, hence, the absorption of a photon is called infrared (IR) absorption.

In a semi-classical picture a photon with a frequency higher than any of the normal mode vibrations can be scattered at an atomic structure. The elastic process, where the photon does not change its energy, is called Rayleigh scattering. Inelastic scattering, where the photon interacts with one of the vibrational modes and changes its energy by $\Delta E = \pm h\nu_i$, is called Raman scattering. In this Section only the basic theory of IR and Raman spectroscopy is introduced. A detailed description along with a derivation of the equations presented can be found, e.g., in [30].

In the harmonic approximation, neglecting overtones due to nonlinear terms, only transitions with $\Delta n_i = \pm 1$ are allowed. Only photons the frequency $\nu_p = E_p/h$ of which matches any of the vibrational frequencies can directly interact with the cluster or molecule. The frequencies in the IR absorption and Raman scattering spectra are defined by the curvature of the atomic potential at the equilibrium geometry, or equivalent, the eigenvalues of the Hessian matrix. In contrast the probability for the absorption process depends on the change of the electric dipole moment $\vec{p}$ of

---

[2] A derivation can be found in almost any introductory textbook on Quantum Mechanics

the atomic structure during the corresponding vibration. The dipole moment $\vec{p}$ is defined as the distance between the center of the negative and of the positive charge times the charge q: $\vec{p} := q \cdot (\vec{R}^{+} - \vec{R}^{-})$. If the cluster or molecule has a center of symmetry, these two center coincide and the dipole moment vanishes. In a classical picture the normal mode vibrations accompanied by an oscillating dipole moment introduce an oscillating electric field. Contrariwise an external oscillating electric field may excite such a vibrational mode, if it oscillates with the same frequency. However, for a quantitative description of the absorption process a fully quantum mechanically treatment is more appropriate. For this, both the atomic system and the electromagnetic field have to be described by quantum theory. In the formalism of “second quantization” the electric field operator $\hat{G}$ is written as:

$$\hat{G} = \sum_{\lambda} \sqrt{\frac{\hbar\omega_\lambda}{2\varepsilon_0}} \left(\vec{A}_\lambda \hat{b}_\lambda + \vec{A}^*_\lambda \hat{b}^+_\lambda \right) \quad \text{with} \quad \vec{A}_\lambda = L^{-3/2} \vec{e}_\lambda e^{i\vec{k}_\lambda \cdot \vec{r}}.$$

Here $\hat{b}_\lambda$ and $\hat{b}^+_\lambda$ describe the annihilation (absorption) and creation (emission) of a photon with wavelength λ, respectively. The vector $\vec{e}_\lambda$ denotes the polarization and $\vec{k}_\lambda$ the corresponding wave-vector. The factor $L^{-3/2}$ normalizes the electromagnetic field, which is assumed to be in a periodic bounding cube of size L.

Two approximations based on the time and space scale on which the electromagnetic field varies significantly simplify the computation of the spectral intensities: Typical vibrational frequencies of clusters and molecules range from $3 \cdot 10^{12}$/s to $1.5 \cdot 10^{14}$/s (corresponding to wave numbers of $5000\,\mathrm{cm}^{-1}$ to $100\,\mathrm{cm}^{-1}$). The shortest wavelength of a photon with a frequency equivalent to that of a vibrational mode is about 10^{-6}m, that is 3 orders of magnitude larger than the dimensions of a small molecule. Therefore, at any fixed time the electromagnetic field of the photon can be considered constant over the whole molecule. The time scale for electronic relaxations ($\approx 10^{-17}$s) is about 2 orders of magnitude lower than the period of a nuclear vibration. It follows that the electromagnetic field varies slowly compared to the electronic time scale and can be considered constant in time.

Compared to the nuclear potential the influence of the electromagnetic field is assumed to be rather weak. In this case, it is possible to expand the Hamiltonian of the atomic system into a Taylor series up to 2nd order with respect to $\hat{G}$:

$$\begin{aligned} \hat{H}_{tot} &= \hat{H}_0 + \sum_{j=1}^{3} \frac{\partial \hat{H}_{tot}}{\partial \hat{G}_j} \hat{G}_j + \frac{1}{2} \sum_{i=1}^{3} \sum_{j=1}^{3} \frac{\partial^2 \hat{H}_{tot}}{\partial \hat{G}_i \hat{G}_j} \hat{G}_i \hat{G}_j && (3.10) \\ &= \hat{H}_0 - \hat{p}\hat{G} - \frac{1}{2} \hat{G}\hat{\alpha}\hat{G} && (3.11) \\ &= \hat{H}_M + \hat{H}_F + \hat{W}_1 + \hat{W}_2. && (3.12) \end{aligned}$$

Here, $\hat{H}_0 = \hat{H}_M + \hat{H}_F$ is the Hamiltonian of the atomic system and the independent electromagnetic field and the two operators $\hat{W}_1$ and $\hat{W}_2$ describe the interaction in first and second order, respectively. Due to this interaction transitions between an initial state $|\Psi_s\rangle$ of the atomic system (described as a set of harmonic oscillators) and of the electromagnetic field (described as another set of harmonic oscillators) and a final state $|\Psi_e\rangle$ can be introduced. Application of time-dependent perturbation theory yields as approximation for the transition-probability P_{se} *Fermi's "Golden Rule"*:

$$P_{se} = \frac{2\pi}{\hbar} \left| \langle \Psi_s | \hat{W}_1 + \hat{W}_2 | \Psi_e \rangle \right|^2 \delta(E_e - E_s).$$

Here, $|\Psi\rangle$ is the product of $|\Phi_n\rangle$, which describes the state of the i-th atomic harmonic oscillator, and of $|\ldots, n_\lambda, \ldots\rangle$, which describes the state of the photons. The effect of $\hat{W}_1$ on the electromagnetic field described by the "Golden Rule" is given by:

$$\langle \Psi_s | \hat{W}_1 | \Psi_e \rangle \propto \langle \Psi_s | \hat{p} \sum_\lambda \left(\vec{e}_\lambda \hat{b}_\lambda + \vec{e}^{\,*}_\lambda \hat{b}^+_\lambda \right) | \Psi_e \rangle.$$

The interaction with the atomic system may cause the annihilation (absorption) or the creation (emission) of a photon. This corresponds to infrared absorption or emission.

The effect of the second order operator $\hat{W}_2$, given by

$$\langle \Psi_s | \hat{W}_2 | \Psi_e \rangle \propto \langle \Psi_s | \sum_\lambda \sum_\mu \left(\vec{e}_\lambda \hat{b}_\lambda + \vec{e}^{\,*}_\lambda \hat{b}^+_\lambda \right) \hat{\alpha} \left(\vec{e}_\mu \hat{b}_\mu + \vec{e}^{\,*}_\mu \hat{b}^+_\mu \right) | \Psi_e \rangle,$$

describes four different processes: i) $(\hat{b}_\lambda \hat{b}_\mu)$ absorption of two photons with wavelengths μ and λ, ii) $(\hat{b}^+_\lambda \hat{b}^+_\mu)$ emission of two photons, iii) $(\hat{b}_\lambda \hat{b}^+_\mu)$ successive emission and absorption and iv) $(\hat{b}^+_\lambda \hat{b}_\mu)$ successive absorption of a photon with wavelength μ and emission of a photon with wavelength λ. The last term describes inelastic scattering of photons and corresponds to Raman scattering. The case $\mu < \lambda$ (the energy of the absorbed photon is higher than that of the emitted photon) is denoted *Stokes*-component, whereas the case $\mu > \lambda$ is denoted *Anti-Stokes*-component.

For comparisons with experimental IR spectra one has to calculate the IR absorption intensity I_i^{IR} for all modes i. In the double harmonic approximation, where a harmonic nuclear potential is assumed and the expansion of the dipole moment with respect to the normal mode coordinates Q_i is cut off after the linear term, Fermi's Golden Rule yields for the *first-order IR absorption intensity* of the i-th normal mode vibration:

$$I_i^{\mathrm{IR}} = \left| \frac{\partial \vec{p}}{\partial Q_i} \right|^2.$$

The atomic unit for the IR absorption intensity is

$$\left[I_i^{\mathrm{IR}} \right] = \left(\frac{\mathrm{Debye}}{\mathrm{\AA}} \right)^2 \mathrm{amu}^{-1},$$

with

$$\begin{aligned} 1\,\mathrm{\AA} &= 1 \cdot 10^{-10}\,\mathrm{m} \\ 1\,\mathrm{Debye} &= 3.33564 \cdot 10^{-30}\,\mathrm{C\,m} \\ 1\,\mathrm{amu} &= 1.66057 \cdot 10^{-27}\,\mathrm{kg}. \end{aligned}$$

The Raman spectra are determined by the differential Raman cross section. Within the double-harmonic approximation the differential cross section of the i-th mode for non-resonant Raman scattering is given, according to Fermi's Golden Rule, by

$$\frac{d\sigma_i}{d\Omega} = \frac{\hbar\omega_s^4}{2(4\pi\,\varepsilon_0\,c^2)^2}\,\frac{\bar{n}_i+1}{\omega_i}\,\frac{I_i^{\mathrm{Ram}}}{45}, \tag{3.13}$$

$$\text{with}\quad \bar{n}_i = \left[\exp\left(\frac{\hbar\omega_i}{kT}\right)-1\right]^{-1}, \tag{3.14}$$

where the Raman activity I_i^{Ram} is defined as

$$\frac{I_i^{\mathrm{Ram}}}{45} := \left| e_s\,\frac{\partial\hat{\alpha}}{\partial Q_i}\,e_0\right|^2 \tag{3.15}$$

$$= 45\left(\frac{\partial\hat{\alpha}}{\partial Q_i}\right)^2 + 7\left(\frac{\partial\hat{\beta}}{\partial Q_i}\right)^2 =: 45\alpha'^2 + 7\beta'^2\,. \tag{3.16}$$

The atomic units for the polarizability and for the Raman activity are

$$[\alpha] = \text{Å}^3$$
$$\left[I_i^{\mathrm{Ram}}\right] = \text{Å}^4\,\mathrm{amu}^{-1}.$$

The derivatives of the mean polarizability, α', and of the anisotropy, β', are defined by

$$\begin{aligned} 3\alpha' &= (\alpha'_{xx}+\alpha'_{yy}+\alpha'_{zz}) \quad \text{and} \\ 2\beta'^2 &= (\alpha'_{xx}-\alpha'_{yy})^2+(\alpha'_{xx}-\alpha'_{zz})^2+(\alpha'_{yy}-\alpha'_{zz})^2+6\,(\alpha'^2_{xy}+\alpha'^2_{xz}+\alpha'^2_{yz}), \end{aligned} \tag{3.17}$$

where α'_{ij} $(i,j=x,y,z)$ are the elements of $\hat{\alpha}'$ and a prime (') denotes the derivative with respect to the normal mode coordinate Q_i.

The ratio of the scattered intensities perpendicular and parallel to the incident polarization is called de-polarization ratio ρ_i and provides a measure for the anisotropy of the vibration,

$$\rho_i = \frac{3\beta'^2}{45\alpha'^2+4\beta'^2}\,. \tag{3.18}$$

The IR- and Raman intensities are calculated numerically as the derivatives of the forces with respect to a small external electric-field component. The derivatives with respect to a normal mode coordinate Q_i can be transformed via the normal mode eigenvectors X_k into derivatives with respect to the cartesian coordinates R_k.

$$\frac{\partial p_l}{\partial Q_i} = \frac{\partial p_l}{\partial R_k}X_{ki} = -\frac{\partial^2 E}{\partial G_l \partial R_k}X_{ki} = \frac{\partial F_k}{\partial G_l}X_{ki} \tag{3.19}$$

$$\frac{\partial \alpha_{mn}}{\partial Q_i} = -\frac{\partial^3 E}{\partial G_m \partial G_n \partial R_k}X_{ki} = \frac{\partial^2 F_k}{\partial G_m \partial G_n}X_{ki}. \tag{3.20}$$

Here, E and F_k denote the total energy and one force component, respectively. G_m denotes one component of the small external electric-field. The derivatives are computed numerically via forward and backward finite differences. This avoids errors

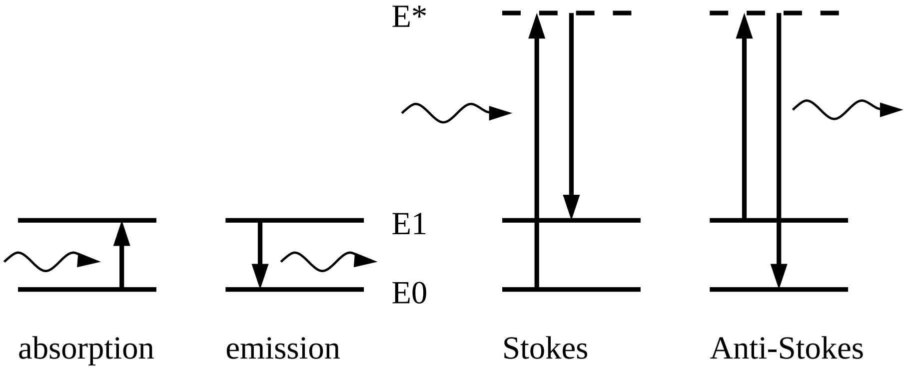

Figure 3.1: Illustration of IR absorption and emission (left) and Stokes and Anti-Stokes Raman scattering (right).

scaling proportional to the small electric-field component G_n. The implementation of IR- and Raman intensities into the scf DFT code *NRLMOL* is described in more detail in [16].

Finally, the processes responsible for infrared absorption and Raman scattering are illustrated in Figure 3.1. Here E_0 and E_1 denote the energies of the vibrational ground-state and of one fundamental vibrational mode, respectively. E^* denotes the energy of an intermediate virtual vibrational state.

The symmetry of a given cluster or molecule determines, if the dipole moment or polarizability varies during the i-th normal mode vibration. With the aid of *Group Theory* selection rules for IR and Raman transitions can be derived. A short introduction to the application of group theory to vibrational spectra and the labeling of vibrational modes is presented in Appendix B.

Chapter 4

Structure and properties of small silicon clusters

As of this writing only the structures of silicon clusters with less than eight atoms are well established. This could be achieved by a combination of theory and experiment, only. There is no direct experimental access to the geometry of a cluster. Even for small silicon clusters with 5 atoms (70 electrons) accurate *ab initio* calculations are computationally highly demanding and it is difficult to reliably predict the energetic order between several low-energy isomers. The measurements of vibrational frequencies via IR- or Raman spectroscopy and of photoelectron spectra combined with the corresponding results from calculations yield a consistent picture for the smallest clusters [31]. The properties of the smallest silicon clusters are summarized in the first Section of this Chapter. Many calculations and experiments have been performed on the larger clusters, but the interpretation of the results is still in progress. Theoretical results, including data accessible by experiments, on clusters with 9 to 14 atoms are presented in the second Section. The subsequent Chapters deal with the shape transition, indicated by mobility measurements, in the range from Si_{20} to Si_{30} and the bonding pattern as compared to bulk-like bonding for special larger cluster sizes.

4.1 Identified ground-state structures for Si_2 to Si_8

Calculated geometries, energies and vibrational frequencies obtained with the very same method and level of accuracy for several isomers of Si_2 up to Si_8 are available for a Hartree-Fock (HF) based code [32], a density-functional theory (DFT) based code [33] and the two density-functional theory based methods described in this work, namely the all-electron full potential scf code (*NRLMOL*) and the approximate tight-binding method (DFTB). By comparison to ultraviolet photoelectron spectra for Si_3^- to Si_{12}^- [34], to vibrationally resolved photoelectron spectra [35] for Si_3^- and Si_4^-, to infrared spectra [36] and to Raman spectra [31, 37] for Si_4, Si_6 and Si_7 the following ground-state structures could be identified.

Si_2: The silicon dimer exhibits two almost isoenergetic local minima at bonding distances of 2.2 and 2.3 Å. This is caused by a level-crossing between the HOMO and the LUMO at about the minimum distance. The DFT-LDA binding energy of $-3.56\,\mathrm{eV}$ ($r_0 = 2.2\,\text{Å}$) is 0.35 eV lower than the experimental value of $-3.21\,\mathrm{eV}$ [38]. This is due to the overbinding common in the LDA. Comparison to the DFT-LDA cohesive energy for the silicon bulk of $-5.2\,\mathrm{eV/atom}$ and the experimental value of $-4.6\,\mathrm{eV/atom}$ [39], which correspond to $-2.6\,\mathrm{eV/bond}$ and $-2.3\,\mathrm{eV/bond}$, shows that the bond in the dimer is 37 % (DFT-LDA) or 53 % (exp.) stronger than in the crystal, indicating the existence of π-bonds in the dimer. The electronic ground state is a triplet state.

Si_3: The isosceles triangle is the most stable isomer of Si_3. Since the DFT-LDA binding energy of the equilateral triangle lies less than 0.1 eV higher, it is difficult to determine the most stable isomer by theory alone. The binding energy of Si_3 is known experimentally to be $-7.6 \pm 0.2\,\mathrm{eV}$ [40] compared to $-8.9\,\mathrm{eV}$ within DFT-LDA.

Si_4: The planar rhombus is the lowest energy configuration of Si_4. The length of the shortest diagonal is 2.4 Å only. Two atoms are threefold and the other two atoms are twofold coordinated. Within DFT-LDA the rhombus is 2.5 eV more stable than the tetrahedron [33]. The rhombus can be found as a subunit in many of the larger clusters.

Si_5: Si_5 is a trigonal bipyramid with D_{3h} symmetry. Only the six bonds from the two apex atoms to the atoms in the triangle are strong with a length of 2.3 Å. In DFT-LDA the distance of 3.0 Å between the apex atoms is about the same as the side length of the triangle.

Si_6: The exact structure of the six atom cluster is a challenge even to very accurate *ab initio* methods. The principal structure is a tetragonal bipyramid with D_{4h} symmetry, but there exist two slightly distorted forms of it that have binding energies within 0.02 eV of each other. A vibrational analysis indicates a flat potential in the direction of the distortion. The experimental Raman spectra matches best the D_{4h} symmetric structure [31, 37].

Si_7: A pentagonal bipyramid is the lowest energy isomer for Si_7. Within the pentagon the atomic distance is 2.48 Å, about 0.1 Å larger than the bulk Si–Si bond length of 2.35 Å. Each of the apex atoms has five equivalent bonds of lengths 2.46 Å to the atoms in the pentagon and a weak bond of length 2.51 Å to the other apex atom. The two apex atoms along with any two adjacent atoms in the pentagon form a near tetrahedral geometry, therefore, this cluster is best considered as five tetrahedra sharing a common edge (the fivefold rotation axis).

Si_8: A Jahn-Teller distorted bicapped octahedron with C_{2h} symmetry is known from HF- and DFT-LDA calculations to be the ground-state of Si_8. Here, two opposite faces of the octahedron are capped, which is favorable compared to capping adjacent faces. Four other possible candidates for Si_8 have one or more imaginary eigenmodes. They represent transition states and no local minima [33].

The identification of the ground-state structures of Si_4, Si_6 and Si_7 by comparison of calculated and measured Raman spectra as presented by Honea et al. [37] is illus-

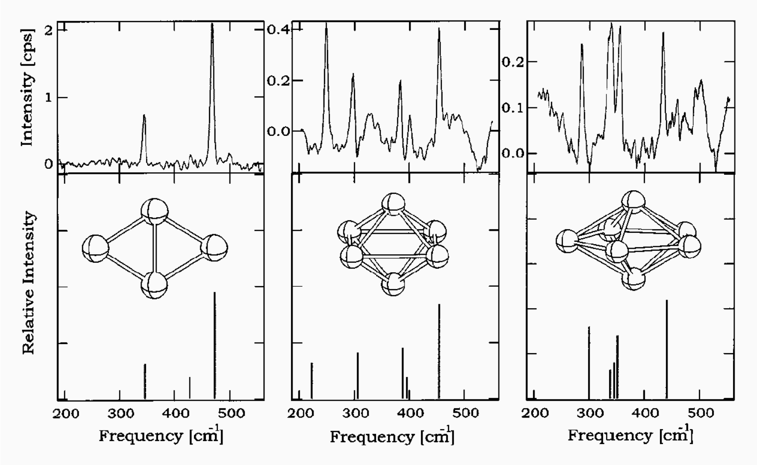

Figure 4.1: Measured spectra, calculated spectra and predicted structures of Si_4, Si_6, and Si_7. This Figure is taken from Ref. [37].

trated in Fig. 4.1. The spectra of the size-selected, matrix-isolated silicon clusters have been measureded with the surface-plasmon-polariton enhanced Raman spectroscopy, which yields well-resolved vibrations in agreement with predictions based on the Hartree-Fock method with quadratic configuration interaction (HF-QCISD). Among all the Raman active modes predicted for Si_4, Si_6 and Si_7, only the relatively weak b_{3g} mode of Si_4 has not been observed. All the other experimentally seen modes show a mean absolute deviation of only $7\,\mathrm{cm}^{-1}$ between theory and experiment. The authors in [37] mention that consideration of other possible structural isomers yields qualitative and quantitative results which are completely inconsistent with the experimental spectra. They also report that *"numerous attempts to measure the Raman signature of Si_5 and Si_{10} were unsuccessful, presumably because of low Raman cross sections and a limited signal-to-noise ratio."*

Cluster	(sym.)	E_{TB}	E_{scf}	Gap_{TB}	Gap_{scf}
Si2	$(D_{\infty h})$	-1.94	-1.78	2.50	2.75
Si3	(C_{2v})	-2.98	-2.97	1.87	1.01
Si4	(D_{2h})	-3.49	-3.54	1.45	1.08
Si5	(D_{3h})	-3.77	-3.83	1.70	1.98
Si6	(C_{2v})	-3.93	-4.04	1.34	2.11
Si7	(D_{5h})	-4.06	-4.19	1.51	2.10
Si8	(C_{2h})	-4.07	-4.12	1.16	1.42

Table 4.1: Binding energies with respect to spin polarized atoms in eV/atom and HOMO–LUMO gaps in eV for small silicon clusters as calculated within DFTB and scf-DFT-LDA.

For larger clusters the *ab initio* calculations become very time consuming. To scan an area as large as possible of the Born-Oppenheimer surface for such clusters the usage of an efficient approximate approach, like the density-functional based tight-binding (DFTB) method, is required. To ensure accurate results for the geometry and energy of the larger clusters the reproduction of the corresponding scf-DFT-LDA variables for the smaller clusters is a minimum requirement. For small silicon clusters, up to Si_8, one obtains within the DFTB method the same equilibrium structures as Fournier et al. [33] and Pederson et al. [41]. The maximum deviations in bond lengths and angles are smaller than 10%. Table 4.1 compares the cohesive energies and gaps between the *Highest Occupied Molecular Orbital* (HOMO) and the *Lowest Unoccupied Molecular Orbital* (LUMO) from the DFTB calculations with the corresponding values from scf-DFT-LDA calculations. The agreement for the cohesive energies with a maximum error of 0.16 eV/atom for Si_2 is very good. However, the HOMO–LUMO gaps are only in qualitative agreement, but these deviations decrease for the larger clusters (see below).

Cluster	ZPE/ eV	E/ eV	E_{ZP}/ eV
Si_{7a}	0.29	-22.34	-22.05
Si_{7b}	0.30	-21.61	-21.31
Si_{7c}	0.28	-20.55	-20.28
Si_{8a}	0.29	-24.05	-23.76
Si_{8b}	0.33	-24.65	-24.32
Si_{8c}	0.33	-24.39	-24.07
Si_{8d}	0.33	-24.12	-23.78
Si_{8e}	0.32	-24.02	-23.69
Si_{10a}	0.46	-32.15	-31.69
Si_{10c}	0.43	-33.19	-32.76

Table 4.2: Zero-point energies (ZPE) as calculated within HF/6-31G*, binding energies (E) and zero-point corrected binding energies (E_{ZP}) as calculated within HF-MP4/6-31G* for various isomers of Si_7 to Si_{10}. All results and the labeling of the clusters are taken from Ref. [32].

The total energies E^0_{tot} (and also the cohesive energies) of the equilibrium structures have to be corrected by the zero-point energy. Every vibrational mode with frequency ω_i contributes the energy $E_i = 1/2\,\hbar\omega_i$ to the zero-point corrected total energy $E^{\mathrm{ZP}}_{\mathrm{tot}}$:

$$E^{\mathrm{ZP}}_{\mathrm{tot}} = E^0_{\mathrm{tot}} + \frac{1}{2}\sum_{i=1}^{3M-6} \hbar\omega_i .$$

In general the differences in the zero-point corrections of different isomers are much smaller than the differences in the total energies and the energetic order with and without zero-point correction is the same. For several isomers of Si_7 to Si_8 this is proved in Table 4.2. The binding energies calculated by Raghavachari et al. with the Hartree-Fock method under inclusion of correlation effects by Moeller-Plesset perturbation theory (HF-MP4) with a 6-31G* basis set are compared to the corresponding zero-point corrected binding energies [32]. The vibrational frequencies and zero-point energies were calculated on the HF level (without correlation). In none of the cases the zero-point correction changes the energetic order of the isomers. Therefore, the energies without zero-point corrections are reported in the following.

4.2 Structure and energies of Si_9 to Si_{14}

None of the Si_n structures for $n > 7$ has been verified experimentally to date. Experimental data for size-selected clusters in the gas-phase larger than Si_7 have been provided for photoelectron spectra of anions [34, 42, 43, 44], for fragmentation pathways and dissociation energies of cations [45, 46, 47, 48], for chemical reactivities [49], and for ionization potentials of the neutrals [50, 51, 52]. The observed fragmentation patterns of both cations and anions are quite complex. First, all species with $8 < n \leq 70$ (at least) undergo fission rather than evaporation. That is, both primary dissociation products contain a relatively large number of atoms, one of them always 6 to 11 atoms. Second, the preferred fragments are specific to the size and the charge state (+1 or -1) of the original ion. The products of collision-induced dissociation of the cations Si_n^+ contain mainly Si_6, Si_7 or Si_{10} fragments, either in neutral or positive charge state [47, 48]. This is in agreement with the calculated cohesive energies for Si_2 to Si_{14} which indicate that Si_6, Si_7 and Si_{10} are quite stable (see Fig. 4.2).

Cluster	(sym.)	E_{TB}	E_{scf}	Gap_{TB}	Gap_{scf}
Si9a	(C_{2v})	-4.176	-4.234	1.904	1.988
Si9b	(C_{2v})	-4.126	-4.183	1.846	1.551
Si9c	(D_{3h})	-4.031	-4.097	0.173	0.397
Si10a	(C_{3v})	-4.242	-4.357	1.706	2.125
Si10b	(T_d)	-4.129	-4.286	3.405	2.136
Si11a	(C_s)	-4.203	-4.274	1.214	1.041
Si11b	(E)	-4.210	-4.262	1.009	0.922
Si11c	(C_s)	-4.205	-4.259	1.330	1.073
Si12a	(C_s)	-4.228	-4.274	0.925	0.593
Si12b	(E)	-4.250	-4.267	0.862	0.940
Si13a	(C_{3v})	-4.204	-4.305	1.451	1.606
Si13b	(C_{2v})	-4.277	-4.291	1.332	0.787
Si14a	(C_s)	-4.328	-4.372	1.531	1.774
Si14b	(C_s)	-4.300	-4.332	1.029	1.323
Si14c	(D_{3h})	-4.283	-4.253	1.095	0.896
Si14d	(C_{3v})	-4.179	——	0.000	——

Table 4.3: Binding energies with respect to spin polarized atoms in eV/atom and HOMO–LUMO gaps in eV for several isomers from Si_9 to Si_{14} as calculated within DFTB and scf-LDA.

Considering larger clusters with 9 to 14 atoms, an extensive search for the equilibrium structures with different seed clusters obtained by edge or face capping

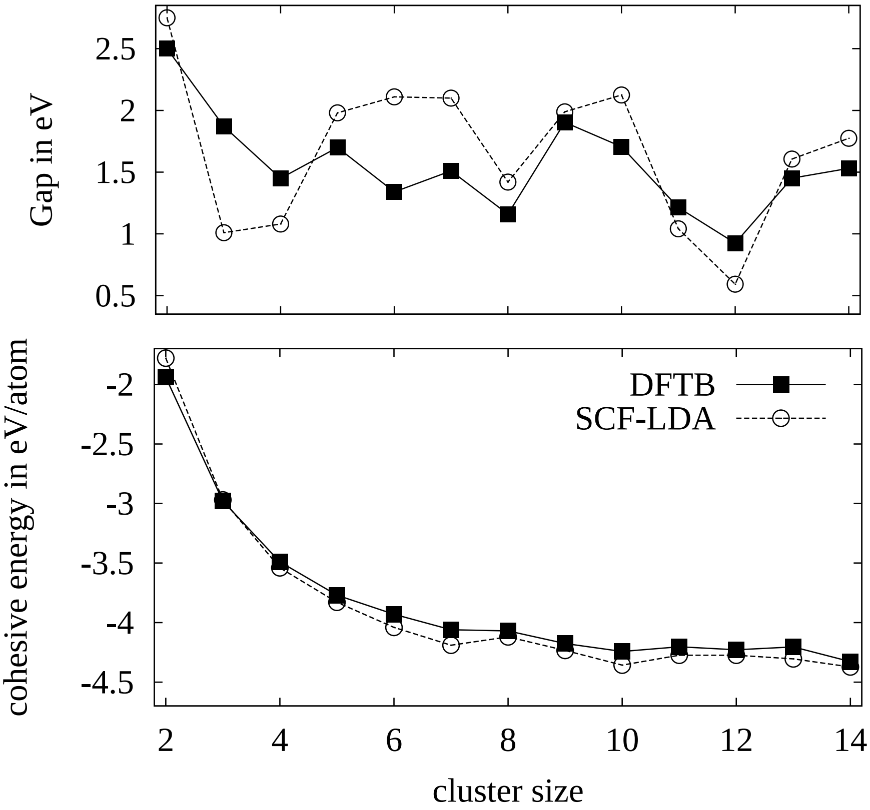

Figure 4.2: HOMO–LUMO gaps in eV (top) and cohesive energies in eV/atom (bottom) as calculated within DFTB and SCF-LDA as a function of cluster size.

of smaller stable clusters or with clusters taken from the literature has been performed. The geometries of these structures have been optimized with the DFTB method by applying either a stochastic molecular-dynamic quenching or conjugate gradient relaxation until the maximum force on every atom dropped below 10^{-4} Hartree/Bohr. At least the two most stable[1] structures within DFTB were then relaxed with the scf-LDA *NRLMOL* code using a 6s5p3d basis set (i.e. 6 s-like, 5 p-like and 3 d-like contracted Gaussian) and the Perdew-Wang '91 exchange-correlation functional. The minimum allowed force during these conjugate gradient procedures was 10^{-3} Hartree/Bohr.

Within scf-LDA the cohesive energies were calculated with respect to spin polarized isolated atoms. Since the DFTB method does not take spin into account, the DFTB energies were shifted by the LDA spin-polarization energy of 0.66 eV. The cohesive energies and highest occupied to lowest unoccupied molecular orbital (HOMO–LUMO) gaps for the lowest energy clusters are summarized in Table 4.3. The variation of both quantities with cluster size is depicted in Figure 4.2. Si_7, Si_{10}, and Si_{14} are more stable than their neighbors. The order of the DFTB cohesive

---

[1] most stable in the sense of lowest-energy and not lowest reactivity

energies of the lowest energy isomers for a given cluster size agrees with the scf-LDA results for all smaller clusters and Si_9, Si_{10} and Si_{14} but is reversed for Si_8, Si_{11}, Si_{12} and Si_{13}. However, for the three latter clusters the differences in the scf cohesive energies are smaller than 0.02 eV/atom, and, therefore, challenge the accuracy of the DFTB approach. The variation of the HOMO–LUMO gap as calculated within DFTB with increasing cluster size, n, is in good agreement with the scf-LDA calculations for $n > 7$. The quantitative differences for Si_8 to Si_{14} are at maximum 20%, and the deviations are smaller for the larger clusters. An accurate description of the eigenvalues of unoccupied orbitals often fails with a minimum basis set.

In the following discussion of the results for each cluster size the self-consistent calculated cohesive energies and HOMO–LUMO gaps, obtained with *NRLMOL*, are considered. The geometries of the silicon clusters are depicted in Fig. 4.3.

Si_9: Two stacked distorted rhombi with an additional atom capped on top form the lowest-energy cluster (Si_{9a}, see Fig. 4.3a). This structure has C_{2v} symmetry and is 0.05 eV/atom more stable than the distorted tri-capped trigonal prism Si_{9b}, first proposed by Ordejon et al. [53] as the most stable structure of Si_9. Raghavachari and Rohlfing [32] calculated by using a HF-MP4(SDQ)/6-31G* algorithm nearly identical energies for a tri-capped trigonal prism $Si_{9c}(D_{3h})$, a tri-capped octahedron (C_{3v}), and a distorted tri-capped octahedron (C_s). They found the latter cluster to be only 0.014 eV/atom more stable than the first one and only 0.011 eV/atom more stable than the second. Ordejon et al. found by using a non-scf multi-center TB-approach [54] an energy difference of 0.10 eV/atom between the distorted tri-capped octahedron (C_s) and the distorted tri-capped trigonal prism $Si_{9b}(C_{2v})$. The difference in energy between the triplet state of the tri-capped trigonal prism (D_{3h}) (which is nearly isoenergetic to the distorted tri-capped octahedron (C_s)) and Si_{9b} as calculated with NRLMOL is 0.09 eV/atom. This is in agreement with the energy difference between the three structures considered by Raghavachari and Rohlfing and the structure proposed by Ordejon. However, none of these authors considered the candidate Si_{9a} (C_{2v}). It is possible that a similar structure has been described in earlier works of Ballone et al. [55], Wales [56] and Vasiliev et al. [57], but no detailed information about geometrical parameters is given in those works. Si_{9a} has a large gap of 2.0 eV within the scf-LDA formalism.

Si_{11}: A structure proposed by Lee *et al.* [58] using a TB-method, Si_{11a}, can be confirmed with DFTB and *NRLMOL* to be the most stable Si_{11} cluster. Lee et al. describe the geometry as a distorted tri-capped tetragonal anti-prism, but it may also be seen as a distorted penta-capped trigonal prism (see Fig. 4.3f). The three rectangular faces of the prism, one edge and one triangular face are capped, which results in C_s symmetry. The relaxation out of different starting structures for Si_{11} with the DFTB method has also spawned another cluster, Si_{11b}, having no symmetry at all. This cluster is within scf-LDA only 0.01 eV/atom less stable than Si_{11a}. It is a distorted 4-5 prism, with two atoms capping the fivefold ring (see Fig. 4.3g). Structure Si_{11a} is more stable by 0.02 eV/atom than the distorted tetragonal anti-prism $Si_{11c}(C_s)$ with both tops and one roof-face capped found by Rohlfing and Raghavachari [59]. However, Liu et al. [60] find by using the DFT-GGA the C_{2v} geometry in [59] and an isoenergetic C_s isomer not previously described lower in energy than Si_{11a} by 0.25 eV. Grossman and Mitas [61] considered three stacked triangles with

capped tops (D_{3h}) for Si_{11}. Within DFTB this cluster is metastable with a binding-energy 0.03 eV/atom higher than that of Si_{11a}. After small displacements in the direction of the occuring imaginary eigenmodes this structure converges to Si_{11b}.

Si_{12}: Ramakrishna et al. presented results of their extensive search for the ground state of Si_{12} [62]. They report on six isomers, which differ by only 0.02 eV/atom in cohesive energies, as calculated within the DFT-LDA. These isomers can all be described either as hexa-capped trigonal prisms or anti-prisms with different faces or edges capped. Additionally, they report on seven other structures with the highest energy cluster being 0.11 eV/atom less stable than the lowest-energy one. For their isomer 2 (Si_{12a}), a hexa-capped distorted trigonal prism with (C_s) symmetry (see Fig. 4.3i), a cohesive energy of -4.27 eV/atom is obtained with the all-electron full potential scf DFT-LDA code *NRLMOL*. The search with DFTB revealed also another, non-symmetric, structure Si_{12b} (see Fig. 4.3j) being only 0.01 eV/atom less stable than their isomer 2. This structure, a stacking sequence of a distorted rhombus, a fourfold ring, a triangle and a single atom, does not match any of their isomers.

Si_{13}: The most stable structure of Si_{13} consists of four stacked triangles with a cap on top. QMC [63] and DFT-LDA [41, 64] calculations found this structure Si_{13a} to be favoured against the icosahedral form of Si_{13}. From the MD search with DFTB the cohesive energy of another structure can be predicted to be very close to that of the lowest energy cluster. This structure, Si_{13b}, has C_{2v} symmetry and can be described as a distorted tri-capped trigonal prism with an additional rhombus capped on one edge of the prism (see Fig.4.3l). The energy difference between these two structures within the DFT-LDA is only 0.01 eV/atom, whereas Grossman and Mitas found an energy difference of 0.3 eV/atom between the icosahedral cluster and Si_{13a} [63]. The HOMO–LUMO gap of structure Si_{13b} is only half as large as that of the most stable cluster Si_{13a}.

Si_{14}: Only a few structures for Si_{14} have been presented in the literature. Here, a stacking sequence of two distorted rhombi, one fivefold ring and an atom on top (Si_{14a}) is suggested as a candidate for the groundstate structure. In this cluster the longer axes of the two stacked rhombi are perpendicular, as can be seen in Figure 4.3m. There exists also a locally stable cluster, Si_{14b}, with similar geometry but parallel longer axes, which is only 0.04 eV/atom higher in energy. Another local stable isomer is the octa-capped trigonal prism with D_{3h} symmetry (Si_{14c}). The rectangular faces of the prism are capped by a six-fold ring and both triangular faces are capped by one atom each (see Fig.4.3o). This geometry is 0.12 eV/atom less stable than the lowest energy candidate. One interesting feature of this structure are the six fivefold rings, which also occur as part of the sixfold rings in the tetrahedral bulk structure. Si_{14c} has 30 bonding-angles very close to the tetrahedral bond angle of 109^o. For the three structures Si_{14a}, Si_{14b}, and Si_{14c} the HOMO–LUMO gaps are 1.77, 1.32, and 0.90 eV respectively. Within the DFTB method the lowest energy cluster is more stable by 0.15 eV/atom than the four stacked triangles with capped tops (Si_{14d}) investigated by Grossman *et al.* [61]. Structure Si_{14a} has been confirmed to be the most stable isomer of Si_{14} by DFT-GGA calculations [60].

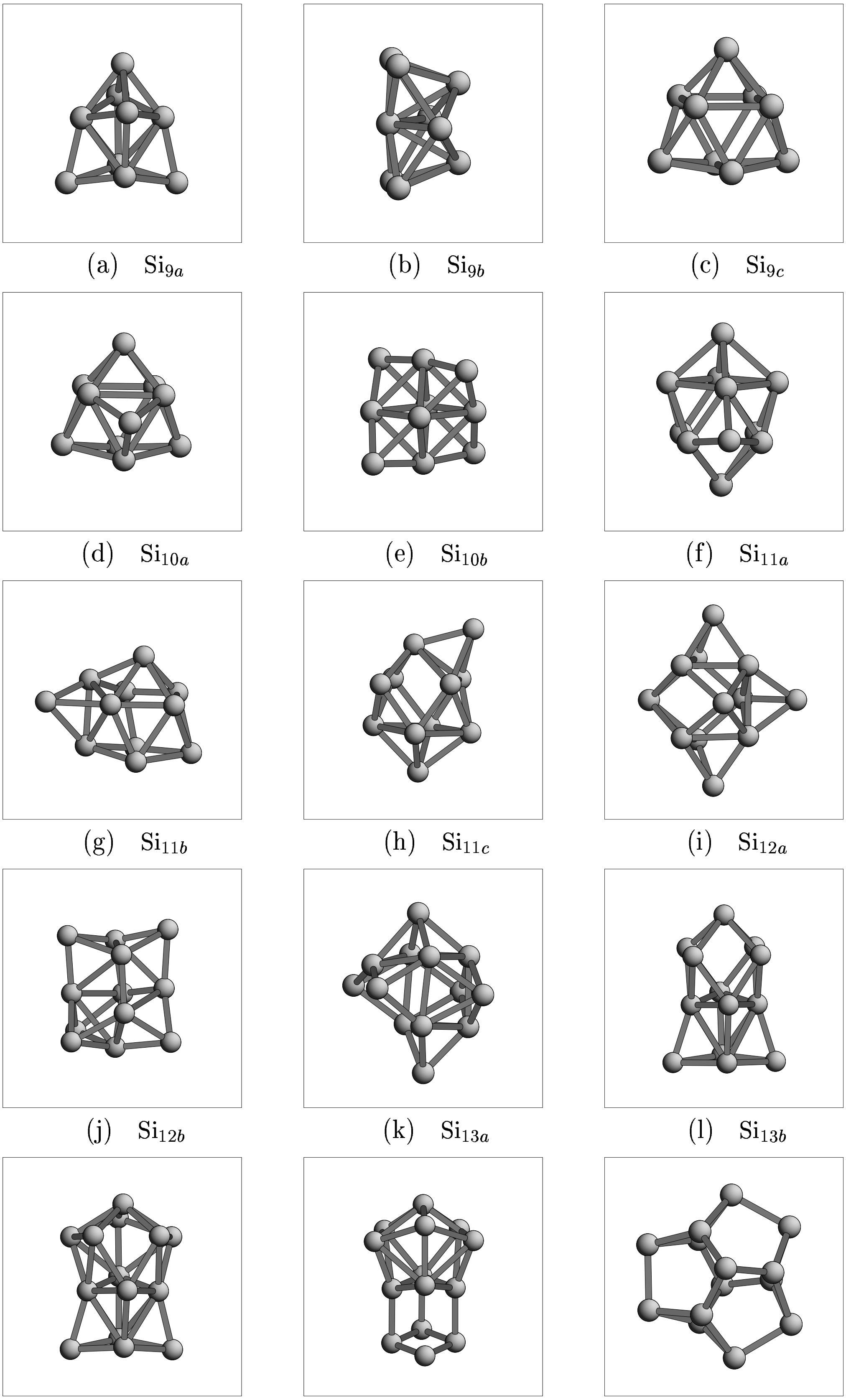

(a) Si$_{9a}$ (b) Si$_{9b}$ (c) Si$_{9c}$

(d) Si$_{10a}$ (e) Si$_{10b}$ (f) Si$_{11a}$

(g) Si$_{11b}$ (h) Si$_{11c}$ (i) Si$_{12a}$

(j) Si$_{12b}$ (k) Si$_{13a}$ (l) Si$_{13b}$

(m) Si$_{14a}$ (n) Si$_{14b}$ (o) Si$_{14c}$

Figure 4.3: Low-energy isomers of Si$_9$ to Si$_{14}$.

Ho and coworkers have presented candidates for the ground state isomer of silicon clusters from Si_{11} to Si_{20} using a Genetic Algorithm and a tight-binding potential [65]. Similar to the approach described here, they further relaxed their new candidates within the scf-LDA. Their most stable structures for Si_{12} and Si_{14} are identical to the clusters presented above, but for Si_{13} Ho et al. calculated the cluster Si_{13b} to be more stable than cluster Si_{13a} by 0.02 eV/atom. The small deviations in binding energies and HOMO–LUMO gaps between both LDA approaches are probably due to the use of different basis sets and different functionals for the exchange and correlation potential. In this work the Perdew-Wang '91 exchange-correlation functional was used, whereas in [65] they used the Vosko-Wilk-Nusair functional.

All lowest-energy structures considered here, with the exception of Si_{9a}, have a tri-capped trigonal prism as the common subunit. This building block can also be described as a stacking sequence of a rhombus, a rectangle and a single atom capped on top. In the most stable 9 atom cluster Si_{9a} the rectangle is replaced by a rhombus. The tetra-capped trigonal prism Si_{10a} (C_{3v}) can be obtained by capping one top of the tri-capped trigonal prism. Further capping of one edge of the prism leads to the Si_{11a} cluster. Capping of the second triangle followed by a displacement of the edge capping atom of Si_{11a} to one side of the trigonal prism results in structure Si_{12a}. In Si_{13b} a rhombus is attached to four atoms of the tri-capped trigonal prism. Si_{13a} can be obtained by adding a further triangle to the three stacked triangles and capping the top. Si_{14a} is very similar to Si_{13b}, the rectangle in the building block is expanded to a fivefold ring in Si_{14a}. Si_{14c} can be built by replacing the capping atoms of the tri-capped trigonal prism with three dimers and capping each of the two triangular faces with one atom. The dimers lie in the mirror plane perpendicular to the principal axis. All low-energy structures with 11 to 14 atoms considered here have various five- and even sixfold coordinated atoms. The overall bonding scheme is quite different from the bulk tetrahedral symmetry. However, each structure has numerous bond angles close to 109°.

4.3 Vibrational signatures and polarizabilities of Si_9 to Si_{14}

Due to the small differences in cohesive energies for the low-energy clusters, additional theoretical data for the identification of the ground-state geometry of a cluster are highly useful. Calculation of the vibrational spectra not only confirms the stable stationary points on the Born-Oppenheimer surface, but along with the Raman activities and IR absorption intensities also provides unique spectral information on chemical bonding, which can be used for comparisons with experiment. This approach has already been successfully applied to identify smaller clusters [31, 37, 36].

To determine the vibrational modes of the clusters the method discussed in Chapter 3 and in Refs.[41, 66, 67, 68] has been applied to Si_9 and Si_{11} to Si_{14}. For the numerical computation of the vibrational frequencies with *NRLMOL* displacements of 0.05 a_B and for the computation of the dynamical response to an external electric field small electric field components of $\Delta G = 0.005$ a.u. were used (see Chapter 3). As described in [66], the scf-DFT method yields reliable results for vibrational frequencies, IR intensities and Raman activities of small silicon clusters with a (6s5p3d) basis set and within the LDA. Since the IR and Raman activities depend on second and third order total energy derivatives with respect to the normal mode coordinates and external electric field components, extremely well converged energies and electronic densities are required. Hence, for the calculation of the vibrational frequencies, the total energy was converged during the scf iteration to 10^{-6} Hartree and for the calculation of the intensities and activities to 10^{-8} Hartree with respect to the electronic degrees of freedom.

Cluster	(sym.)	Frequencies/(cm^{-1})
Si_{9a}	(C_{2v})	$56(b_2), 109(b_1), 120(a_2), 164(a_1), 219(a_1), 225(b_2), 256(b_1), 262(b_2), 284(a_1), 285(a_2), 290(b_1), 292(a_1), 322(a_1), 332(a_1), 335(b_1), 373(a_2), 397(b_1), 405(a_1), 437(b_2), 468(b_2), 486(a_1)$
Si_{11a}	(C_s)	62, 111, 115, 129, 149, 197, 208, 223, 232, 251, 253, 261, 268, 278, 281, 298, 304, 306, 350, 354, 358, 366, 397, 411, 413, 439, 493
Si_{12a}	(C_s)	46, 110, 139, 163, 166, 178, 196, 197, 213, 228, 234, 238, 243, 255, 264, 266, 288, 291, 313, 322, 336, 342, 345, 390, 407, 425, 471, 488, 506
Si_{13b}	(C_{2v})	$45(b_2), 58(b_1), 100(a_2), 136(b_1), 145(a_1), 158(a_2), 168(b_2), 176(b_1), 189(a_1), 199(b_2), 204(a_1), 229(a_2), 230(a_2), 230(b_1), 233(a_1), 255(a_1), 257(b_2), 259(b_2), 279(a_2), 289(a_1), 302(b_2), 311(b_1), 330(a_1), 349(b_1), 351(a_1), 353(a_2), 356(b_2), 360(a_2), 373(a_1), 394(a_1), 405(b_2), 408(b_1), 446(b_1), 454(a_1)$
Si_{14a}	(C_s)	54, 99, 103, 115, 142, 154, 180, 188, 193, 196, 213, 222, 223, 230, 240, 259, 269, 273, 283, 286, 290, 298, 306, 315, 339, 356, 356, 365, 367, 370, 401, 410, 428, 447, 463, 480

Table 4.4: Vibrational frequencies of lowest-energy silicon clusters as calculated within DFT-LDA.

In the following paragraph the IR and Raman spectra of the candidates for the ground state structures of Si_9, Si_{11}, Si_{12}, Si_{14}, and for the second stable structure of Si_{13} will be discussed. The corresponding spectra for the most stable isomer Si_{13a} have already been presented in Ref. [41]. Table 4.4 contains the vibrational frequencies of these clusters labeled by the symbol of the irreducible representations (see the Appendix) for clusters with more than two symmetry elements. In the figures with the vibrational spectra the lower panel shows the Gaussian-broadened vibrational density of states (VDOS), obtained by centering a Gaussian-function with a FWHM of 6 cm^{-1} on each of the normal mode frequencies. In the other panels the VDOS is weighted by the IR intensity and Raman activity of the various modes. For the Raman spectra the activities for parallel and perpendicular polarization are plotted.

Si_{9a}: This cluster has C_{2v} symmetry and therefore has no degenerate eigenmodes. All modes are Raman active, but only the modes which transform as the irreducible representations a_1, b_1, and b_2 are IR active. Therefore, one expects a maximum number of 21 Raman active modes and a maximum number of 18 IR active modes. On the left hand side of Figure 4.4 the predicted IR and Raman spectra for Si_{9a} are presented.

The IR spectrum has its strongest peak at 486 cm^{-1} and six other strong peaks are located in the range from 109 to 468 cm^{-1}. The strongest IR mode corresponds to an anti-phase vibration of the atom on top relative to the left and right atom of the upper rhombus (see Fig. 4.3a) and of the left and right atoms in the upper rhombus relative to the left and right atoms in the lower rhombus. The maximum IR intensity of 0.16 $(D/\,\text{Å})^2/\,\mathrm{amu}$ is small compared to some spectra of other structures like Si_4 [1.34 $(D/\,\text{Å})^2/\,\mathrm{amu}$] or Si_{10}(TCO) [1.5 $(D/\,\text{Å})^2/\,\mathrm{amu}$] in Ref. [41]. In the experimental spectra of Ref. [36] only the modes corresponding to calculated IR intensities greater than approximately 0.15 $(D/\,\text{Å})^2/\,\mathrm{amu}$ (within DFT-LDA) could be identified.

Si_{9a} has a fully polarized strongest Raman peak at 405 cm^{-1} and one strong peak at 56 cm^{-1}, which is nearly non-polarized (The scaling is different in the Raman perpendicular and Raman parallel DOS). Mainly the atoms in the upper rhombus and the atom on top (see Fig. 4.3a) contribute to the low-frequency non-polarized Raman mode. The atom on top moves horizontally in the opposite direction than the two atoms (in front and in the back) of the upper rhombus. The high-frequency polarized Raman mode corresponds to a breathing mode in which all atoms participate.

Si_{9a} provides a good example to illustrate that the selection rules derived from Group Theory (see the Appendix) only give a necessary, but not a sufficient, criterion for a vibrational mode to appear in the measured IR or Raman spectra. Only seven out of the 18 allowed IR active modes have an IR intensity greater than 0.04 $(D/\,\text{Å})^2/\,\mathrm{amu}$. The intensities of all other modes are far too weak to be detected by experiment. Only in some cases one can distinguish between two different isomers with the aid of the selection rules alone. In many cases the explicit calculation of the spectra is essential.

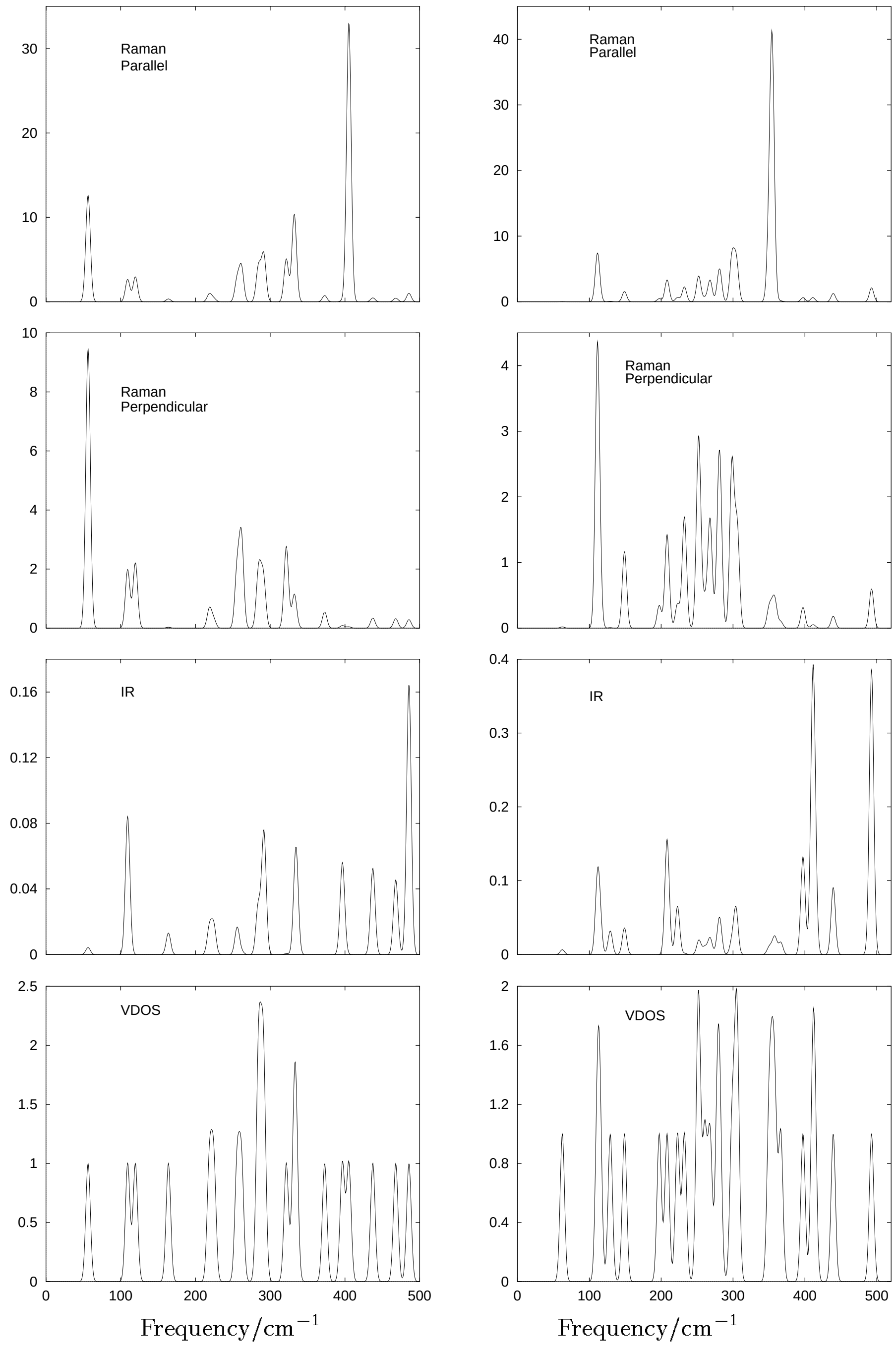

Figure 4.4: VDOS and simulated IR and Raman spectra of the Si_{9a} structure (left) and of the Si_{11a} structure (right). IR intensities are in $(Debye/\,\text{Å})^2/$ amu and Raman activities are in $\text{Å}^4/$ amu.

Si_{11a}: This structure has only one reflection plane, hence, all 27 modes are nondegenerate and are both Raman and IR active. As can be seen on the right hand side of Figure 4.4, Si_{11a} has two nearly equally strong IR active modes at high energies (411 and 493 cm^{-1}) and only one partly polarized strong Raman peak at 354 cm^{-1}. All Raman peaks observed in the direction perpendicular to the polarization plane have very low intensities. Since the only difference between Si_{11a} and Si_{10a} (TTP) is the additional atom capped on one edge of the trigonal prism, it is interesting to see the influence of the additional atom on the IR and Raman spectra. The spectra for Si_{10a} is given on the left hand side of Fig. 4.5. Both structures have one highly active and strongly polarized Raman mode at about 380 cm^{-1} (Si_{10a}) and at 354 cm^{-1} (Si_{11a}). For Si_{11a} this Raman mode corresponds to a breathing mode in which all atoms participate. The Raman-perpendicular spectra is very weak for both clusters. The IR spectra of both structures are weak, too, but the highest energy IR active modes occur at higher energies for Si_{11a}.

Si_{12a}: Like Si_{11a} this cluster has only nondegenerate vibrational modes, which are all Raman and IR active. The IR and Raman spectra of Si_{12a} are depicted on the left hand side of Figure 4.6. The IR spectrum is rather weak and may be hard to detect experimentally. The strongest, polarized, Raman peak for Si_{12a} is at 336 cm^{-1} and corresponds roughly to a breathing mode. Two other strong Raman peaks appear at 196 and 342 cm^{-1}, the latter is obscured by the 336 cm^{-1} peak in the diagram.

Si_{13b}: The second most stable configuration of Si_{13} has C_{2v} symmetry and, therefore, has a maximum number of 33 Raman and 27 IR active modes. The IR absorption intensities are rather weak and may be difficult to observe in experiment. The most striking feature in the Raman spectra is a strong peak with low energy (45 cm^{-1}). Si_{13b} has another strong, polarized, peak at 373 cm^{-1} (see the right hand side of Figure 4.6). The high-frequency polarized Raman mode can be described as two independent breathing modes. The atoms in the rhombus on the bottom and the seven upper atoms (see Fig. 4.3l) perform a breathing-mode-like vibration.

A comparison of the spectra for Si_{13b} with the spectra of the proposed ground state structure Si_{13a} in Ref. [41] is helpful in the identification of the ground-state. The IR-spectra of both Si_{13} isomers are very weak and an experimental identification by IR measurements will be difficult. In contrast to the IR spectra, the Raman spectra are strikingly different and should be well suited for an experimental determination of the ground state structure of Si_{13}. Si_{13a} has strong Raman modes at 100, 220, and 337 cm^{-1}, the strongest mode at 337 cm^{-1} being fully polarized. Considering that the Si_{13a} structure is only 0.01 eV/atom more stable than the Si_{13b} structure within DFT-LDA, it would be very useful to determine the experimental Raman-spectra of Si_{13} clusters.

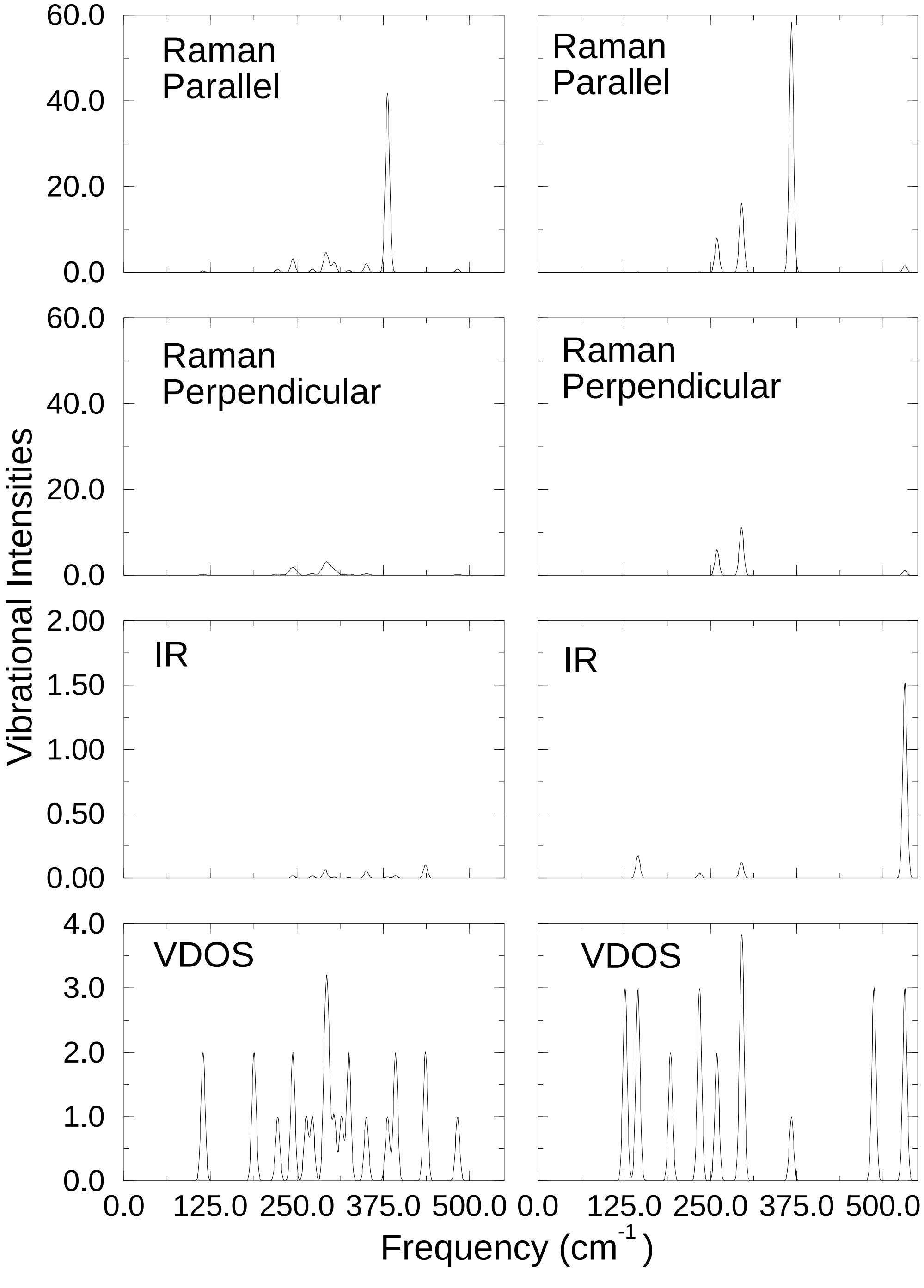

Figure 4.5: VDOS and simulated IR and Raman spectra of the Si$_{10}$(TTP) structure (left) and of the Si$_{10}$(TCO) structure (right). IR intensities are in $(Debye/\,\text{Å})^2/$ amu and Raman activities are in $\text{Å}^4/$ amu. These spectra are taken from Ref.[41].

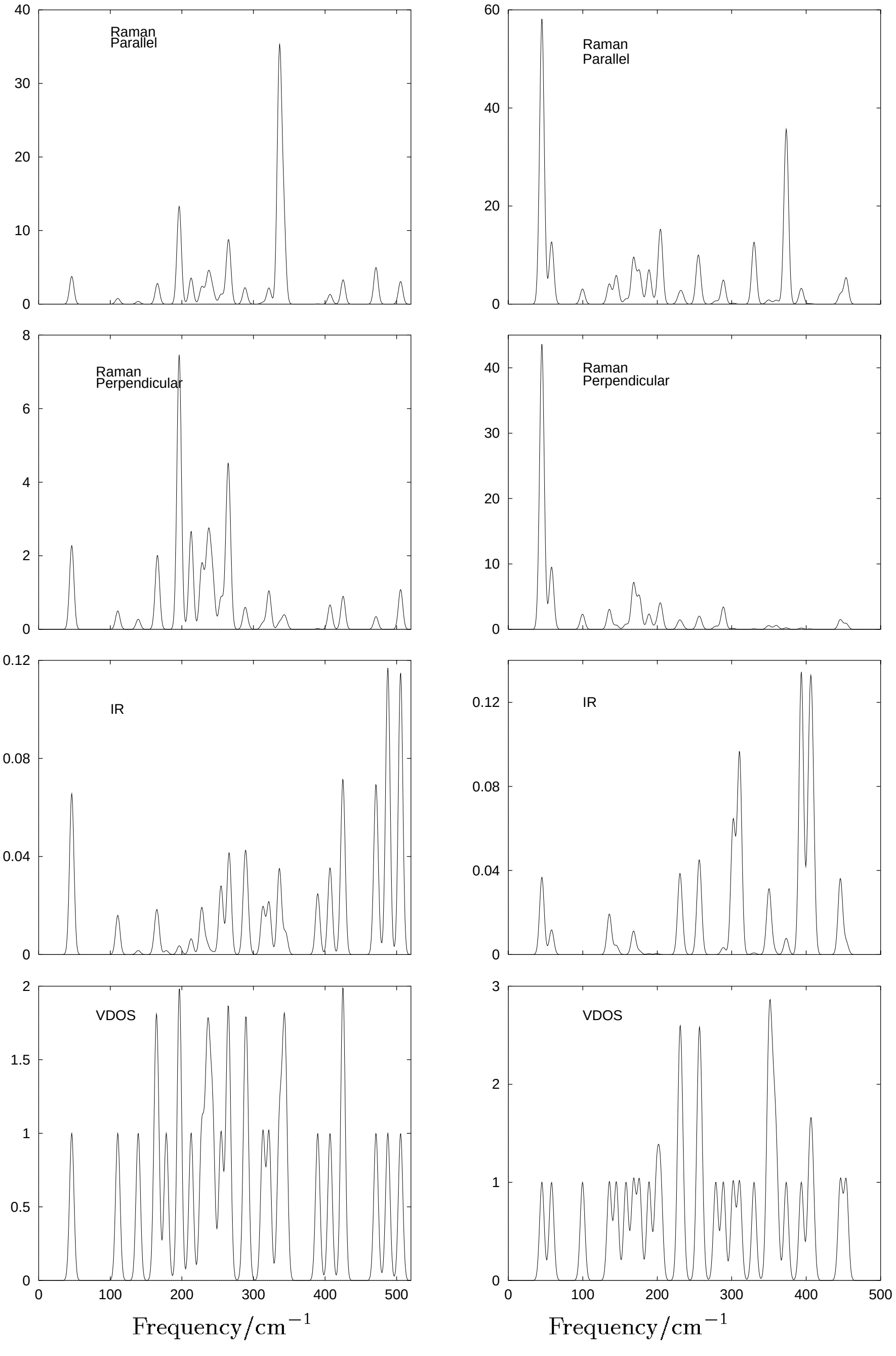

Figure 4.6: VDOS and simulated IR and Raman spectra of the Si_{12a} structure (left) and of the Si_{13b} structure (right). IR intensities are in $(Debye/\,\text{Å})^2/\,\text{amu}$ and Raman activities are in $\text{Å}^4/\,\text{amu}$.

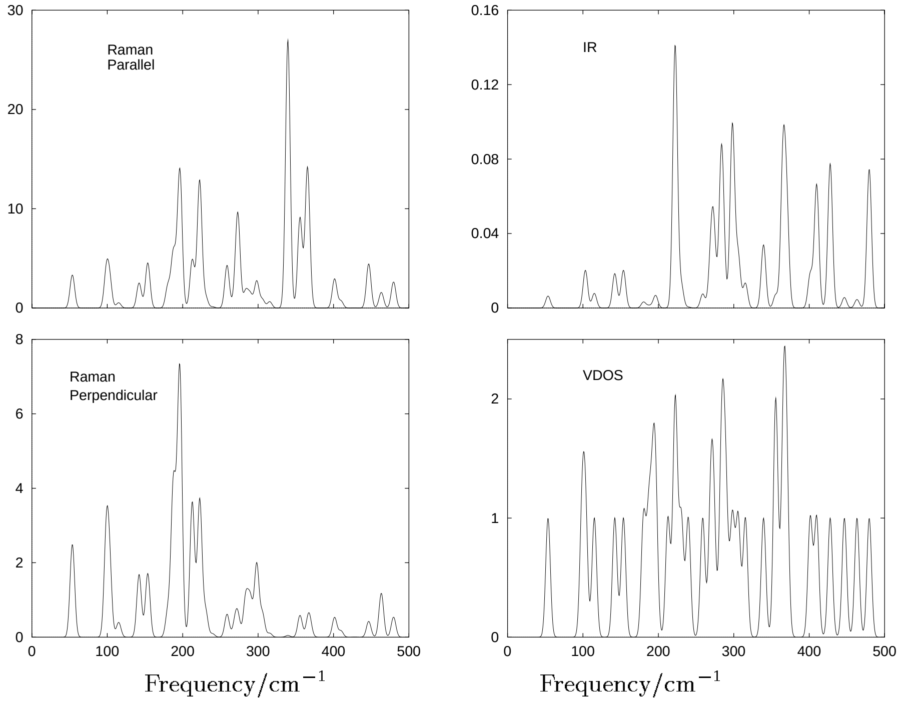

Figure 4.7: VDOS and simulated IR (right) and Raman (left) spectra of the Si_{14a} structure. IR intensities are in $(Debye/\,\text{Å})^2/\,\text{amu}$ and Raman activities are in $\text{Å}^4/\,\text{amu}$.

Si_{14a}: Since the ground-state candidate for Si_{14} has C_s symmetry, all of its 36 vibrational modes are both IR and Raman active. The Raman spectra, which are depicted in Figure 4.7 along with the IR-spectrum, show one highly active mode at 339 cm^{-1}, which is strongly polarized, and five less active peaks located in the range from 196 to 365 cm^{-1}. In contrast to the structures discussed above this strong polarized Raman peak at about 330 to 370 cm^{-1} does not correspond to a breathing mode, but exhibits a more complicated vibration pattern. The most active IR modes have frequencies larger than 200 cm^{-1}. The strongest peak has an intensity of $\approx 0.14\,(D/\,\text{Å})^2/\,\text{amu}$ only, which is close to the experimentally detectable limit. Although structure Si_{14a} is similar to Si_{13b} (the rectangle in Si_{13b} is replaced by a fivefold ring), both the IR intensities and the Raman activities are quite different.

As noted in the previous section the most stable structures of Si_{10} to Si_{14} have a tri-capped trigonal prism as the common subunit. However, there is no strong IR or Raman peak specific to this subunit. The only common (detectable) vibrational feature of Si_{9a}, Si_{10a}, Si_{11a}, Si_{12a}, and Si_{13b} is the strongly polarized Raman peak at about 330 to 370 cm^{-1} corresponding to a breathing mode. The different capping of the common subunit influences the bond-strength and the frequency of these modes. This Raman peak has the highest frequency for Si_{10a} indicating stiff bonds.

Besides IR and Raman spectra the polarizabilities of clusters can be determined by experiment. In Table 4.5 the static electric dipole moments for the investigated clusters are presented and the calculated static polarizabilities are compared to the experimental measurements of Schäfer et al. [69]. The polarizability α is defined as the averaged sum over the eigenvalues α_i of the polarizability tensor: $\alpha = (\alpha_1 + \alpha_2 + \alpha_3)/3$. The calculations of the polarizabilities show smaller variations with cluster size than has been observed in experiment. The measured polarizabilities range from 1.8 to 5.5 Å^3/atom, whereas the calculated polarizabilities are all greater than 4.34 Å/atom and less than 5.21 Å/atom. This deviation between theory and experiment has previously been mentioned in Ref. [41] for Si_{10}, Si_{13}, Si_{20}, and Si_{21}. One could argue that the theoretically determined isomers may not be the ground-state structures seen in experiment. However, due to the small differences in calculated polarizabilities for Si_{13a} (4.40 Å^3/atom) and Si_{13b} (4.51 Å^3/atom) and for both Si_{10} isomers (TTP and TCO) it is unlikely that the consideration of other isomers will resolve the discrepancy between theory and experiment.

Cluster	$\|\mu_{LDA}\|$ Debye	$\|\mu_{LDA}\|$[57] Debye	α_{LDA} Å^3/atom	α_{LDA}[57] Å^3/atom	α_{expt} Å^3/atom
Si_1	0	0	5.88	6.12	5.4
Si_3	0.32	0.33	5.21	5.22	
Si_4	0	0	5.07	5.07	
Si_5	0	0	4.82	4.81	
Si_6	0.21	0.19	4.51	4.46	
Si_7	0	0	4.41	4.37	
Si_{8a}	0	0	4.54	4.52	
Si_{9a}	0.28	0.36	4.43	4.38	2.9
Si_{10a}	0.72	0.69	4.34	4.31	5.5
Si_{11a}	0.76		4.38		2.8
Si_{12a}	0.94		4.50		2.3
Si_{13a}	0.12		4.40		1.8
Si_{13b}	0.30		4.51		1.8
Si_{14a}	1.12		4.47		2.7
Si_{20}	0.02		4.83		3.6
Si_{21}	0.79		4.58		3.1

Table 4.5: Dipole moments and polarizabilities as calculated within DFT-LDA and a finite-difference pseudo-potential method [57]. Experimental polarizabilities for clusters are taken from Ref. [69] and results for Si_1, Si_{10a}, Si_{13a}, Si_{20}, and Si_{21} are taken from Ref. [41]

Chapter 5

Finding low-energy structures with Simulated Annealing

The number of possible geometries for a given set of atoms increases exponentially with the number of atoms. For structures with more than 10 atoms it is not feasible to scan a fine grid in configuration space. Also, there exists no simple unique bonding pattern for silicon clusters and it is not possible to predict the geometries of larger clusters from the geometries of the smaller clusters. Therefore, statistical methods to find the global-energy minimum, or at least a local minimum close to the global minimum, must be applied. The principle idea of *Simulated Annealing* when applied to atomic systems and using molecular dynamics (MD) is to supply the system with additional kinetic energy to overcome barriers around local minima and to find lower lying minima. During the simulation the kinetic energy, or equivalently the temperature, is decreased. This makes it more unlikely to escape from a local minimum towards the end of the simulation.

5.1 Simulated Annealing

Finding the geometry with the lowest energy for a given atomic system can be seen as a special case of a general optimization problem. In a general optimization problem one searches for the global minimum of a cost-function dependent on very many independent variables. It is not feasible to evaluate the cost-function at any point in the (discretized) state-space. Simulated Annealing [70, 71, 72, 73] presents an optimization technique that statistically guarantees finding the global minimum of the cost-function. The technique is based on the simulation of annealing a physical system from a high energy liquid phase to a lowest-energy frozen state. The general method of Simulated Annealing consists of three functional relationships:

1. Selection of points in state-space, in general via a probability density of state-space.
2. Probalbility h for acceptance of a new point determined by the difference ΔE between the cost-functions at the new and at the present point.

3. Schedule of "annealing" the "temperature" T in annealing-time steps t_k.

The probability h to accept a new point with an increase of the cost-function by ΔE compared to the present point is chosen as a Boltzmann distribution:

$$h(\Delta E, T) = e^{-\Delta E/T}.$$

In the case of Boltzmann-type SA it has been proven that it suffices to obtain a global minimum of the cost-function E if T is chosen to decrease not faster than [74]

$$T(t_k) = T_0/\ln(t_k),$$

with T_0 "large enough".

To statistically guarantee finding the global minimum the concept of "ergodicity" is important. The term "ergodic" means that all states of the system are actually to be visited. However, for very large systems ergodicity is not an entirely rigorous concept when faced with the real task of its computation. The long time of execution of standard Boltzmann-type SA has driven the application of a faster temperature schedule violating the conditions required to establish a true ergodic search. The application of a too high cooling rate transforms the SA algorithm into an algorithm better described as Simulated Quenching (SQ). The $1/\ln t$ annealing schedule ensures to find an optimal solution for any arbitrary cost-function possessing quite arbitrary degrees of nonlinearities, discontinuties, stochasticity, and boundary conditions. However, in many cases one knows quite a bit about the cost-function, and perhaps some less stringent necessary conditions may be developed for some special type of cost-functions. The convenience of the SA algorithm, together with the need for some global search over local optima, makes a strong practical case for the use of SQ.

In the case of atomic systems the cost-fuction is identical to the total energy of the system and the state-space is identical to the $3N-6$ dimensional space of internal atomic coordinates. The energy is a continuous function of the coordinates and the possible energy range from compact dense systems to optimal bound configurations can be roughly estimated. For atomic systems the SA/SQ algorithm can be implemented either stochasically or deterministically. In the first case the points in state-space are randomly selected from a given probability-distribution. In the second case of deterministic SA/SQ the points in state-space are determined by molecular dynamics (MD). For a given number of atoms an initial set of coordinates (determining a point in state-phase) and randomly distributed velocities are chosen. The velocities are scaled such that the kinetic energy equals $N_{\mathrm{at}} 3/2\, k_{\mathrm{B}} T$ for a given start temperature $T = T_0$, where $k_{\mathrm{B}} = 8.617 \cdot 10^{-5}\,\mathrm{eV}/K$ is the Boltzmann constant. The next set of coordinates is selected by performing an MD step and propagating the system with respect to the forces on each atom and the present velocities. The forces point in the direction of a lower energy while the nonzero kinetic energy allows to move up-hill and to overcome barriers around local minima.

As one will see in the next Section and the following Chapter, in practice the Simulated Annealing ensures an unbiased global search, if the starting temperature is high enough for a sufficiently long time. The result of the Simulated Annealing depends on the number of start structures, on the cooling-rate and the step width in the molecular dynamics. The choices for these parameters are discussed in the next Section.

Other algorithms competitive with SA or SQ are *Genetic Algorithms* (GA). A Genetic Algorithm is based on the biological evolution process. The cost-function is evaluated for a given set of states (the parents) and the parents with a low cost-function are combined to form offspring. If offspring with a lower cost-function than that of a parent has been created it replaces the parents with the highest cost-function (energy). This process is continued until no offspring with a lower cost-function is created for a certain time. Additionally, "mutations" can be introduced by randomly changing some properties of the population members. In the case of molecules and clusters the offspring is formed by combining fragments of the low-energy parent clusters. Before the energy of the offspring clusters is evaluated the clusters are relaxed to a near minimum via steepest descent or conjugate gradient algorithms. The result of the Genetic Algorithm depends on how large the population is and on how many cycles (generations) are performed. Since GA does not possess any claim to ergodicity, it is important to avoid a restriction to only a subclass of all possible structures. The operations to form new structures must be chosen carefully. E.g., if one starts with spherical structures, cuts the spheres into two parts of equal size and randomly puts the parts together at the cutting-faces, one limits the search to spherical structures. The total number of energy and force calculations in a Genetic Algorithm equals the number of structures in the ensemble times the number of iterations (generations) times the number of steps needed for the relaxation (e.g., the conjugate gradient algorithm). A Genetic Algorithm [37, 65] and a modified single parent Genetic Algorithm [75] have already been applied to search for low-energy silicon clusters.

5.2 Parameters used for Simulated Annealing

The appropriate time step-width for molecular dynamics is related to the shortest time period of the vibrational modes. For silicon clusters the vibrational wavenumbers range from 50 to 600 cm^{-1}. A wavenumber of $1/\lambda = 600\ \mathrm{cm}^{-1}$ corresponds to a time-period of $T_{600} = 5.55 \cdot 10^{-14}\,\mathrm{s} = 2297 \cdot \Delta t_{\mathrm{a}}$, where $\Delta t_{\mathrm{a}} = 2.419 \cdot 10^{-17}\,\mathrm{s}$ denotes the atomic time-unit. Using a step width of $100 \cdot \Delta t_{\mathrm{a}}$ corresponds roughly to $T_{600}/23$. For each temperature 100 MD steps are performed, which corresponds to about $5 \cdot T_{600}$.

The start temperature for the Simulated Annealing should be sufficiently high to overcome high energy-barriers during the initial phase. On the other hand one must avoid dissociation of the structure or apply additional boundary conditions and confine the atoms in a box to ensure that the atoms interact with each other. The start temperature is chosen to lie slightly below the dissociation temperature. For silicon clusters $T_{\mathrm{max}} = 2500\,\mathrm{K}$ results in a high variation of the geometry during the MD, but the clusters do not dissociate. To scan a large area in configuration space the temperature should be high for a relatively large time. Instead of a linear

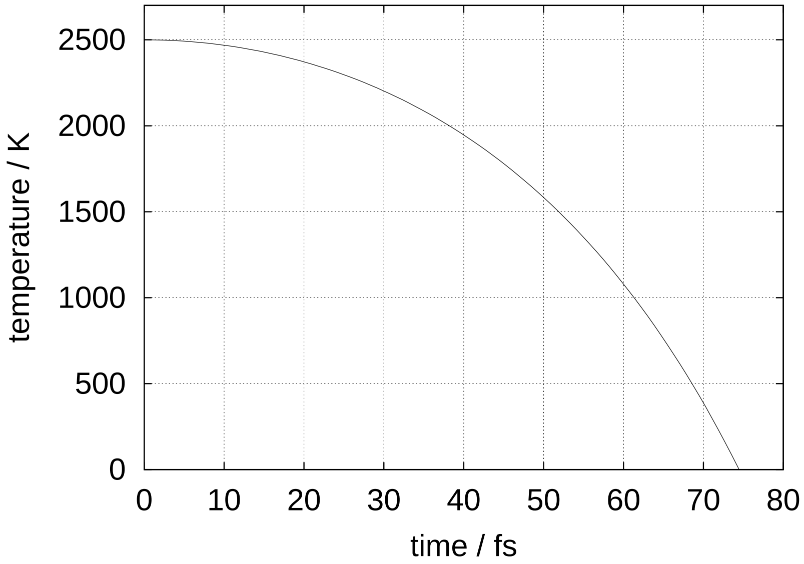

Figure 5.1: Temperature as a function of time during Simulated Annealing.

temperature decrease, a temperature-time dependency of the form:

$$T(t) = T_{\mathrm{max}}[2 - e^{at^2}]$$

is chosen. The parameters $T_{\mathrm{max}} = 2500\,\mathrm{K}$ and $a = 1.25 \cdot 10^{-4}/\mathrm{fs}^2$ result in a temperature-time dependency as shown in Fig. 5.1. The temperature is above 1500 K for two-thirds of the total time. This annealing schedule is much faster than the $1/\ln t$ annealing schedule required to ensure finding the global minimum of arbitrary cost-functions. However, for many tests on smaller silicon clusters this fast annealing schedule suffices to find the global energy minimum (see below). The total time interval is divided into 300 subintervals. In each subinterval 100 MD steps with a step width of 100 Δt_{a} are performed at constant temperature. The total interval corresponds to $73 \cdot 10^{-12}\,\mathrm{s}$ and 30 000 energy and force calculations are performed.

To find low-energy structures for a given cluster size, the Simulated Annealing is applied to several (randomly) created seed clusters. After the Simulated Annealing run the structures are fully relaxed with the conjugate gradient method until the maximum force on the nuclei drops below $10^{-4}\,\mathrm{H}/\,a_{\mathrm{B}}$.

It is difficult to compare the efficiency of Simulated Annealing to that of a Genetic Algorithm, because, besides the statistical nature of both algorithms, the number of calculations necessary for a conjugate gradient relaxation depends on the cluster size and the given potential around the local minimum. For a Si_{35} cluster the relaxation to a maximum force of $10^{-3}\,\mathrm{H}/\,a_{\mathrm{B}}$ requires about 30 to 80 conjugate gradient steps dependent on the initial step-width. Assuming an average of 50 steps, it follows that with the 30000 energy and force calculations performed in the Simulated Annealing one could evaluate 600 structures with an Genetic Algorithm, e.g., 30 generations of an ensemble of 20 structures. As outlined in the next paragraph, the SA parameters chosen yield the global minimum of Si_7 for almost any reasonable initial structure

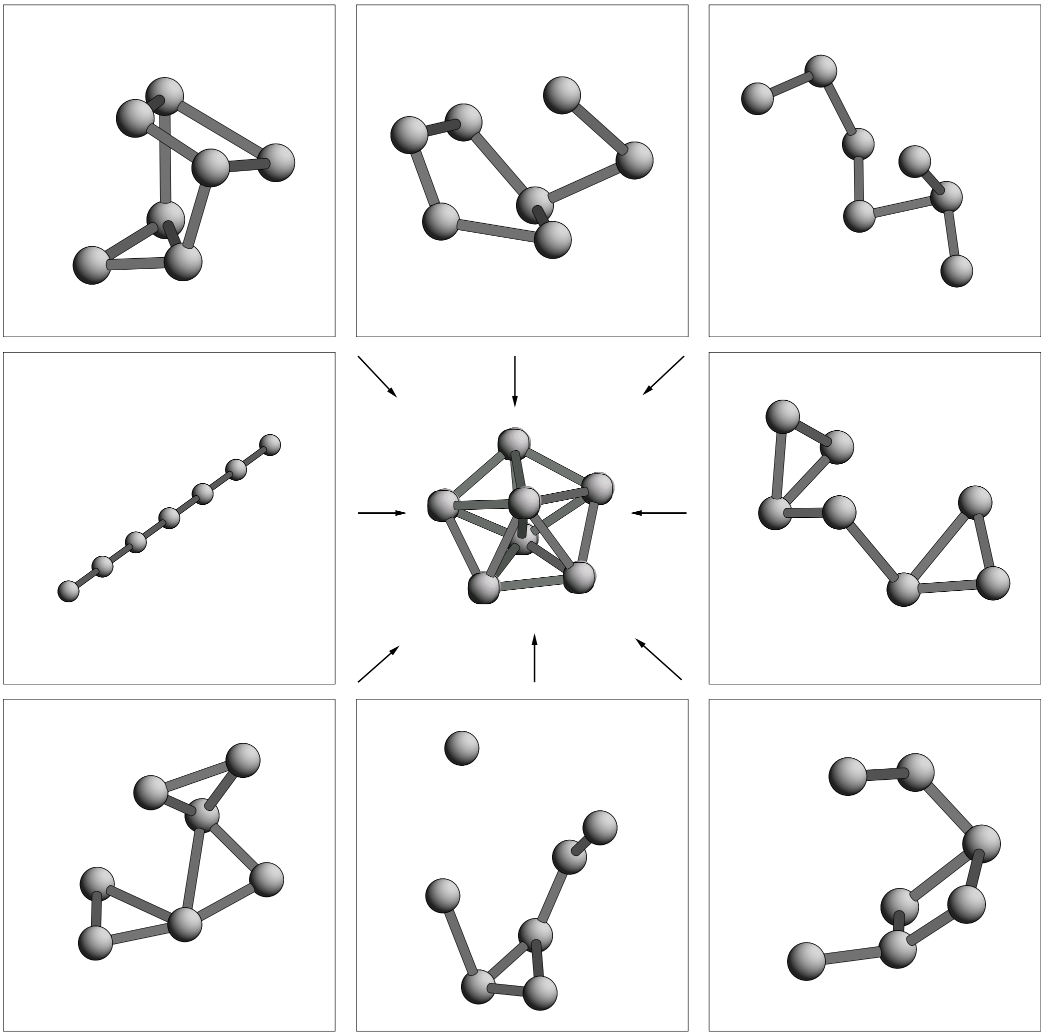

Figure 5.2: All initial configurations (framed boxes) of 7 silicon atoms result in the global minimum geometry $\mathrm{Si}_7(D_{5h})$ depicted in the center after Simulated Annealing.

and probably a higher cooling rate with fewer temperature steps would give the same result[1]. However, the complexity of the energy-surface in configuration space dramatically increases with the cluster size and for larger clusters the high number of MD steps is required to yield clusters with a low energy.

For smaller silicon clusters the Simulated Annealing of different random structures with the parameters given above results in the global minimum (the lowest-energy structure known so far) in most cases. For Si_7 this is illustrated in Figure 5.2. All eight initial configurations including seven configurations with randomly distributed atoms in a finite sphere and one linear chain configuration result after Simulated Annealing in the global minimum geometry with D_{5h}-symmetry. For Si_7 there exist several local minima. Raghavachari et al.report on five low-energy isomers of Si_7, three of them are proven to represent local minima by calculating the harmonic

---

[1] For a few cases this has been verified

vibrational frequencies [32]. In none of the performed runs the SA algorithm is trapped into these local minima, and one can expect to find structures with an energy close to the one of the global minimum also for larger clusters.

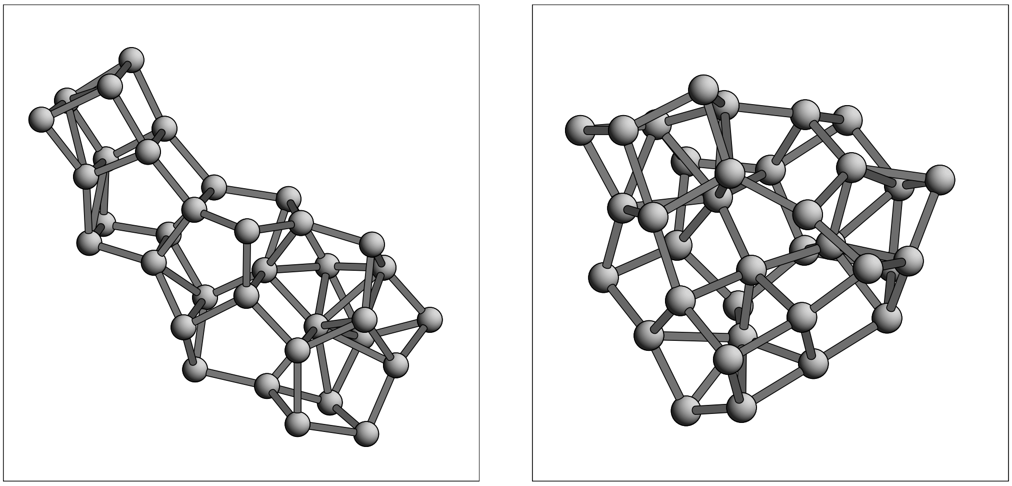

(a) $E = -3.98\,\mathrm{eV/atom}$, $p = 0.50$ (b) $E = -4.00\,\mathrm{eV/atom}$, $p = -0.04$

Figure 5.3: (a) Cluster after Simulated Annealing with high angular momentum, (b) cluster after Simulated Annealing with zero angular momentum. p is a measure for the prolateness of the structure defined via the moments of inertia. For spherical clusters it is $p = 0$.

To find structures as they are present in low-temperature experiments, it is important to avoid a high total angular momentum of the cluster during the Simulated Annealing. To calculate new atomic positions from the old positions, the velocities and the forces, a three-step *Verlet* algorithm is used in the MD implementation of DFTB and the first set of coordinates is created randomly. In general this introduces a nonzero total momentum and a nonzero total angular momentum. A high angular momentum introduces large additional centrifugal forces which results in a bias towards prolate structures for the annealed clusters. Figure 5.3 shows the final structures after two different Simulated Annealing runs. The same structure, an almost spherical cluster with 35 randomly distributed silicon atoms, was annealed with a high angular momentum (about $10^{-12}\,\mathrm{kg\,m^2}/s$ on average) in one case and with zero angular momentum in the other case. The angular momentum was set to zero by using an appropriate velocity distribution. The high angular momentum distorts the cluster into a clearly prolate structure.

Chapter 6

Shape transition at cluster sizes of 20 to 30 atoms

Raman and infrared experiments on silicon clusters have not yet been able to provide ground-state vibrational frequencies for clusters with more than seven atoms. This is due to the difficulty of producing sufficient numbers of larger clusters, which are necessary to obtain an observable signal. On the other hand, ion mobility measurements have been proven to provide useful information about the structures of silicon clusters containing over a dozen atoms. While vibrational spectra give detailed information about the different bonds present in a given cluster, the mobility depends mainly on the rotational-averaged collision cross-section corresponding to the shape of the cluster. The mobility experiments indicate a shape transition in the size range from 24 to 34 atoms. This Chapter briefly describes the mobility experiments and gives a detailed description of the calculated energies and geometries of stable clusters obtained from the Simulated Annealing of 100 isomers of Si_{25}, Si_{29}, and Si_{35}. The structures of the most stable clusters are analyzed and compared to the measured mobilities to gain an understanding of what causes the transition.

6.1 Experimental indications of a shape transition from Si_{20} to Si_{30}

In the mobility experiments done by Jarrold et al. [76, 77] ionized silicon clusters were mass-selected, accelerated into a buffer gas by an electric-field, and the drift-time in the buffer gas was measured. To obtain results independent of the buffer gas different kinds of gas were used. First, the experiments were performed with positive ions at room temperature. Later the mobility experiments additionally were performed at 78 K [65]. Recently the ion mobility measurements have been repeated with a higher resolution for silicon cluster anions and cations [78].

The drift-time, is proportional to the inverse mobility and, considering only elastic collisions, to the rotational-averaged cross section of the cluster. Prolate structures have a longer drift-time than spherical structures of the same cluster size. For a fixed shape the drift-time increases with increasing cluster size.

Plots of the measured inverse reduced mobilities versus the cluster size are shown in Figure 6.1 for the cations (top) and the anions (bottom). This Figure clearly reveals the existence of two distinct growth-paths and the switch from one path to the other at about Si_{24} to Si_{30}.

For the cations one observes a shift from a low mobility component to a high mobility component between Si_{24}^+ and Si_{28}^+. This indicates a transition from prolate to more spherical geometries. For the anions a similar structural transformation occurs at slightly larger cluster sizes between Si_{26}^- and Si_{30}^-. The transition does not appear to be a sharp transformation from a prolate shape to a more spherical shape, for many cluster sizes more than two isomers are clearly resolved. For the cations several isomers are detected mainly between Si_{24}^+ and Si_{28}^+. It should be noted that this is true for, e.g., Si_{17}^+ or Si_{41}^+, too. For the anions this occurs for the cluster sizes between Si_{24}^- and Si_{30}^- as well as for, e.g., Si_{33}^- or Si_{43}^-. The low mobility component survives with a detectable abundance up to around Si_{30}^+ for cations and up to around Si_{38}^- for anions. The existence of several isomers in this size regime is also indicated by previous chemical reactivity experiments [79, 80, 81] and simultaneous mobility and chemical reactivity measurements [76].

The measured mobilities show that the charge state affects the relative stability of the isomers even for quite large clusters. The transition between prolate and more spherical geometries occurs at smaller cluster sizes for cations than it does for anions. The prolate geometries persist for larger cluster sizes for anions than for cations. Apparently, the two extra electrons in the anions stabilize the prolate isomers relative to the more spherical ones. Structural changes caused by charging neutral silicon clusters have previously been examined in other theoretical studies [60, 82]. The geometries for the cations Si_n^+ with $n \leq 7$ [83, 84] and with $n \leq 20$ [60] have been theoretically determined. Except for $n = 6, 8, 12,$ and 13 the ground-state structures remain identical to those of the neutrals. Removing an electron from a neutral cluster does not influence the stability significantly. On the other hand, the lowest unoccupied molecular orbital (LUMO) of a neutral cluster most likely corresponds to a non-bonding state. After adding an electron to a neutral cluster, the cluster will rearrange its geometry in order to lower the energy.

The drift-time measurements indicate that the low mobility (long drift-time) clusters all have a similar shape and undergo a special growth pattern and that the high mobility clusters all have a shape different from the low mobility clusters and undergo a different growth path. The authors in [76] suggest a prolate growth sequence for the component with the smaller mobility. Starting with Si_{10}^+, which is assumed to be almost spherical in agreement with predictions from theory, the clusters grow as prolate spheroids with almost constant diameter and increasing length. Assuming that the prolate spheroids can be represented by a cylinder with diameter d and length l the measured mobilities indicate an increasing aspect ratio (defined as l/d) which reaches about 3 by Si_{30}^+. For the component with the larger mobility, observed for $n \geq 24$, they suggest an oblate growth sequence with almost constant l and increasing d. However, this assignment is not unique. The authors mention that the low mobility component could, in principle, also be fit by a model where the clusters follow an oblate growth sequence and get flatter (l gets smaller) with increasing cluster size.

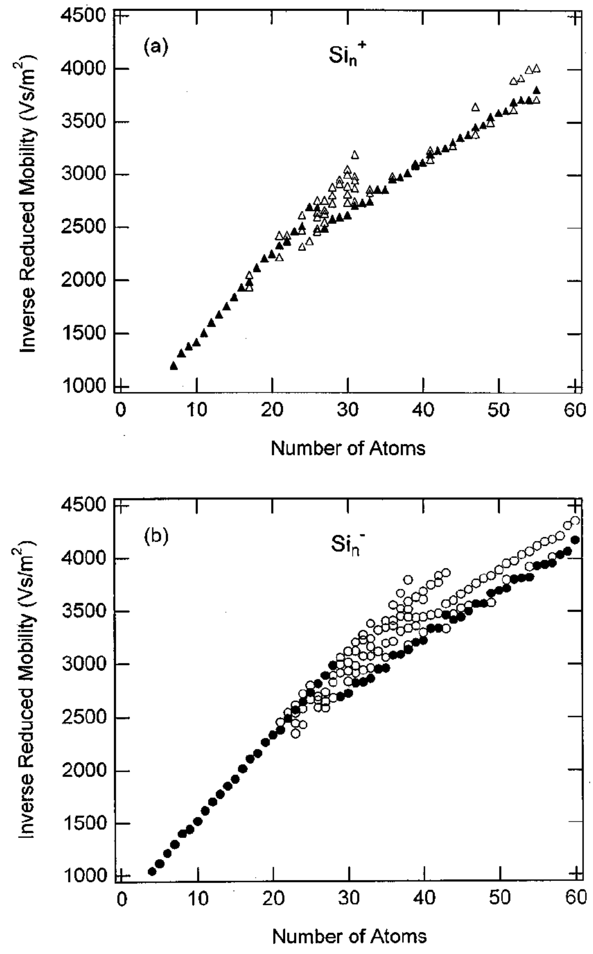

Figure 6.1: Plot of inverse reduced mobilities versus number of atoms for silicon cluster cations (top) and anions (bottom). The filled points correspond to the most abundant peak observed for each cluster size while additional isomers are shown as open points. This Figure is taken from Ref. [78].

6.2 Stability of differently shaped clusters

A systematic theoretical search for low-energy structures has been undertaken only for smaller silicon clusters to date, because the number of possible configurations increases exponentially with the number of atoms in the cluster. Recently, Ho et. al searched for low-energy clusters with 12 to 20 silicon atoms using a Tight-Binding approach and a Genetic Algorithm [65]. They compared the mobilities obtained by trajectory calculations of their low-energy structures with the measured values and found good agreement with the lower-mobility component from experiment for clusters with up to 18 atoms. However, the mobilities for their lowest-energy structures of Si_{19} and Si_{20} match the higher-mobility component from experiment better. In agreement with the assumptions about the relationship between drift-time and shape mentioned above their low-energy clusters with less than 19 atoms have prolate shapes and the low-energy clusters for Si_{19} and Si_{20}, which match better the short drift-time component, are more spherical. These calculations predict the transition from prolate to oblate or spherical clusters to occur for smaller cluster sizes than found experimentally, where the transition starts for cluster sizes greater than 23 atoms. The authors state this could be due to an entropic effect similar to that found for carbon clusters. For carbon the fullerene is predicted to be the most stable geometry for a cluster as small as C_{20}^+. The smallest fullerene observed experimentally is C_{30}^+ though. This occurs since at the high temperature required to induce isomerization, the fullerene is not a low-*free-energy* structure for the smaller clusters [85, 86]. However, the energy differences between the spherical and prolate isomers of Si_{19} and Si_{20}, reported in [65], are only about 0.02 eV/atom. Recently some prolate isomers with even lower energies have been reported [75].

To investigate the structural transition for larger clusters extensive Simulated Annealing optimizations with DFTB were performed for silicon clusters with 25, 29 and 35 atoms. To allow for an unbiased search 200 to 300 (900 for Si_{35}) initial structures with very different geometries were created for each cluster size. Prolate structures were formed by stacking triangles, rhombi, and pentagons in different combinations. Spherical structures were obtained by randomly filling a sphere under the constraint not to fall below a minimum bond-length and to result in an atomic-density similar to that of the diamond or simple cubic phase. Moreover, fragments of the silicon diamond phase were included in the group of initial clusters. First, all structures were relaxed with the conjugate gradient method to nearby local minima. For each cluster size the one hundred structures with the lowest energy were chosen for the time-consuming Simulated Annealing. Since the Simulated Annealing started with a high temperature of 2500 K, where the atoms almost dissociate, the geometry of the clusters varied in a wide range at the beginning of the simulation. Even if one starts with a linear chain of atoms the final structure is compact, which shows that during the Simulated Annealing geometries much different from the initial geometry can occur and the search is not restricted to the configuration space close to the initial geometry. During the simulation the rotation of the clusters was prohibited to avoid the preferred generation of prolate structures (see Chapter 5). After decreasing the temperature to 300 K the clusters were further relaxed with the conjugate gradient method to minimize the forces on the atoms.

Already for the smaller silicon clusters one notices that the number of low-energy structures increases with cluster size. There exist several local minima on the energy hyper-surface with energies close to the energy of the global minimum and the energy-differences between some of these local minima are smaller than 0.01 eV/atom and challenge the accuracy of DFTB as well as of self-consistent-field density-functional or Hartree-Fock based methods. This is particularly true for clusters with more than 20 atoms considered here. Within DFTB the cohesive energies of the ten most stable clusters range from -3.99 eV/atom to -3.97 eV/atom for Si_{25}, from -4.00 eV/atom to -3.99 eV/atom for Si_{29}, and from -4.04 eV/atom to -4.02 eV/atom for Si_{35}. Note that the energy per atom is given, the corresponding differences for the whole cluster are about 0.5 eV. The energy differences between the lowest-energy and the highest-energy isomer of the 100 annealed isomers are 0.08 eV/atom (2.1 eV), 0.08 eV/atom (2.4 eV), and 0.08 eV/atom (2.7 eV) for Si_{25}, Si_{29} and Si_{35}, respectively. Because of the very small differences in energy, the exact energetic order of some isomers might be slightly different within other methodologies. E.g., the DFTB-energies for the ten most stable Si_{25} isomers are compared to the energies obtained within all-electron scf-GGA (*NRLMOL*) using the Perdew-Burke-Ernzerhof exchange-correlation functional in Table 6.1.

cluster	E_{coh} (DFTB) eV/atom	E_{coh} (scf-GGA) eV/atom	p (DFTB)	p (scf-GGA)
Si_{25}(a)	-3.99	-3.89	0.23	0.20
Si_{25}(b)	-3.98	-3.88	0.28	0.25
Si_{25}(c)	-3.98	-3.92	0.63	0.61
Si_{25}(d)	-3.97	-3.88	0.15	0.14
Si_{25}(e)	-3.97	-3.90	0.64	0.63
Si_{25}(f)	-3.97	-3.88	0.29	0.28
Si_{25}(g)	-3.97	-3.89	0.19	0.17
Si_{25}(h)	-3.97	-3.88	0.49	0.48
Si_{25}(i)	-3.97	-3.90	0.45	0.44

Table 6.1: Cohesive energies and prolateness p for the, within DFTB, nine most stable isomers of Si_{25} within DFTB and scf-DFT-GGA.

For all silicon clusters the DFTB energies reported in this Chapter have been calculated with the DFTB parametrization as described in the Appendix. With this parametrization the diamond structure of silicon has a cohesive energy of -4.80 eV/atom. The DFTB energies reported in the previous Chapters for silicon clusters up to Si_{14} have been calculated with an older DFTB parametrization adjusted to scf-DFT-LDA. Therefore, the older parametrization showed an overbinding typical for LDA. Compared to the new parametrization described in the Appendix the older DFTB energies per atom are shifted by about -0.45 eV. For both parametrizations the cohesive energies for the ground-state clusters of Si_2 to Si_8 are given in the Appendix. The self-consistent-charge (SCC) extension has been used throughout this Chapter to accurately treat the charge transfer between silicon atoms with different coordination numbers. However, it turned out that for the homo-nuclear silicon systems the energies with and without the SCC extension are identical within 0.01 eV/atom (see the Appendix).

The inverse reduced mobilities are proportional to the collision cross section and depend on the shape of the cluster. Instead of explicitly calculating the collision cross section it is more convenient to define a scalar variable, which describes the shape of a cluster via the moments of inertia. For a spherical structure all moments of inertia are equal, a prolate structure has two large and one small moments of inertia and an oblate structure has two small and one large moments of inertia. The prolateness p defined by the moments of inertia I_j as

$$p := \sum_{j=1}^{3}(I_j - \bar{I}) = -\frac{I_1}{2} + I_2 - \frac{I_3}{2}, \; 0 < I_1 \leq I_2 \leq I_3, \; \bar{I} := \frac{I_1 + I_3}{2} \tag{6.1}$$

has the following values dependent on the shape of the structures:

$$p \begin{cases} < 0 & : \quad I_1 = I_2 < I_3 \quad : \quad \text{oblate} \\ = 0 & : \quad I_1 = I_2 = I_3 \quad : \quad \text{spherical} \\ > 0 & : \quad I_1 < I_2 = I_3 \quad : \quad \text{prolate} \end{cases}$$

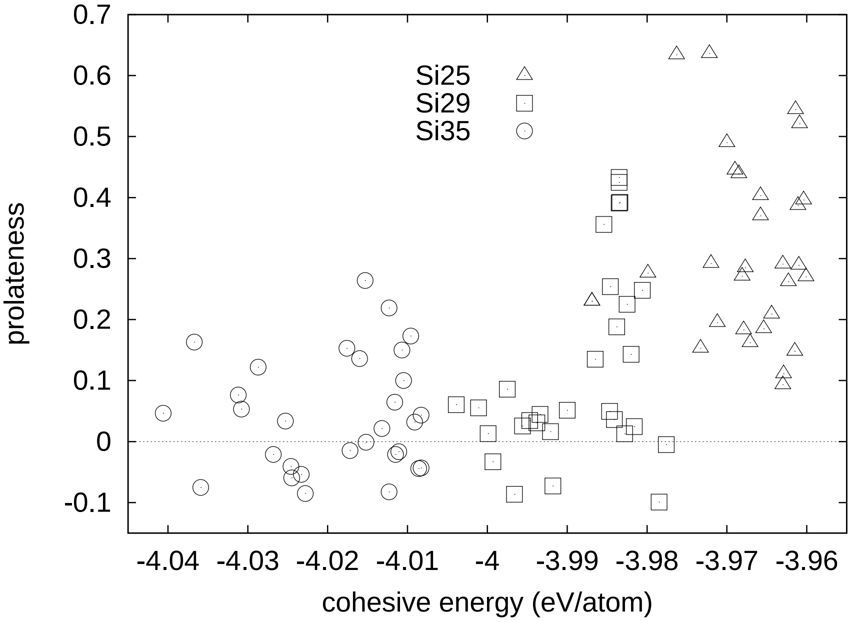

Figure 6.2: Prolateness defined via moments of inertia vs. cohesive energy for the 30 most stable isomers of Si_{25}, Si_{29}, and Si_{35}.

The prolateness plotted versus the cohesive energy is displayed in Figure 6.2 for the 30 most stable isomers of Si_{25}, Si_{29} and Si_{35}. This figure shows that the 30 most stable isomers of Si_{25} exhibit prolate shapes as well as more spherical shapes. The shape distribution is not much different for the ten most stable (ten most left triangles in Fig. 6.2) compared to the 30 most stable isomers. The shape distribution is similar for the most stable isomers of Si_{29} but shifted to more spherical structures, and all of the 10 (within DFTB) most stable isomers are spherical ($-0.1 \leq p \leq 0.1$). All of the 30 most stable isomers of Si_{35} exhibit a prolateness below 0.3 and above -0.1.

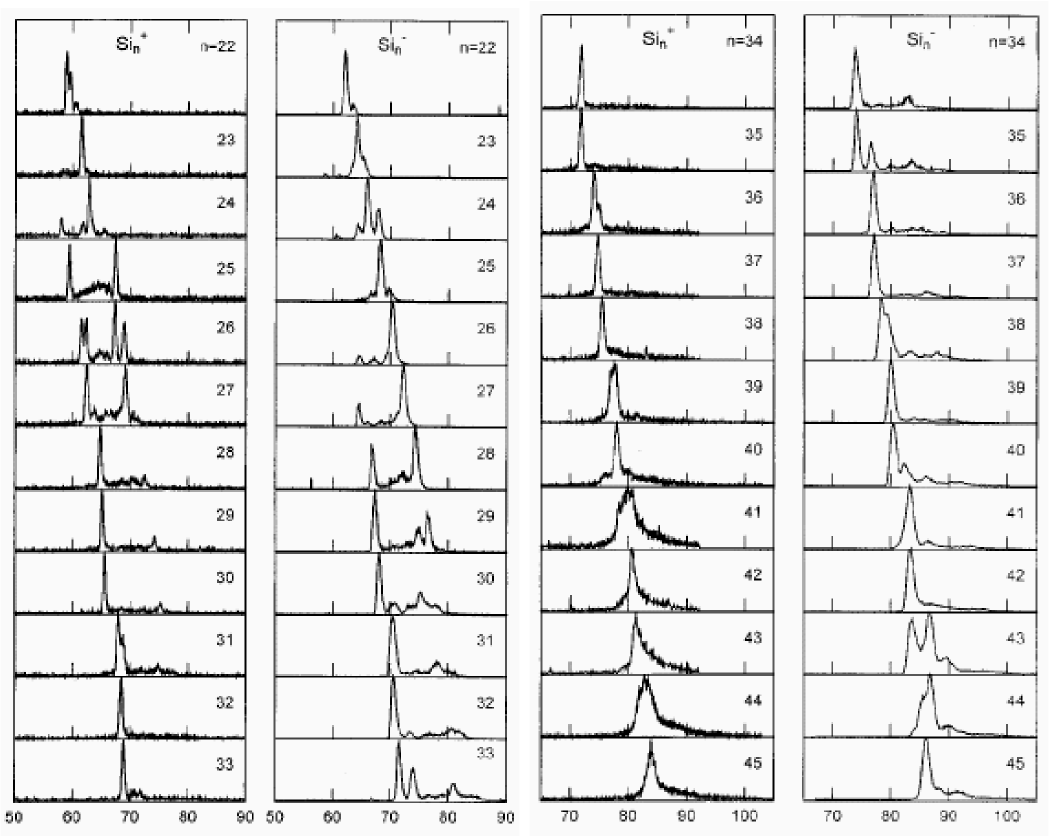

Si_n^+ Si_n^-

(a)

Si_n^+ Si_n^-

(b)

Figure 6.3: Measured drift-time distribution of cations Si_n^+ (left) and anions Si_n^- (right) [78]. (a) Si_{22} to Si_{33}, (b) Si_{34} to Si_{45}. The drift times in (a) range from 50 to 90 ms and in (b) from 70 to 100 ms.

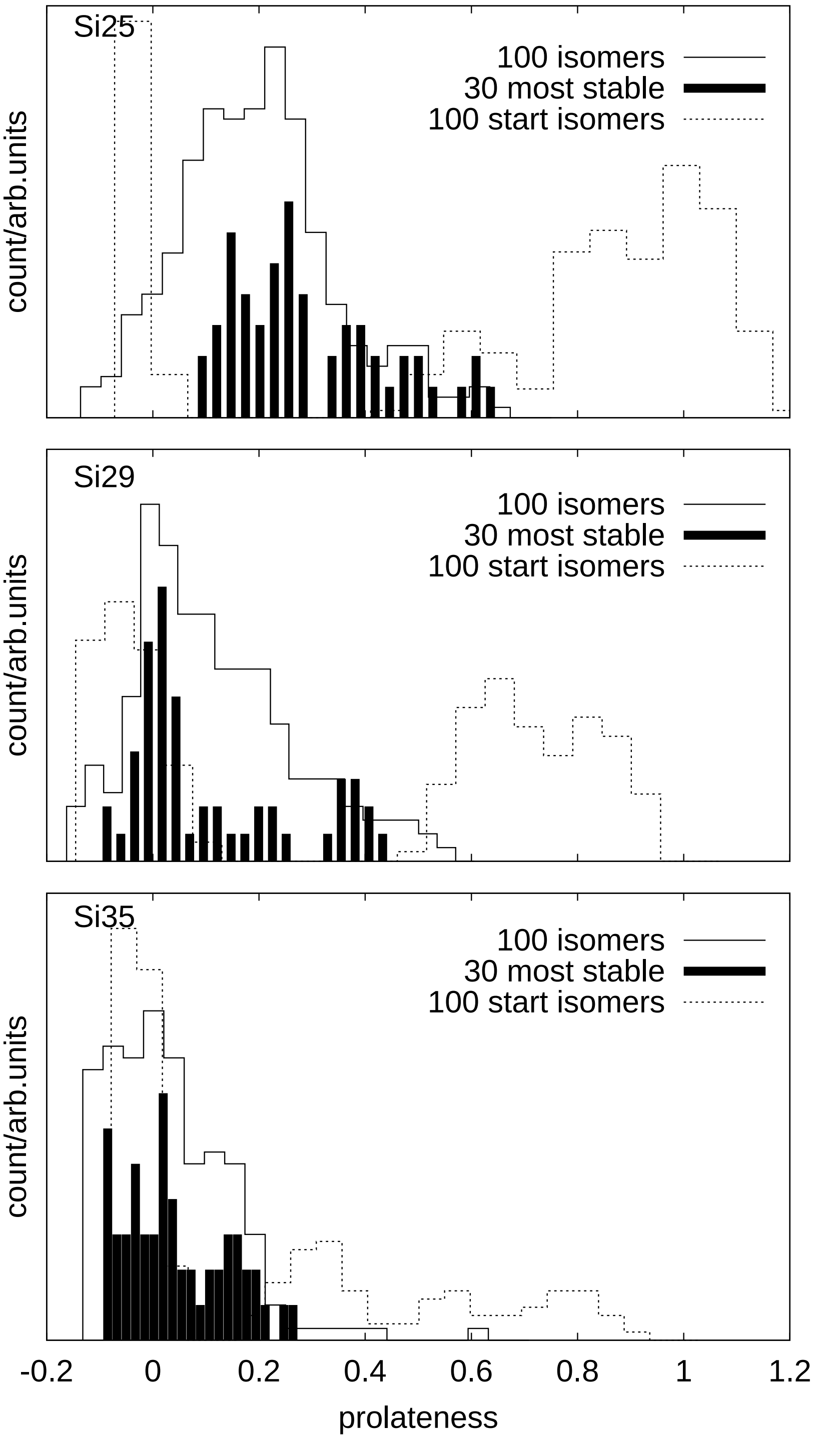

Figure 6.4: Distribution of shapes for all 100 isomers before (dotted line) and after (solid line) the Simulated Annealing and for the 30 most stable isomers (bars) of Si_{25}, Si_{29}, and Si_{35}. A prolateness of 0.0 corresponds to spherical shapes and a prolateness $\gg$ 0.0 to prolate shapes.

The distribution of shapes (defined via the prolateness) is displayed in Figure 6.4 for all 100 isomers before and after the Simulated Annealing and, additionally, for the 30 most stable isomers of Si_{25}, Si_{29}, and Si_{35}. This figure clearly shows the change in shape, when the cluster size increases from Si_{25} to Si_{35}. The prolateness of the 30 most stable isomers of Si_{25} ranges from 0.09 (spherical) to 0.64 (prolate). This range equals $[-0.10 : 0.43]$ for the 30 most stable isomers of Si_{29} and is reduced to $[-0.09 : 0.26]$ for the 30 most stable isomers of Si_{35}. Considering all hundred isomers treated with Simulated Annealing the range of the prolateness is slightly larger: $[-0.12 : 0.65]$ (Si_{25}), $[-0.15 : 0.55]$ (Si_{29}) and $[-0.11 : 0.44]$ (Si_{35}). For Si_{25} spherical structures disappear among the 30 most stable isomers compared to all 100 Si_{25} clusters. Clearly it can be seen that the result of the Simulated Annealing is not biased by the initial shape distribution. Most of the start structures for Si_{25} had a prolateness larger than 0.8 while none of the structures after the Simulated Annealing has such a high prolateness. Similarly, 36 out of the 100 initial structures for Si_{35} had a prolateness larger than 0.3, while only three out of all 100 structures, and none of the 30 most stable isomers has a prolateness larger than 0.3 after the Simulated Annealing.

A link to experimental data can be provided by comparing the distribution of shapes (see Fig. 6.4) obtained within DFTB to the measured drift time distributions (DTDs) displayed in Figure 6.3. It is important to notice that the DFTB calculations were performed on the neutral clusters, while the measurements were performed on the anions and cations. In the DTD's the measured intensity is plotted versus the drift time in the buffer gas. Since the averaged rotational cross section is larger for a prolate structure compared to a spherical structure of the same size, the drift time increases with increasing prolateness. Therefore, the distribution of clusters as a function of prolateness is directly related to the distribution as a function of drift time.

The calculated shape distribution of the 30 most stable Si_{25} isomers (top of Fig. 6.4) features a large group of clusters with a prolateness p between 0.1 and 0.3, the remaining stable isomers all have a prolateness larger than 0.35. The measured DTD of Si_{25}^+ (upper left in Fig. 6.3) shows two dominant peaks, one short and one long drift-time component, and in between additional isomers with a smaller abundance. The DTD of Si_{25}^- features one dominant peak at a long drift-time and additionally some other weak components very close to the dominant peak. The MD simulation and scf DFT calculations show that there exist both, prolate and spherical low-energy isomers of Si_{25}. The mobility measurements indicate that for Si_{25}^+ one prolate cation (or few isomers with about the same shape) and one more spherical cation are especially stable. For the anion Si_{25}^- the measurements indicate a prolate isomer to be much more stable than the more spherical ones. The existence of both prolate and spherical low-energy isomers of neutral Si_{25} is also found by very accurate DFT-GGA calculations [87]. The reported energy difference between a compact spherical structure similar to Fig. 6.5 (a) and a prolate structure similar to Fig. 6.5 (b) is only 0.15 eV in favour of the compact spherical isomer. Despite the fact that there exist some prolate and spherical isomers of Si_{25} with a very low energy it may be more likely for the prolate structures to form. The prolate structures can easily be built from smaller stable isomers as Si_6 and Si_{10}, whereas the compact structures have to be formed by successively adding single silicon atoms or by complex rearrangements. This could explain the absence of the short drift-time component in the DTD for Si_{25}^{-}.

The calculated shape distribution for the 30 most stable isomers of Si_{29} shows that most of the isomers exhibit a spherical shape ($p \approx 0$). The remaining low-energy isomers are either slightly prolate ($0.1 < p < 0.3$) or prolate ($p \approx 0.4$). This theoretical result matches the measured DTDs for the cations and anions of Si_{29}. In the experiment the abundance of prolate geometries is larger for Si_{29}^{-} than for Si_{29}^{+}. For both charge states the short drift-time component, i.e., the more spherical geometry, is dominant. For Si_{35} the DFTB calculations find solely nearly spherical or slightly prolate structures ($p < 0.3$) with a low energy. This is in agreement with the measured DTDs of Si_{35}^{+} and Si_{35}^{-}. The DTD for Si_{35}^{+} exhibits one dominant short drift-time component, only. The DTD for Si_{35}^{-} exhibits two peaks at short drift-times and a very weak intensity at longer drift-times.

The structural variety of the most stable isomers of Si_{25}, Si_{29}, and Si_{35} is illustrated in Fig. 6.5. Here, the most oblate (smallest p) and most prolate (largest p) isomers are shown for each cluster size. The almost spherical clusters feature two or three highly coordinated atoms inside the cluster and three- or fourfold coordinated atoms on the surface. Many of the prolate isomers of Si_{25} can be described as two smaller clusters (with about 10 atoms each) connected by an intermediate ringlike fragment. The prolate Si_{25} cluster, displayed in the upper right of Fig. 6.5, provides one example. A Si_9 cluster is connected via a sixfold ring to a Si_{10} cluster. The Si_9 fragment does not have the same geometry as the most stable Si_9 cluster. It more resembles the tricapped trigonal prism isomer of Si_9, which has an energy close to the ground-state of Si_9 (see Chapter 4 and [20]). Interestingly, all of the three most stable isomers within scf-DFT-GGA (see Tab. 6.1) match this bonding pattern, i.e., a formation of $Si_9 + Si_6 + Si_{10}$. Also, three of the 30 most stable isomers of Si_{29} obey this pattern, but none of the 100 Si_{35} isomers. The slightly prolate isomers (with $p \approx 0.3$) of Si_{35} are rather compact.

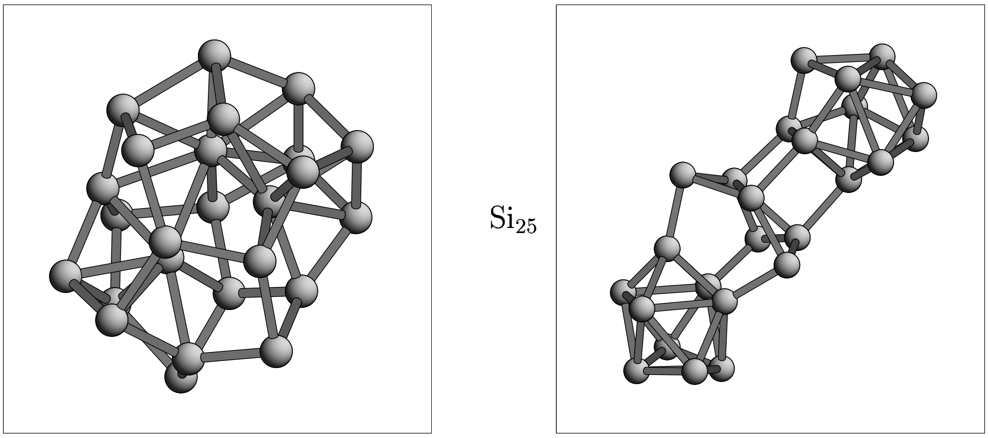

(a) $E = -3.96\,\mathrm{eV/atom}$, $p = 0.09$ (b) $E = -3.97\,\mathrm{eV/atom}$, $p = 0.64$

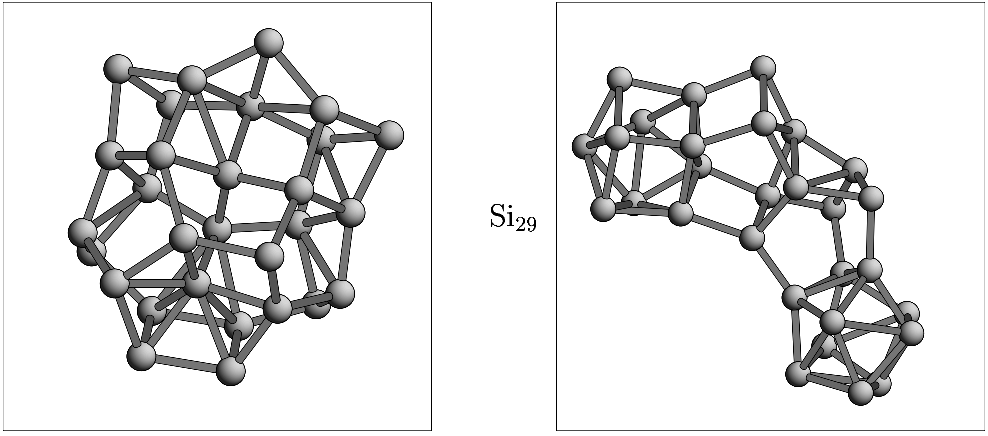

(a) $E = -3.98\,\mathrm{eV/atom}$, $p = -0.10$ (b) $E = -3.98\,\mathrm{eV/atom}$, $p = 0.43$

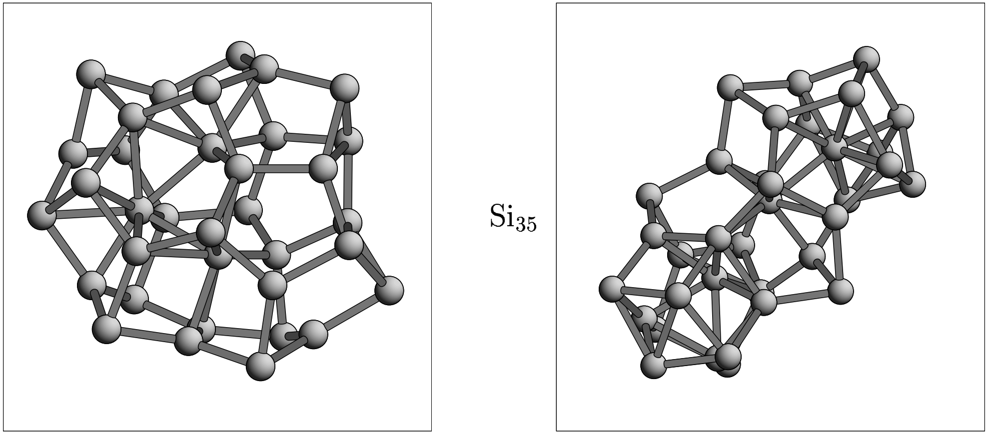

(a) $E = -4.02\,\mathrm{eV/atom}$, $p = -0.09$ (b) $E = -4.02\,\mathrm{eV/atom}$, $p = 0.26$

Figure 6.5: Most oblate structure (a) and most prolate structure (b) from the 30 most stable isomers of Si_{25}, Si_{29}, and Si_{35}.

The results of the MD search with DFTB show that there exist many low-energy isomers with almost equal energies for Si_{25}, Si_{29}, and Si_{35}. The dominant shapes for each cluster size undergo a transition with increasing cluster size. For Si_{25} both spherical and prolate shapes occur. For Si_{29} and Si_{35} mainly spherical shapes are found for the 30 most stable isomers. The calculations indicate that the peaks found in the measured DTDs may not be due to only one special isomer, but to several isomers with a very similar shape and mobility. E.g., within DFTB there are 11 isomers of Si_{29} with a prolateness between -0.05 and +0.05 and cohesive energies between $-4.00\,\mathrm{eV/atom}$ and $-3.98\,\mathrm{eV/atom}$. Very likely these clusters cannot be resolved in mobility experiments and additional signatures, like vibrational spectra, are needed to identify the exact geometry of the most stable structures.

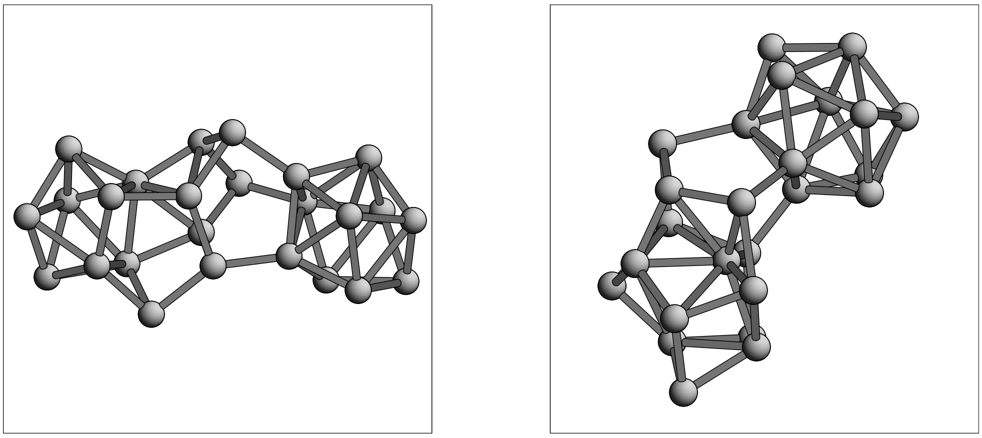

(a) $E = -3.96\,\mathrm{eV/atom}$, gap $= 1.3\,\mathrm{eV}$, $p = 0.52$

(b) $E = -3.96\,\mathrm{eV/atom}$, gap $= 1.0\,\mathrm{eV}$, $p = 0.39$

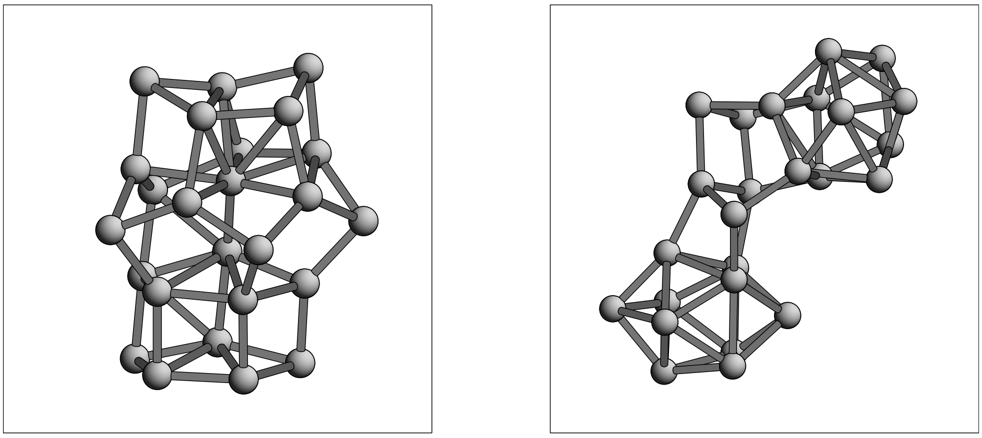

(c) $E = -3.96\,\mathrm{eV/atom}$, gap $= 1.1\,\mathrm{eV}$, $p = 0.15$

(d) $E = -3.97\,\mathrm{eV/atom}$, gap $= 1.0\,\mathrm{eV}$, $p = 0.49$

Figure 6.6: Low-energy isomers of Si_{25} with a large HOMO–LUMO gap.

Besides a low cohesive energy a large HOMO–LUMO gap for homo-nuclear systems is an indication that the electrons occupy states similar to covalent bonding states. The HOMO–LUMO gap as a function of prolateness is shown in Fig. 6.7. There is no direct correlation between the prolateness and the HOMO–LUMO gap for any of

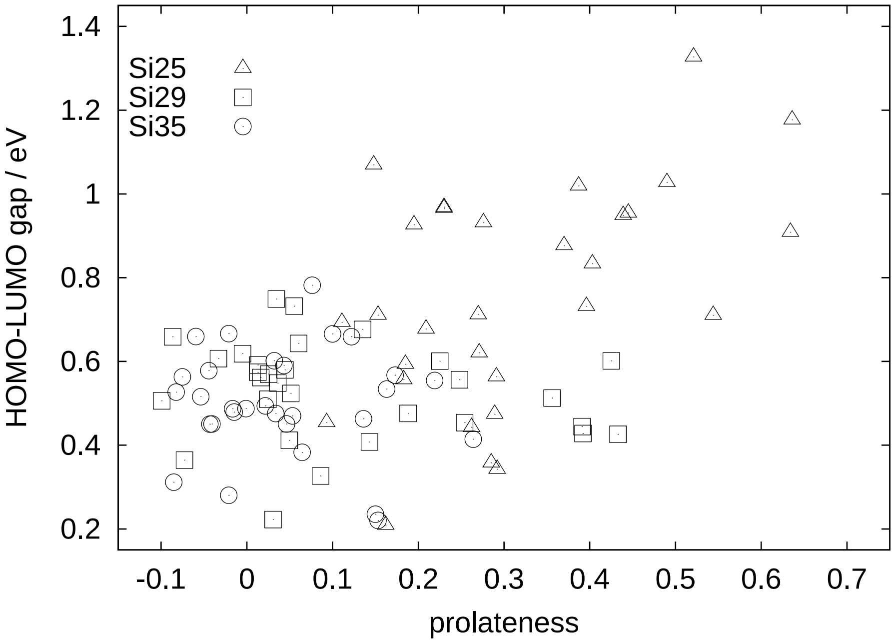

Figure 6.7: HOMO–LUMO gap vs. prolateness for the 30 most stable isomers of Si_{25}, Si_{29}, and Si_{35}. Gaps larger than 0.8 eV only occur for Si_{25} clusters.

the investigated cluster sizes. However, one striking feature in Fig. 6.7 is that some of the Si_{25} isomers have a quite large gap within SCC-DFTB, larger than 0.8 eV. Some of these isomers are depicted in Fig. 6.6. Three of the structures shown can be described as two smaller clusters connected by an intermediate fragment. The other structure (Fig. 6.6 (c)) is rather compact and has three highly coordinated atoms, which usually are related to metallic bonding.

The charge transfer, determined by a Mulliken-analysis, between silicon atoms of different coordination numbers does not exceed 0.2 e. For the compact spherical cluster Si_{25A} displayed top-left in Fig. 6.5 and on top in Fig. 6.8 the most negatively charged atoms are the three-fold coordinated atoms 11, 17 and 23 on the surface (see Tab. 6.2 and Fig. 6.8). The charge transfer is smaller in the prolate cluster Si_{25B} displayed top-right in Fig. 6.5 and at the bottom in Fig. 6.8. The contribution of the localized atomic orbitals to the different eigenstates for both isomers Si_{25A} and Si_{25B} are depicted in Fig.6.9 and in Fig.6.10, respectively. The LUMO of Si_{25A} is localized at atom 5, a fourfold coordinated atom on the surface. The HOMO is localized at atom 3, also a fourfold coordinated atom on the surface. Both atoms, 3 and 5, are bonded to the 6-fold coordinated atom 12, which neither contributes to the LUMO nor to the HOMO. The LUMO of Si_{25B} is mainly localized at two fourfold coordinated atoms (2 and 11) in the Si_9-fragment. The HOMO is mainly localized at the two widely separated atoms 7 and 23. These two atoms represent fivefold coordinated caps at the Si_{10}- and at the Si_9-fragment, respectively. Si_{25A} features a narrow HOMO–LUMO gap, whereas Si_{25B} features a wide gap of about 1.2 eV (see

	Si_{25A}		Si_{25B}	
No.	Charge/e	Coord.	Charge/e	Coord.
0	3.94	4	3.92	6
1	3.89	4	4.02	5
2	4.06	4	4.00	4
3	4.03	4	4.01	5
4	3.90	4	3.93	6
5	3.99	4	4.00	4
6	4.06	4	3.89	5
7	3.96	4	4.06	5
8	4.03	4	3.98	5
9	3.98	4	4.09	3
10	3.98	4	3.98	5
11	4.17	3	4.01	4
12	3.93	6	4.01	5
13	3.89	7	3.92	6
14	4.09	3	4.02	5
15	3.87	4	4.01	5
16	4.05	4	4.08	3
17	4.12	3	4.01	4
18	3.97	4	3.89	5
19	3.98	7	4.01	4
20	3.95	4	4.09	3
21	4.04	4	3.93	6
22	4.02	4	4.01	4
23	4.15	3	4.11	5
24	3.93	4	4.00	4

Table 6.2: Atomic charges determined by a Mulliken analysis and coordination numbers for Si_{25A} and Si_{25B}. Si–Si distances shorter than 2.82 Å are counted as bonds. The atom numbers refer to Fig. 6.8.

Fig. 6.11). The electronic density of states (DOS) just below the HOMO–level is higher for Si_{25B} than for Si_{25A}.

Since the differences in the cohesive energies are very small between the lowest-energy isomers (about 0.5 eV and 0.02 eV per atom), it is difficult to predict the ground-state structures for Si_{25}, Si_{29}, and Si_{35} from the SCC-DFTB calculations. This may be true for more sophisticated and more accurate methods like scf-DFT-GGA or Quantum Monte Carlo (QMC), too. Mitas et al. have calculated the cohesive energies of five low-energy isomers of Si_{20} with different first principles methods and find some subtle deviations in the energetic order between DFT-LDA, DFT-GGA with different exchange-correlation functionals, and QMC [87].

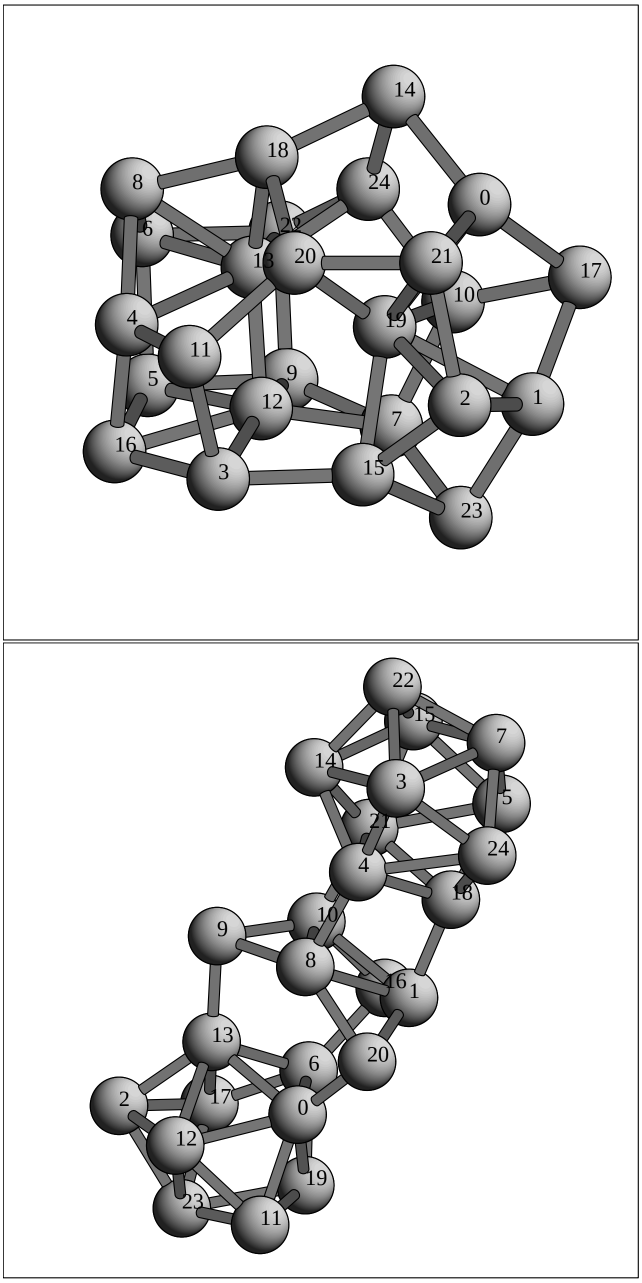

Figure 6.8: Atom numbering for the compact and nearly spherical cluster Si_{25A} (top) and for the prolate cluster Si_{25B} (bottom). Note that the numbers start with 0.

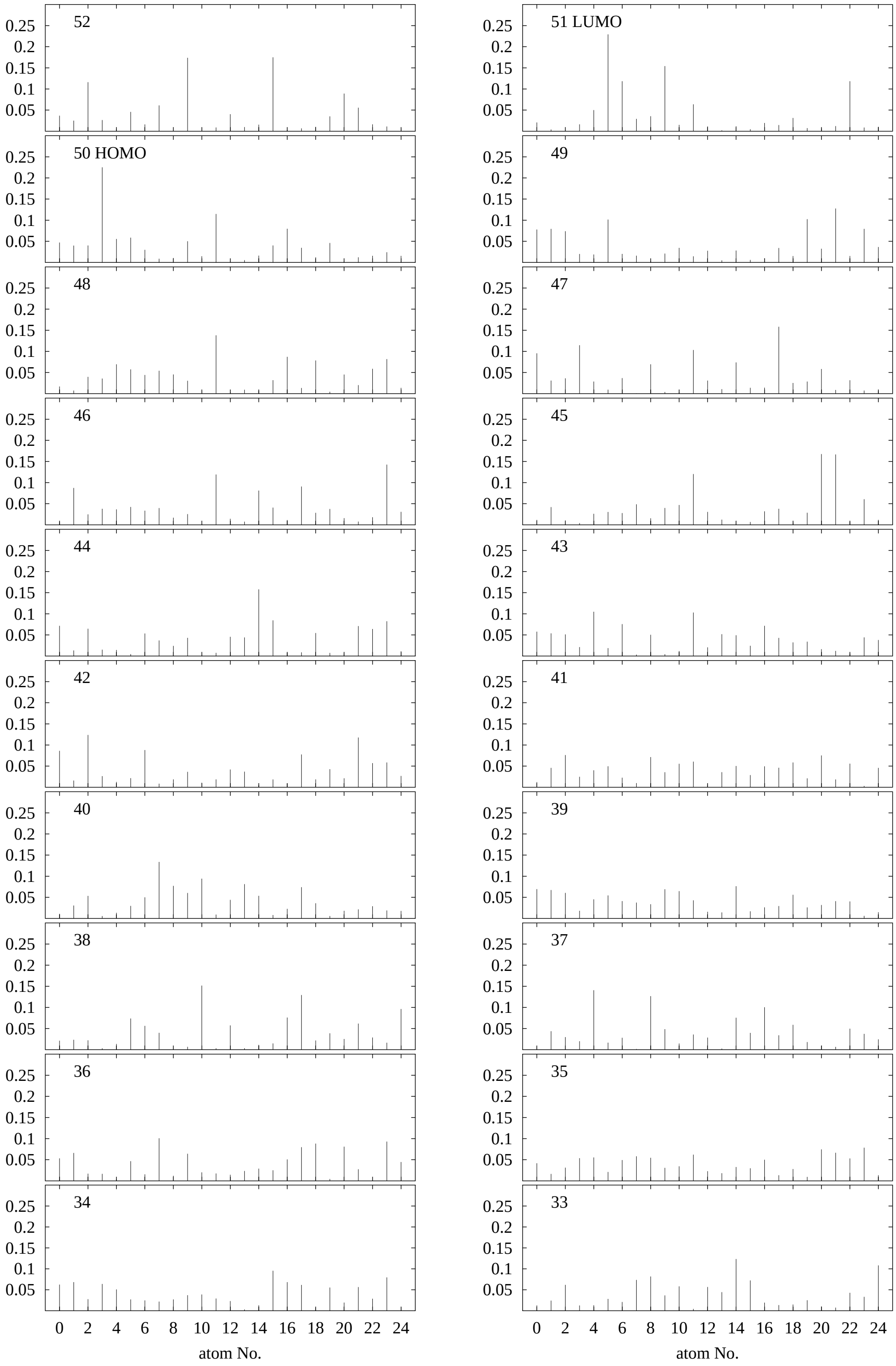

Figure 6.9: Contribution of the localized atomic orbitals to the different eigenstates of Si_{25A}. The levels from just above the LUMO (level 52) down to level 33 are shown. The atom numbers refer to Fig. 6.8.

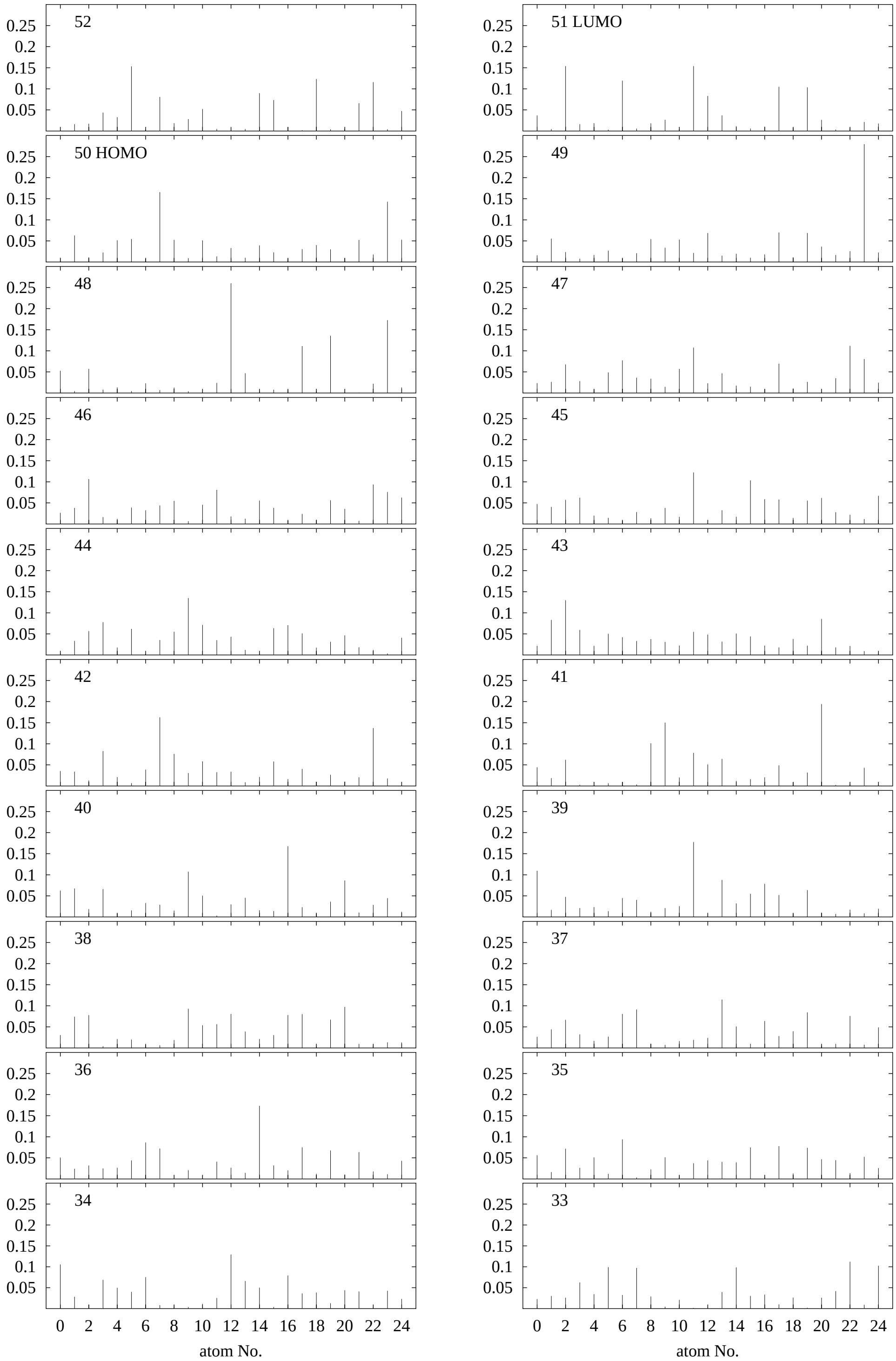

Figure 6.10: Contribution of the orbitals localized at one atom to the different eigenstates of Si_{25B}. The levels from just above the LUMO (level 52) down to level 33 are shown. The atom numbers refer to Fig. 6.8.

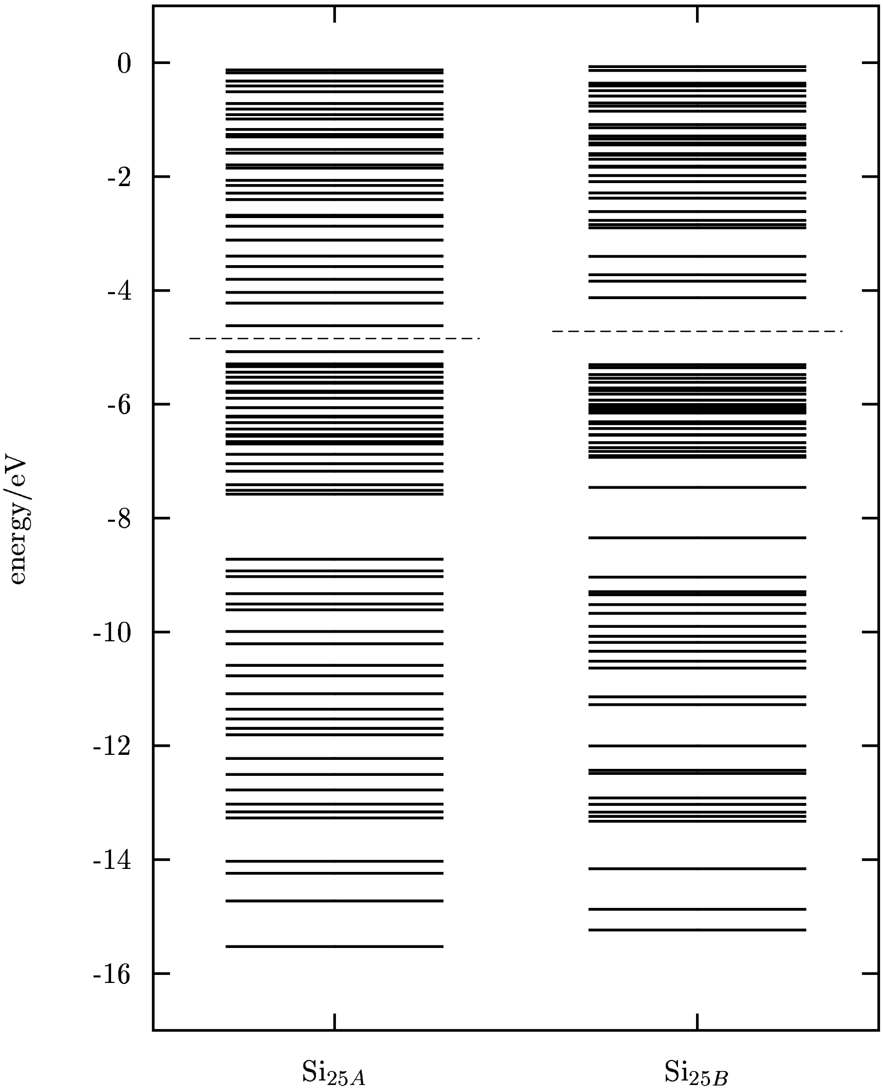

Figure 6.11: Eigenvalues of all occupied and the lowest non-occupied eigenstates for Si_{25A} (left) and Si_{25B} (right). The Fermi-levels are indicated by the two dashed lines.

6.3 Larger clusters with a bulk-like core

Regarding silicon clusters with more than 50 atoms no thorough investigations have been undertaken so far. Since the diamond structure is the most stable structure for bulk silicon, one expects very large silicon clusters to consist of a diamond-like (or mainly sp^3-hybridized amorphous) core with a relaxed surface.

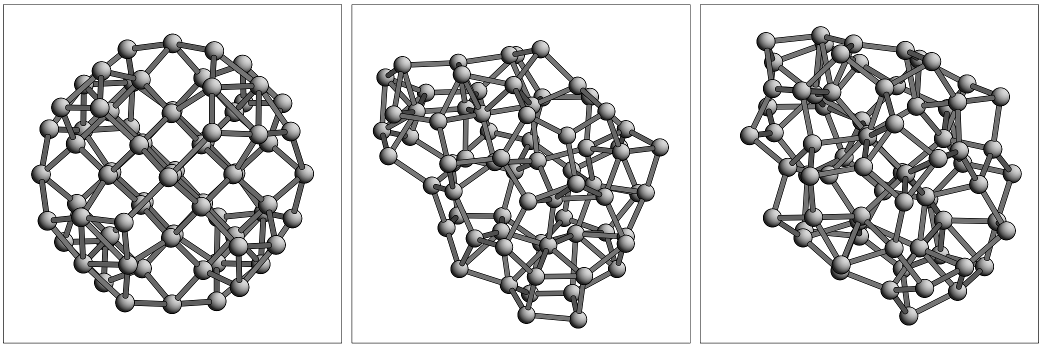

(a) $E = -3.96\,\text{eV/atom}$, gap $= 0.1\,\text{eV}$, $p = 0.0$ (b) $E = -4.11\,\text{eV/atom}$, gap $= 0.3\,\text{eV}$, $p = 0.14$ (c) $E = -4.11\,\text{eV/atom}$, gap $= 0.3\,\text{eV}$, $p = 0.09$

Figure 6.12: Three isomers of Si$_{71}$: (a) diamond sphere relaxed with conjugate gradient, (b) diamond sphere optimized with Simulated Annealing and (c) randomized sphere optimized with Simulated Annealing.

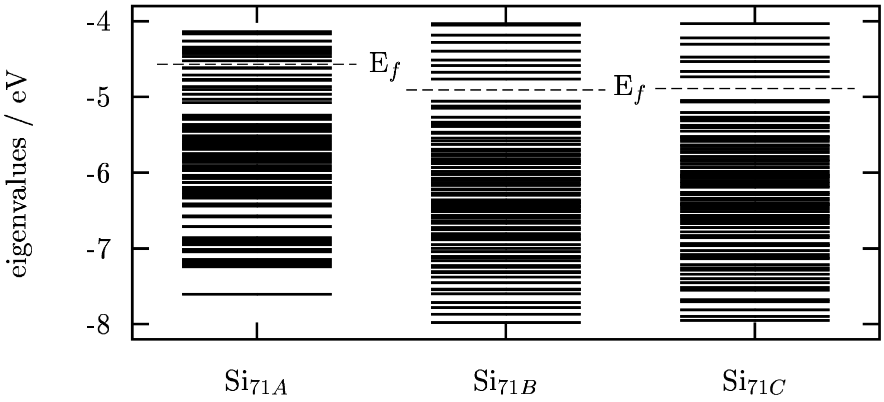

Figure 6.13: Kohn-Sham eigenvalues ε_i for the three structures of Si$_{71}$ displayed in Fig. 6.12. Only the part of the electronic-spectrum with $-8\,\text{eV} < \varepsilon_i < -4\,\text{eV}$ is shown. The Fermi-levels E_f are indicated by the dashed lines.

To determine the stability of a diamond-like core compared to other bonding-schemes a sphere with 71 atoms was cut from the diamond structure and its structure was optimized in two ways. In one case the diamond sphere was relaxed with the conjugate gradient method to the next local minimum to obtain a reconstructed surface. In the other case the diamond sphere was treated with Simulated Annealing to check if there exist different isomers with lower energies. Additionally, Simulated Annealing has been applied to a spherical and a prolate structure with 71 randomly distributed atoms and to a diamond sphere with 239 atoms.

The annealed diamond sphere has (within SCC-DFTB) a cohesive energy of −291.8 eV (−4.11 eV/atom). The two annealed randomized structure have a cohesive energy of −292.0 eV (−4.11 eV/atom) and −291.3 eV (−4.10 eV/atom). All three annealed structures have a cohesive energy about 10 eV lower than the cohesive energy of −281.0 eV (−3.96 eV/atom) of the relaxed diamond sphere. The cohesive energy of Si_{71} is still significantly higher than the −4.8 eV of the silicon diamond structure. The three annealed structures are quite similar, but are very different from the relaxed diamond sphere (see Fig. 6.12). They are compact and almost spherical (the annealed prolate structure as well), but their are some highly coordinated atoms and fewer ideal tetrahedral bonds. Some parts of the surfaces are concave, in this way some of the surface atoms can be fourfold coordinated with bond angles closer to 109° than possible on a convex surface. The annealed diamond sphere features 39 sp^3-like atoms, whereas the relaxed diamond sphere features 43 sp^3-like atoms. It follows that for this cluster size the ratio of surface to core atoms is still quite large. Therefore, a structure different from the diamond sphere with a reconstructed surface is favoured. The relaxed diamond sphere has a narrow HOMO–LUMO gap of about 0.1 eV within SCC-DFTB (see Fig. 6.13). The HOMO–LUMO gaps are wider (about 0.3 eV) for the annealed structures. The quite narrow HOMO–LUMO gaps are mainly due to surface-states close to the Fermi-level. Fragments from the ideal diamond structure with hydrogen-saturated surface atoms feature a wide HOMO–LUMO gap which is comparable to the gap of 1.1 eV in silicon diamond. The largest cluster treated with DFTB and Simulated Annealing is Si_{239}. The relaxed diamond sphere of this size has a cohesive energy of −4.19 eV/atom. After Simulated Annealing this sphere distorts into a compact disordered structure (see Fig. 6.14 (bottom)) similar to the annealed Si_{71} clusters. The annealed Si_{239} cluster has 42 threefold coordinated atoms, 39 fivefold coordinated atoms, 7 sixfold coordinated atoms, and 1 sevenfold coordinated atom. The cohesive energy is lowered to −4.24 eV/atom, this corresponds to 88% of the bulk cohesive energy. The HOMO–LUMO gap has a width of only 0.05 eV compared to 0.3 eV for the annealed Si_{71} structures.

From the theoretical and experimental investigations done so far, the following growth pattern for silicon clusters evolves:

- Silicon clusters with less than 10 atoms usually have a high symmetry and are compact.
- Silicon clusters with 10 to 20 atoms can be described as a tri-capped trigonal prism capped by several atoms or small fragments. For Si_{18} to Si_{22} some of the most stable clusters consist of two low-energy isomers of Si_9 to Si_{13} connected to form a single prolate structure.
- Between Si_{20} and Si_{30} a shape transition from prolate to compact and nearly spherical geometries occurs. Clusters with about 25 atoms have several low-energy isomers. Some of them can be described as two smaller clusters with

about 10 atoms connected by a small intermediate fragment, whereas others are compact and nearly spherical. The compact clusters have several five- or sixfold coordinated inner atoms.

- For clusters with more than 30 atoms the geometries evolve towards compact amorphous structures. For Si_{35} and also for Si_{71} the most stable isomers have a core quite different from the diamond structure with several highly coordinated atoms. For very large clusters with several thousand atoms one expects groundstate structures with sp^3-hybridized atoms in the core similar to crystalline or amorphous silicon. However, the lowest energy is not a sufficient criterion for the formation of structures during annealing in experiment.

The suggested growth pattern for silicon clusters is illustrated in Fig. 6.14. The occurrence of some highly coordinated atoms prevalent in the compact structures investigated could serve two purposes: (i) to saturate the dangling bonds of the surface atoms (which would otherwise be mostly threefold coordinated) and (ii) to act as "catalytic" centers and to enable the compact structures to relax through a sequence of rebonding and restructuring steps supported by their high coordination and their multiple weak bonds (previously this has also been pointed out in Ref. [87]).

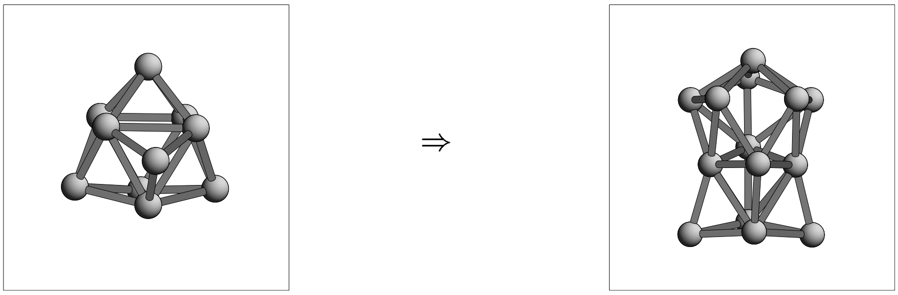

Si_{10} capped tri-capped trigonal prism Si_{14} capped and distorted TTP

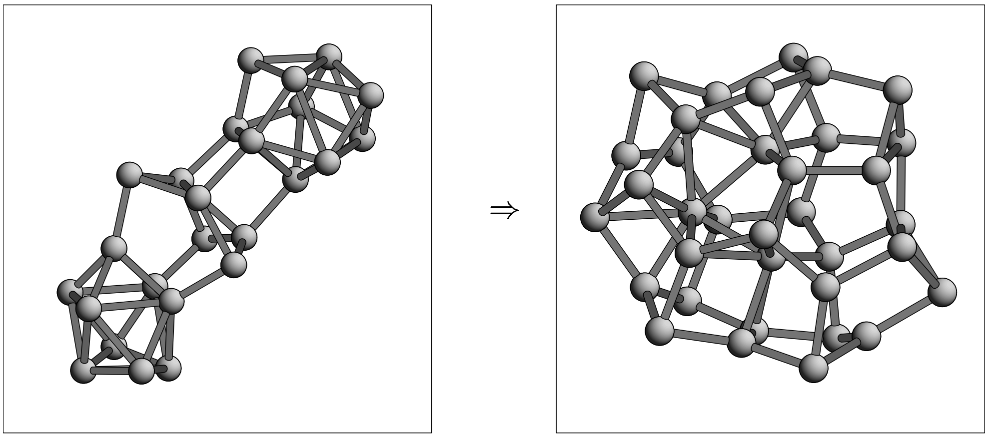

$Si_{25} = Si_9^* + Si_6$-ring + Si_{10}^* Si_{35} compact and amorphous

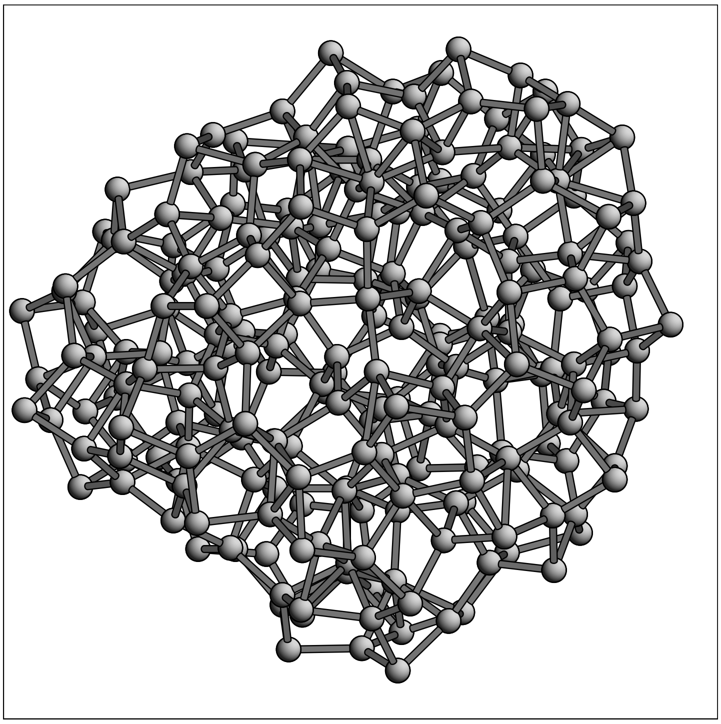

Si_{239} compact and amorphous with some highly coordinated atoms

Figure 6.14: Possible growth pattern for silicon clusters.

Chapter 7

Vacancy clusters in silicon

Vacancy clusters in bulk silicon are detected by electron paramagnetic resonance (EPR), positron annihilation spectroscopy (PAS), and other methods not only after damage (electron [88, 89, 90, 91] and neutron irradiation [92, 93, 94] or plastic deformation [95]), but also in as-grown samples [96]. Due to a lack of computational data on structure and stability of vacancy clusters detected in silicon in the 70th and 80th their size has been under discussion since. Based on a simple theoretical model, namely the counting of dangling bonds, it has been proposed [97] that closed ring structures of vacancies, such as for V_6 and V_{10}, should be particularly stable. Still, explicit and accurate calculations on the stability and structure of larger vacancy clusters in silicon and a reasonable comparison to experimental results are rare. Until recently, accurate *ab initio* calculations have been performed only for very small structures (mono- and divacancies) due to the limited size of the super-cell (64 atoms) used [98]. Using a small super-cell with 38 atoms the Hartree-Fock method has been applied to clusters with up to 8 vacancies [99]. Massive parallel computing has made it possible to treat larger super-cells, which seem to be necessary to obtain converged results even for mono- and di-vacancies [100, 101]. As of this writing, there exists only one approximative treatment based on quantum mechanics for clusters with more than 8 vacancies [102].

The self-consistent charge density-functional based tight-binding (SCC-DFTB) method described in Chapter 2 and References [15, 103] offers the unique possibility to treat larger structures nearly as accurate as with *ab initio* methods. For clusters consisting of more than 10 vacancies one has to consider large super-cells of about 500 atoms to avoid interactions between the extended defects and their periodic replica and to allow for an unbiased relaxation.

In contrast to metals, it seems to be impossible to determine the mono-vacancy formation enthalpy for silicon or other semiconductors in thermodynamic equilibrium by standard techniques (differential dilatometry or positron annihilation). Due to their relatively high formation enthalpy, no measurable amount of vacancies is created below the melting temperature in silicon. Therefore, it is not possible to directly compare calculated formation energies for defects in silicon to experimental data. Besides EPR, infrared absorption, deep level transient spectroscopy (DLTS), and other measurements, experimentally determined positron lifetimes along with a comparison to calculated lifetimes for different vacancy structures provide a link between theory and experiment.

7.1 Measurement and calculation of positron lifetimes

Positron annihilation (PA) spectroscopy is primarily sensitive to open volume defects such as vacancies or vacancy clusters, and dislocations in the bulk of crystals. The positron lifetime gives information about local electron densities around defects and can be correlated to the size of the open volume, i.e., the number of vacancies involved. The sensitivity of the positron trapping is dependent on the net charge of the trapping center. In the case of negatively charged defects the positron trapping rate shows a strong increase at low temperatures ($T < 100\,\mathrm{K}$), while neutral defects cause no comparable temperature-dependent trapping effect. Positrons are not sensitive to positively charged defects due to coulomb repulsion.

Using a weak radioactive ^{22}NaCl positron source the positron lifetime spectrum is monitored by measuring the time difference between the creation of the positron indicated by a 1.28 MeV γ quantum, and the annihilation γ rays of 0.51 MeV. The positron lifetime spectrum is considered as a sum of exponential decay terms. The relation between the lifetime spectrum and the positron lifetime components is modelled with the *trapping model* [95, 104, 105]. In the ideal crystal without defects only one component which is determined by the electron density in the ideal structure is present. If there is only one dominant defect type the positron lifetime spectrum consists of two components with intensities I_i and lifetimes τ_i, $(i = 1, 2)$. The first component is related to the ideal crystal and the second component is determined by the electron density at the defect. Its intensity reflects the defect concentration. In case of transition-limited trapping the trapping rate κ_d is proportional to the defect concentration N_d,

$$\kappa_d = \mu_d N_d.$$

The so-called specific trapping rate μ_d is a constant for a given material, defect type, and temperature. For extended positron traps such as voids the trapping is no longer transition limited but becomes diffusion limited. Then, the trapping rate is proportional to the product of the defect density N_d and the radius r of the defect (assuming the defect is spherical). The trapping rate for such an extended positron trap is calculated by

$$\kappa_d = 4\pi D_+ r N_d,$$

where D_+ is the positron diffusion constant.

In the simple trapping model one assumes that there is only one defect type which does not interact with other defects and that a trapped positron does not escape. Then, the lifetimes τ_1, τ_2 of the two components and the corresponding intensities I_i are given by

$$\tau_1 = \frac{1}{\frac{1}{\tau_b} + \kappa_d}, \quad I_1 = 1 - I_2, \tag{7.1}$$

$$\tau_2 = \tau_d, \qquad I_2 = \frac{\kappa_d}{\frac{1}{\tau_b} + \kappa_d - \frac{1}{\tau_d}},$$

where τ_b and τ_d are the positron lifetime in the bulk and that related to the defect, respectively. The trapping rate κ_d can be calculated from the decomposition of the lifetime spectra according to (7.1). It is possible to check whether the simple trapping model (one dominant defect, two components) is reasonable. The lifetime τ_1 calculated with (7.1) should coincide with the measured lifetime $\tau_{1,\mathrm{exp}}$. If this is not the case, one has to consider a multi-component model which takes into account more than one dominant defect. The lifetimes and the intensities are different, dependent on whether the defects are independent of each other (*capture model 1*) or not (*capture model 2*). In the case of two independent dominant positron traps d_1 and d_2 (three lifetime components) the lifetime components τ_i and their intensities I_i $(i = 1, 2, 3)$ are given by

$$\begin{aligned} \tau_1 &= \frac{1}{\frac{1}{\tau_b} + \kappa_{d_1} + \kappa_{d_2}}, \qquad \tau_2 = \tau_{d_1}, \qquad \tau_3 = \tau_{d_2}, \\ I_1 &= 1 - (I_2 + I_3), \\ I_2 &= \frac{\kappa_{d_1}}{\frac{1}{\tau_b} + \kappa_{d_1} + \kappa_{d_2} - \frac{1}{\tau_{d_1}}}, \qquad I_3 = \frac{\kappa_{d_1}}{\frac{1}{\tau_b} + \kappa_{d_1} + \kappa_{d_2} - \frac{1}{\tau_{d_1}}}. \end{aligned} \tag{7.2}$$

In general, it is difficult to resolve more than three lifetime components from measured spectra. However, if more than two dominant defects are present, they will introduce an error in the lifetimes derived from a model based only on two dominant defects.

7.2 Computation of positron lifetimes

Positron lifetimes for the perfect lattice and for different vacancy cluster configurations have been calculated using the superimposed-free-atom model by Puska and Nieminen [106] in the semiconductor approach [107]. The superimposed electron densities of free atoms form the background potential for which the Schrödinger equation for a positron is solved. This leads to the positron wave function Ψ_+. The enhancement of the electron density at the positron due to the electron-positron correlation is taken care of by the Boronski-Nieminen enhancement factor [108]. The annihilation rate λ is calculated as the overlap of the electron density n^- and the positron density $|\Psi_+(\mathbf{r})|^2$ increased by the enhancement factor Γ:

$$\lambda \propto \int \Gamma(n^-) n^-(\mathbf{r}) |\Psi_+(\mathbf{r})|^2 d\mathbf{r} \ . \tag{7.3}$$

To obtain accurate positron lifetimes, the super-cell has to be large enough to avoid interactions between positrons localized at adjacent vacancies of the super-lattice. An overlap of the positron wave function with regions of higher electron density in between the defects is known to lead to artificially small lifetimes.

While one finds large inward relaxations for silicon mono- and divacancies (if no positron is present), it is assumed that outward lattice relaxations under the influence of the trapped positron cancel out or even over-compensate the electronically induced inward relaxations [109]. Because the positron lifetime calculations do not take into account the influence of the trapped positron, the positron lifetimes calculated with respect to the unrelaxed geometries are compared to experimental data.

7.3 Experimental data on silicon vacancy clusters

Electron irradiation at low temperatures creates a high density of Frenkel pairs (mono-vacancies and interstitial atoms) far from thermodynamical equilibrium. The mono-vacancies lead to an experimentally detected positron lifetime around 275 ps and become mobile at about 150 K [110]. During this annealing stage the formation of di-vacancies is observed by a change in the defect-related positron lifetime to the range from 290 to 320 ps. Di-vacancies have been found to be stable up to a temperature of 550 K. At this temperature the di-vacancies dissociate and anneal, if the sample was irradiated with a low dose. However, they may form vacancy clusters, if the sample was treated with a higher irradiation dose and had initially a higher defect density.

Recent results on positron annihilation in neutron irradiated silicon [94, 111] and on high-dose electron irradiated silicon [88, 112] give a quite consistent picture on stable vacancy clusters formed during annealing by mobile primary defects: After neutron irradiation, larger vacancy clusters are formed during annealing around 870 K with defect-related positron lifetimes of $\tau_{\text{def}} = 420 \pm 20$ ps [94] (430 ± 30 ps [111]). After high-dose electron irradiation, vacancy clusters are found in the same temperature range (around 870 K) with positron lifetimes of $\tau_{\text{def}} = 415 \pm 20$ ps [112] (420 ± 30 ps [88]). In all these cases, annealing of the vacancy clusters takes place at about 1000 K. The errors given are estimated according to statistical errors, background and positron source corrections, and difficulties in decomposing the spectra [113, 114].

Considering the experimental results on deformed silicon, the picture emerging from experiments is somewhat different: While EPR indicates the presence of the Si-$P1$ paramagnetic center, significantly higher defect-related positron lifetimes than in irradiated material are found after a similar thermal treatment [95, 115, 116, 117]. High strain rates and low deformation temperatures (about 800 K) seem to favor much larger vacancy clusters: 590 ± 90 ps [95] (600 ± 50 ps [117]). This long lifetimes indicate trapping at positron states at the inner surfaces of large vacancy clusters. Lower deformation rates and/or higher deformation temperatures (about 1000 K) lead to significantly smaller defect-related positron lifetimes: $435 \ldots 480$ ps [118] or 485 ± 30 ps [117]. All defects, including vacancy clusters and dislocations, are found to anneal out around 1100 K [95, 117].

Experimentally detected defect-related positron lifetimes and, thereby, information on their size, have errors of typically 30 ps for larger vacancy clusters ($\tau = 400 - 500$ ps). It turns out that these errors are in the same range as the calculated lifetime differences between, e.g., V_{10} and V_{14}. Hence, the measured defect-related lifetimes cannot uniquely be related to a certain vacancy cluster size by just comparing experiments to positron lifetime calculations.

7.4 Calculated stability and positron lifetimes

Since the assignment of defect-related positron lifetimes to certain sizes of vacancy clusters is still under discussion, it is highly desirable to combine information on the stability of vacancy clusters and their respective annihilation parameters. Hence, the geometries and formation energies of various vacancy clusters in bulk silicon consisting of up to $n = 17$ vacancies in a $512-n$ super-cell have been determined [119]. The investigated structures include vacancy clusters where the atoms have been removed from a hexagonal ring-network, chains along $\langle 1\bar{2}1\rangle$ and along $\langle 110\rangle$ with 3 to 6 vacancies and some compact vacancy clusters. Chains of vacancies seem to play an important role during the creation of multi-vacancy clusters by plastic deformation. Additionally, the corresponding defect-related positron lifetimes have been calculated and compared to experimental data.

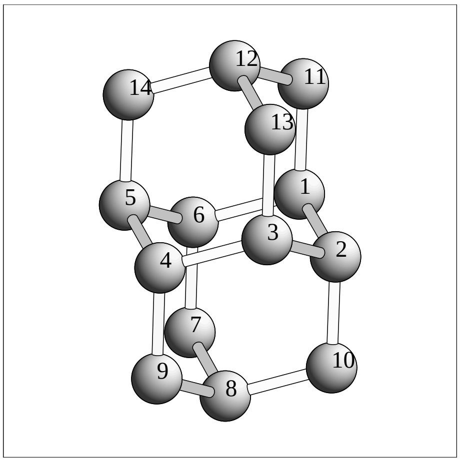

Figure 7.1: Atoms were successively removed from this hexagonal ring network starting with atom 1.

The structures have been relaxed with the self-consistent-charge density-functional based tight-binding (SCC-DFTB) method described in Chapter 2 and in References [15, 103] using a minimum basis-set and the Γ-point approximation. The efficiency of the SCC-DFTB method implemented on a parallel computer allows for the use of large super-cells with 512-n atoms [120]. Super-cells of at least 216 atoms are expected to be necessary to obtain converged results for the mono-vacancy [100]. For extended vacancy clusters even larger super-cells are needed. This is quite obvious if one compares the size of a $4 \times 4 \times 4$ super-cell with 8 atoms per unit-cell (side length 21.7 Å) with the diameter of, e.g., V_{14}, which is about 12 Å. The Si-Si interaction within DFTB is negligible for distances greater than 10 Å, therefore, the $4 \times 4 \times 4$ super-cell should be just large enough for neutral vacancy clusters as large as V_{14}. All structures have been relaxed until the maximum force on each atom dropped below 0.001 H/a_{B}.

For clusters with more than six vacancies many different configurations are conceivable. To limit the computational effort the focus has been put on candidates, which are likely to have low formation energies because of a small number of dangling bonds. As proposed before [97], vacancy structures where the removed atoms belonged to closed rings resulting in a minimum number of dangling bonds should be especially stable. For the hexa-vacancy cluster V_6 it has been found by Hartree Fock calculations [99] that the hexagonal ring is the most stable structure of all possible structures. Hence, the atoms have been removed in different ways from the 14 atom cage-like network displayed in Figure 7.1, to find the most stable vacancy clusters with up to $n = 14$ vacancies. Additionally, chain-like vacancies in the $\langle 1\bar{2}1\rangle$ direction (direction of jog-dragging in deformation experiments) and zigzag-chains in the $\langle 110\rangle$-direction with up to six vacancies have been considered to provide a comparison to more open vacancy clusters. For V_{10} and V_{17} the formation energies of compact vacancy clusters, where the nearest and some of the next-nearest neighbor atoms of a vacancy have been removed, have also been checked. For all relaxations a super-cell of $N - n$ (N=512) atoms and the lattice constant for the ideal crystal in DFTB of 5.43 Å have been used. The atoms around the vacancy have been randomly displaced by a small amount to allow for a symmetry unrestricted relaxation.

	Bond counting models					Quantum mechanical methods				
			simple	extended	TB [102]	DFTB			HF [99]	TB [102]
n	n_{b}	n_{n}	E_{F}^{n} [eV]	E_{F}^{n} [eV]	E_{F}^{n} [eV]	E_{F}^{n} [eV]	E_{X}^{n} [eV]	E_{D}^{n} [eV]	E_{D}^{n} [eV]	E_{D}^{n} [eV]
1	4	2	5.6	3.4	3.4	3.8	-1.8	0.0	0.0	0.0
2	7	4	8.4	3.9	5.2	5.8	0.2	1.8	1.7	1.6
3	10	5	11.2	5.6	7.1	8.0	-0.8	1.6	2.1	1.5
4	13	6	14.0	7.3	9.4	9.4	-0.6	2.4	1.9	1.2
5	16	7	16.8	9.0	10.7	10.1	-0.4	3.1	3.1	2.1
6	18	6	16.8	10.0	11.4	10.5	2.1	3.5	3.8	2.7
7	21	6	19.6	12.9	13.7	12.9	-0.8	1.4	1.3	1.1
8	24	7	22.4	14.6	14.1	14.5	-1.3	2.2	—	3.0
9	26	7	22.4	14.6	14.7	14.8	0.1	3.5	—	2.8
10	28	6	22.4	15.7	15.6	15.2	2.5	3.4	—	2.6
11	31	6	25.2	18.5	17.8	18.2	-1.7	0.8	—	1.2
12	34	7	28.0	20.2	18.3	19.5	-0.3	2.5	—	3.0
13	36	7	28.0	20.2	18.9	20.5	-0.3	2.8	—	2.8
14	38	6	28.0	21.3	19.6	21.2	0.9	3.1	—	2.7
15	41	6	30.8	24.1	22.0	22.8	-0.5	2.2	—	1.0
16	44	7	33.6	25.8	22.4	24.0	0.0	2.6	—	3.0
17	46	7	33.6	25.8	23.0	25.1	-0.7	2.7	—	2.8
18	48	6	33.6	26.9	23.8	25.6	—	3.3	—	2.7

Table 7.1: Formation energies E_{F}^{n} of different n-vacancy clusters as calculated within DFTB and empirical TB and dissociation energies E_{D}^{n} within DFTB, HF and empirical TB. Columns 2 – 5 correspond to the simple and extended bond counting models. The number of broken and new bonds are given by n_{b} and n_{n}, respectively.

To determine the relative stability of different n-vacancy cluster geometries, their formation energies

$$E_{\mathrm{F}}^{n} = E_{\mathrm{vac}}^{n} - \frac{N-n}{N} E_{\mathrm{cryst}}^{N} \quad , \tag{7.4}$$

are calculated, where E_{vac}^{n} is the total energy of the super-cell containing an n-vacancy cluster and $N - n$ atoms. E_{cryst}^{N} is the total energy of the defect-free super-cell of the same size. From this the *dissociation energy* E_{D}^{n} for the dissociation

$\mathrm{V}_n \rightarrow \mathrm{V}_{n-1} + \mathrm{V}_1$ is derived:

$$E_{\mathrm{D}}^{n} = (E_{\mathrm{F}}^{n-1} + E_{\mathrm{F}}^{1}) - E_{\mathrm{F}}^{n} \tag{7.5}$$

and the *exchange energy* E_{X}^{n} for the exchange reaction $2\,\mathrm{V}_n \rightarrow \mathrm{V}_{n+1} + \mathrm{V}_{n-1}$:

$$E_{\mathrm{X}}^{n} = (E_{\mathrm{F}}^{n+1} + E_{\mathrm{F}}^{n-1}) - 2\,E_{\mathrm{F}}^{n}. \tag{7.6}$$

Vacancy Cluster	remark	Atoms removed	E_{F}^{n}[eV]	E_{F}^{n}[eV] (ext. model)
V_4	$\langle 110\rangle$-chain		9.2	7.3
V_5	$\langle 110\rangle$-chain		11.5	9.0
V_6	$\langle 110\rangle$-chain		13.0	10.6
V_4	$\langle 1\bar{2}1\rangle$-chain		11.5	7.8
V_5	$\langle 1\bar{2}1\rangle$-chain		15.0	11.2
V_6	$\langle 1\bar{2}1\rangle$-chain		17.0	15.6
V_5	Lee/Corbett[93]	[2-4,12,13]	11.5	
V_8	single-ring	[1,2,4-6,8-10]	14.5	13.4
V_8	hexa-ring + 2	[1-6,10,14]	15.4	*
V_9		[1-6,9,10,14]	16.7	*
V_9		[1-6,7,9,10]	15.6	*
V_{10}		[1-6,9-11,14]	19.6	*
V_{10}	compact		18.0	*
V_{12}		[1-6,8-12,14]	20.0	*
V_{12}		[1-10,11,13]	20.4	*
V_{13}		[1-11,13,14]	21.5	*
V_{17}	compact		24.8	*

Table 7.2: Formation energies obtained with SCC-DFTB for vacancy clusters not following the straightforward construction scheme of the hexagonal ring network. The atom numbers in the third column refer to Figure 7.1. The vacancy clusters denoted *compact* consist of one vacancy plus four nearest neighbor vacancies and 5 next-nearest neighbor vacancies (V_{10}) and of one vacancy plus four nearest neighbor vacancies and 12 next-nearest neighbor vacancies (V_{17}).

For each vacancy cluster size n up to $n = 14$ those structures where one removes the atoms 1 to n from the 14 atom hexagonal ring-network displayed in Figure 7.1 have the lowest formation energies. The formation and dissociation energies of these structures calculated within SCC-DFTB are summarized in Table 7.1 and Figure 7.2. For comparison the same energies as calculated with an empirical tight-binding method [102] are given in Tab. 7.1, as well. Furthermore, for vacancy sizes up to V_7 the dissociation energies E_{D}^{n} obtained for the same configurations with a Hartree-Fock method are included [99].

Comparing the formation energies between SCC-DFTB and the empirical TB method one notices that the overall trend with increasing cluster size is similar. However, there are important deviations in the differences of the formation energies of one vacancy cluster size compared to the next larger size. This results in a different order in the dissociation energies. SCC-DFTB predicts V_6, V_{10}, and V_{14} to have high dissociation energies, whereas the empirical TB predicts maximum dissociation energies for V_6, V_8, V_{12}, and V_{16}. The SCC-DFTB dissociation energies agree much better with the corresponding HF energies. Only for V_3 the deviation of the SCC-DFTB value compared to the HF value is as large as within the empirical TB. Despite the fact that the Hartree-Fock method does not take into account correlation effects, the better agreement of the SCC-DFTB dissociation energies with the HF values is an indication for the SCC-DFTB to be more accurate than the empirical TB. Also the maxima in the SCC-DFTB dissociation energies for V_6, V_{10} and V_{14} are in agreement with the dangling-bond counting model [97].

Additionally, configurations of vacancy clusters, where arbitrary atoms (not the sequence of atoms 1 to n) have been removed from the 14 atom hexagonal ring-network displayed in Figure 7.1 have been considered and one finds the formation energies of them to be higher in energy (see Table 7.2). One exception being V_8, where atoms 1,2,4-6 and 8-10 in Fig. 7.1 have been removed. This single-ring structure also exhibits a low number of dangling bonds and, therefore, has about the same energy as V_8 with atoms 1 to 8 in Figure 7.1 removed. It is interesting to note that V_{12} (atoms 1-6,8-12,14 removed) is just the double hexa-vacancy ring which is a very stable vacancy clusters in GaAs [28].

Within SCC-DFTB, the chain-like vacancies in the $\langle 1\bar{2}1\rangle$-direction have significantly higher formation energies than the vacancy clusters of the same size taken from the hexagonal ring. Since the even-numbered types of these chain-like vacancies consist of "isolated" nearest-neighbor vacancy-pairs, their formation energies are roughly multiples of the formation energy of the di-vacancy (5.8 eV). The formation energies for the "zigzag" chains along $\langle 110\rangle$ for V_4 to V_6 are higher compared to the vacancy clusters of the same size taken from the hexagonal ring, as well. Additionally, the energies of two *compact* vacancy clusters, namely, a compact V_{10}, where one atom along with its four nearest neighbors plus five of the next-nearest neighbors had been removed, and a compact V_{17}, where one atom along with its four nearest neighbors and all its 12 next-nearest neighbors had been removed, have been calculated. The formation energy of the compact V_{10} structure is higher by 2.8 eV compared to the adamantane cage V_{10}. But, the compact V_{17} structure exhibits a significantly lower formation energy than the V_{17} structure, where one removes all 14 atoms displayed in Fig. 7.1 along with three atoms from an adjacent hexagonal ring. All the formation energies of the vacancy clusters different from the structures where one removes atoms 1 to n in Fig. 7.1 are summarized in Tab. 7.2. The tight-binding calculations suggest that for all sizes up to V_{14} vacancy clusters built from the set of atoms indicated in Fig 7.1 are the most stable. For vacancy clusters larger than V_{16}, the more compact structures become competitive in energy due to a higher flexibility in the relaxation pattern compared to the ring structures. The transition from the construction model for hexagonal rings to the compact spherical growth pattern is predicted by SCC-DFTB for a smaller vacancy cluster size than by the empirical TB method in [102]. There, the compact spherical shaped V_{24} was found to be the smallest vacancy cluster having a formation energy below the hexagonal ring cluster of the same size.

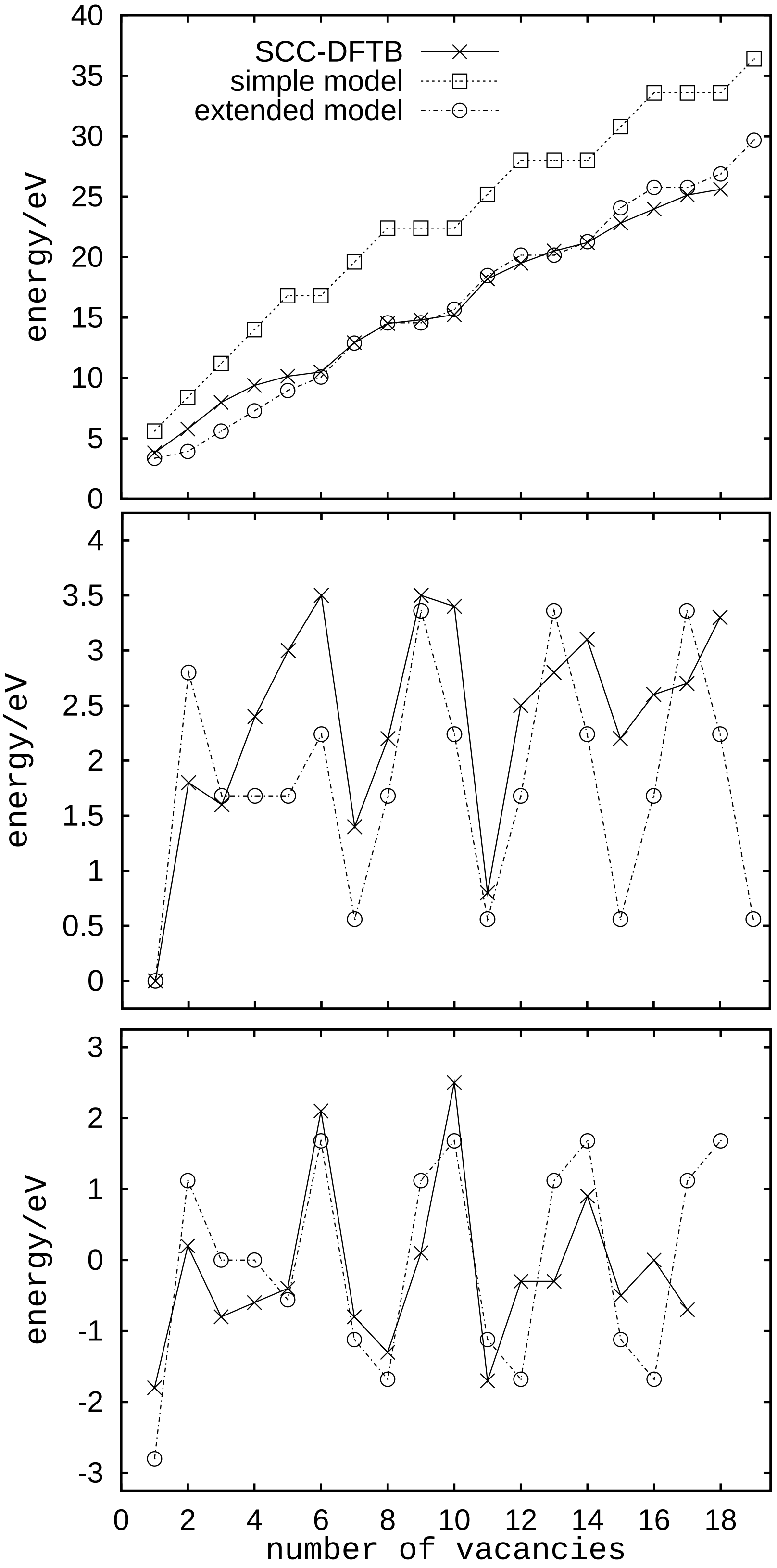

Figure 7.2: (Top) Formation energies in eV as a function of the number of vacancies calculated within SCC-DFTB, the simple bond-counting model and the extended bond-counting model (see text). (Middle) Energies in eV for the dissociation $V_n \to V_{n-1} + V_1$ within DFTB and the extended bond-counting model. (Bottom) Energies in eV for the exchange reaction $2\,V_n \to V_{n+1} + V_{n-1}$ within DFTB and the extended bond-counting model.

For smaller vacancy defects the tight-binding results can be compared to results obtained from sophisticated *ab initio* methods:

In silicon, the mono-vacancy with T_d-symmetry is Jahn-Teller instable and distorts into D_{2d}-symmetry. The SCC-DFTB method yields for the latter symmetry a formation energy of $E_\mathrm{F}^1 = 3.8\,\mathrm{eV}$, which is in reasonable agreement with other first principles calculations (3.27 eV [100], 3.49 eV [121] and 3.29 eV [98]). The symmetry-breaking results in two different nearest neighbor distances between the four atoms surrounding the vacancy. The relaxation with the SCC-DFTB method yields distances of 2.8 Å and 3.0 Å, while Antonelli et al.[121] find two slightly distinct distortions with identical formation energies. They have calculated the distances to be 3.0 Å and 3.5 Å for their structure A and 3.4 Å and 3.5 Å for their structure B. Puska et al.find with a 216 atoms super-cell using the Γ-point and a pseudo-potential plane-wave code 2.9 Å and 3.4 Å [100]. The calculations indicate a very flat potential in the direction of the distortion, which makes it difficult to determine the exact equilibrium distances. The nearest neighbor distance in bulk silicon is 2.35 Å.

Taking two nearest neighbor atoms away from the ideal crystal yields a Jahn-Teller instable D_{3d} configuration for V_2, which distorts within DFTB into C_{2h} symmetry, corresponding to the resonant-bond configuration in [101]. The three nearest neighbors of each of the two removed atoms built an isosceles triangle with two edges of 2.8 Å and one edge of 3.4 Å. In the undistorted crystal these three atoms built an equilateral triangle with an edge length of 3.8 Å, the second neighbor distance. During the relaxation, the two triangles shorten their distance by about 0.3 Å. That means, there is an inward relaxation and the volume of the di-vacancy is reduced. A recent result with a plane-wave pseudo potential approach and a 216 atom super-cell gives $E_\mathrm{F}^2 = 4.94\,\mathrm{eV}$ and a binding energy of $E_\mathrm{D}^2 = 1.6\,\mathrm{eV}$ [122, 123], close to the DFTB result of 1.8 eV. A formation energy of $E_\mathrm{F}^2 = 5.8\,\mathrm{eV}$ for the di-vacancy is obtained with SCC-DFTB. This value is very close to the 5.7 eV found by Song et al.with a TB approach [124], but deviates by more than 1 eV from the 4.3 eV calculated by Seong et al.[98] with a first principles DFT-LDA plane-wave code. However, the authors stated that their results were neither fully converged with respect to the basis set nor to the size of the super-cell.

Comparing the stability between vacancy clusters of different sizes, one finds V_6 and V_{10} having "surfaces" consisting of adjacent closed vacancy hexagonal rings (see Figure 7.3 and Figure 7.4) to be especially stable. Both vacancy clusters have low relative formation energies (compared to the next larger vacancy cluster as shown in Figure 7.2) and a high stability against dissociation into $\mathrm{V}_{n-1}+\ \mathrm{V}_1$ and the exchange reaction $2\mathrm{V}_n \longrightarrow \mathrm{V}_{n+1} + \mathrm{V}_{n-1}$ (see Figure 7.2). For V_{10} this is in agreement with more qualitative predictions [97] and for V_6 additionally with other calculations [99]. With respect to E_D also V_9, V_{13} and V_{14} are especially stable.

In the super-cell with the hexagonal ring vacancy cluster V_6 both of the two atoms positioned next to a vacancy site shorten their distance during relaxation from 3.8 Å, the next-nearest neighbor distance in the ideal crystal, to 2.7 Å. Assuming distances less than 2.8 Å as bonds, all atoms in this relaxed vacancy cluster are fourfold coordinated (cf. Figure 7.3 (b)). The bond angles ranging from 98 to 145°, however, deviate substantially from the tetrahedral bond angle of 109°. In total, 6 new bonds

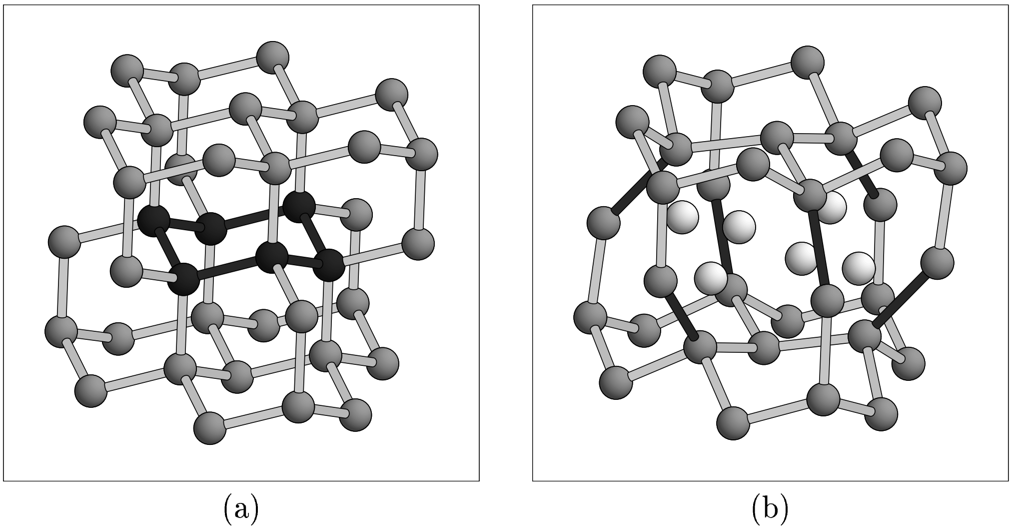

Figure 7.3: Bulk-fragment around V_6. Black atoms and bonds represent the removed atoms forming a hexagonal ring of V_6 in the ideal crystal (a). In (b) the relaxed atoms around V_6 are shown. White spheres represent the positions of the removed atoms. The six new bonds formed in the relaxed structure are drawn in black. No three-fold coordinated atoms are found in this structure.

for the hexa-vacancy cluster are formed (see Figure 7.3).

The nearest neighbor arrangement is different in the V_{10} vacancy cluster, the adamantane cage (see Figure 7.4). Here, four atoms have, in addition to one neighboring vacancy site, three empty next-nearest neighbor sites and, therefore, remain threefold coordinated after the relaxation (see Figure 7.4 (b)). Similar to the case of the hexagonal ring vacancy cluster, the other atoms around the vacancy cluster build new bonds (2.65 Å long) to a next-nearest neighbor (cf. Figure 7.4). For V_{10} the total number of new bonds formed is 6 the same as for V_6. The formation of one of these six new bonds in V_{10} is illustrated in Figure 7.5. The electronic density between the two atoms is significantly increased compared to the density between two next-nearest neighbors in the ideal crystal, but not as high as between two nearest neighbors in the ideal crystal. The unrelaxed V_{10} vacancy cluster has full T_d-symmetry resulting in a three-fold degenerate highest occupied molecular orbital (HOMO) which is occupied by 2 electrons. The symmetry unrestricted relaxation changes the three-fold degenerate HOMO into one two-fold (the new HOMO) and one non-degenerate state. The energy difference between these two states is only 0.005 eV. The Jahn-Teller distortion in V_{10} is much weaker than in the monovacancy, because the overlap between the interacting orbitals is much smaller.

In the cage-like V_{14} vacancy cluster there are eight vacancy sites with three nearest neighbor vacancy sites and, therefore, this vacancy cluster has eight only three-fold coordinated atoms (cf. Figure 7.6 (b)). Again the total number of new bonds formed is 6, and, hence, is the same as for V_6 and V_{10}.

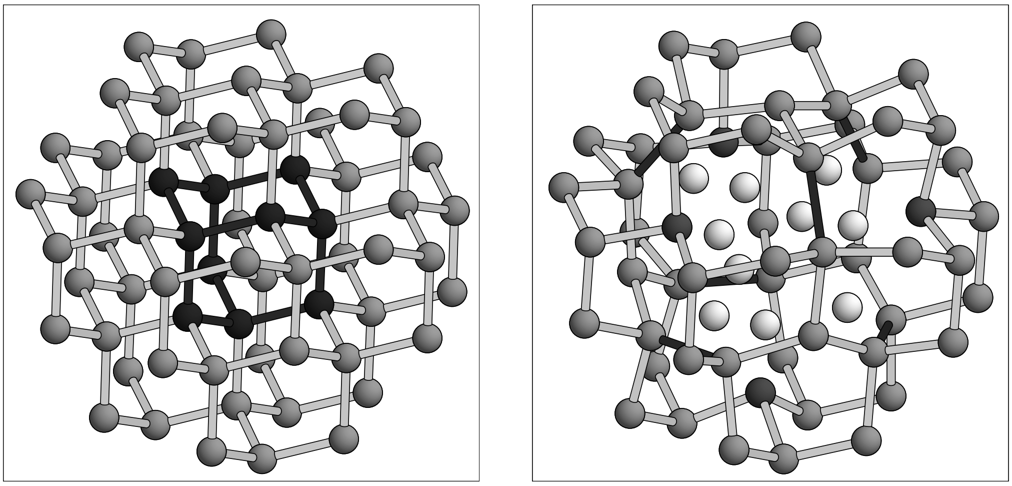
(a) (b)

Figure 7.4: Bulk-fragment around V_{10}. Black atoms and bonds represent the removed atoms forming a cage of V_{10} in the ideal crystal (a). In (b) the relaxed atoms around V_{10} are shown. White spheres represent the positions of the removed atoms. The six new bonds formed in the relaxed structure are drawn in black. Four three-fold coordinated atoms found in this structure are displayed darker than the others.

Summarizing the results about the stability of the different configurations, the hexagonal ring V_6 and V_{10} as well as V_{14} vacancy clusters — build from adjacent hexagonal rings — have minimum numbers of dangling bonds in the relaxed structure. All atoms surrounding the V_6 vacancy cluster are fourfold coordinated, while in the V_{10} adamantane cage structure 4 atoms remain threefold coordinated and V_{14} has 8 only threefold coordinated atoms. Nevertheless, V_{10} is as stable as V_6, because the energy increase by the three-fold coordinated atoms is compensated by the new bonds formed being closer to the ideal lattice bond length. On the other hand, this effect is less pronounced in larger vacancy clusters ($n > 15$), where the relative stability is expected to be weakened according to the large number of threefold coordinated atoms introducing additional dangling bonds. The lower formation energy of the compact V_{17} compared to the vacancy hexagonal ring structure V_{17} indicates that for the larger vacancy clusters hexagonal ring structures are not the most stable ones.

Results from quantum-theory based calculations for covalently bonded systems in some cases can be interpreted within a *simple bond-counting model.* Here, the cohesive energy of the system is approximated by the number of bonds times E_b, the energy per bond in the ideal crystal, and relaxation is neglected. This corresponds to the dangling-bond-counting model applied in [97], where it is suggested that the closed hexagonal ring networks (V_6, V_{10}, and V_{14}) should be especially stable due to their relatively low number of dangling bonds. Based upon the SCC-DFTB results for the relaxed structures it is necessary to extend this simple model by taking into account the energy gained by the formation of new bonds. In this *extended bond-*

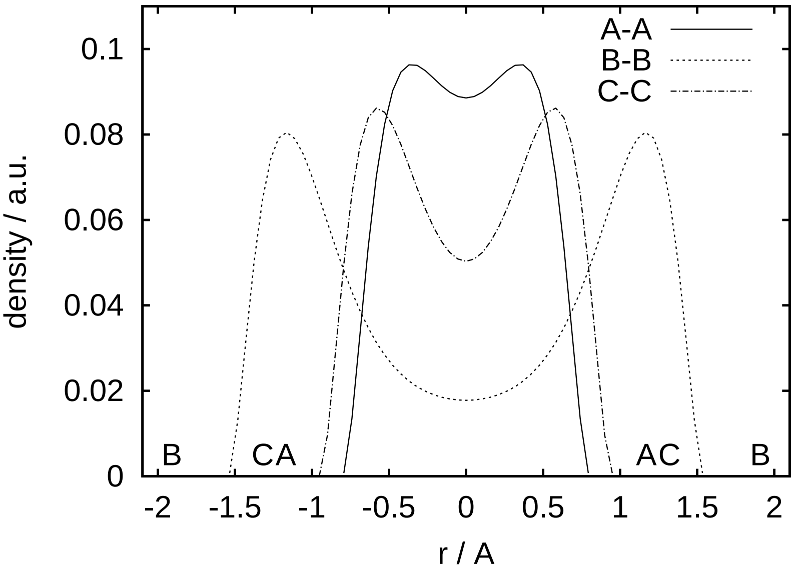

Figure 7.5: Electron density along the bond axis. A–A denotes two nearest neighbor atoms (distance 2.35 Å) and B–B denotes two next-nearest neighbor atoms (distance 3.8 Å) in the ideal crystal. C–C denotes two atoms in V_{10}, which were next-nearest neighbor in the ideal crystal, but shortened their distance to 2.65 Å during relaxation. The positions of the atoms A, B and C are indicated on the lower border. Only the central density in between two nodes is shown. The density localized at the nuclei is not shown.

counting model the cohesive energy compared to the simple bond-counting model is lower by the number of new bonds times the average energy per new bond. Generally, for those vacancy positions where prior to removal the removed atom had at least two bonds to the surrounding crystal (and not to another vacancy site) a new bond is formed between two atoms in the surrounding crystal. In contrast, for those vacancy positions where the removed atom had only one bond to the surrounding crystal (and three to other vacancy sites) a dangling bond is created. The number of broken bonds n_{b} and new bonds n_{n} and the formation energies estimated within the simple and extended bond-counting models for the cases where the atoms have been successively removed from the hexagonal ring network with 14 vacancies (Figure 7.1) are given in Table 7.1. Here, $E_{\mathrm{b}} = 2.8\,\mathrm{eV}$ per bond, the binding energy per bond in the ideal crystal within SCC-DFTB, is used. The newly formed bonds are weaker than the bonds in the ideal crystal and their formation is accompanied by the weakening of some of the ideal tetrahedral bonds. The average energy for a new bond is set to $0.4\,E_{\mathrm{b}}$. This value yields formation energies close to those calculated within SCC-DFTB. The details of the simple and of the extended bond-counting models can be found in the last Section of this Chapter.

By comparing the formation and dissociation energies as a function of n as calculated within DFTB to those estimated from the extended bond-counting model (Figure 7.2), one notices that the extended bond-counting model reproduces the form-

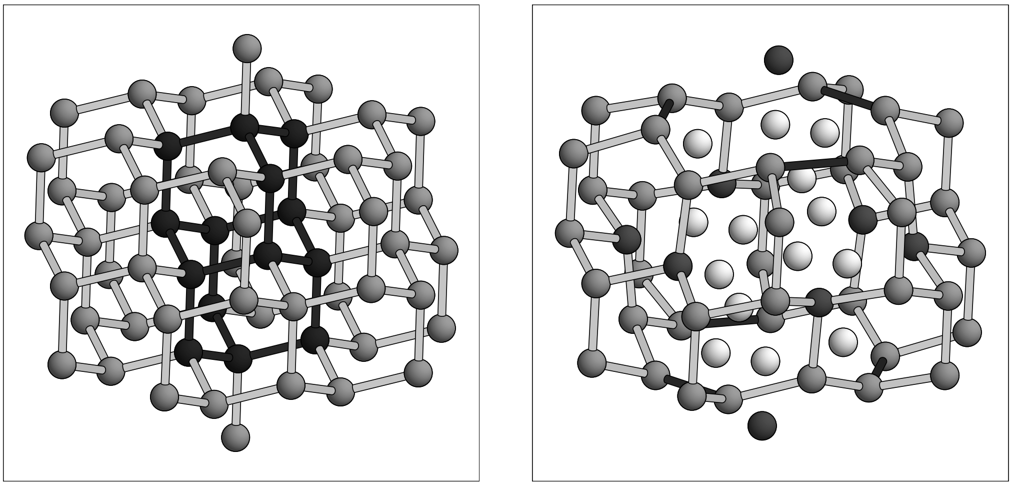
(a) (b)

Figure 7.6: Bulk-fragment around V_{14}. Black atoms and bonds represent the removed atoms forming a cage of V_{14} in the ideal crystal (a). In (b) the relaxed atoms around V_{14} are shown. White spheres represent the positions of the removed atoms. The six new bonds formed in the relaxed structure are drawn in black. The eight three-fold coordinated atoms found in this structure are displayed darker than the others.

ation energy of DFTB as a function of vacancy size n very accurately in the range $6 \leq n \leq 14$. Furthermore, this model yields local maxima in E_{D}^{n} at $n = 2, 6, 9, 13$, and local maxima in E_{X}^{n} at $n = 2, 6$, and 10, in agreement with the tight-binding calculations. However, the simple and the extended bond counting model are less predictive for very small and for larger vacancy clusters, where the bonding scheme is more complex. The energy differences for different vacancy structures of the same size predicted by the extended bond-counting model deviate from the calculated energy differences in some cases. Within this model, the formation energies for the "zigzag" chain-like vacancies along $\langle 110 \rangle$ V_4 and V_5 are the same as for the vacancy clusters of the same size defined by Figure 7.1, whereas the SCC-DFTB calculations yield significantly lower energies for the latter structures. Also, the single-ring vacancy structure V_8 (atoms 1,2,4-6,8-10 in Fig. 7.1 removed) is favored by the extended bond-counting model, whereas the SCC-DFTB-calculations yield the same formation energies for this structure and V_8 where atoms 1 to 8 in Figure 7.1 have been removed.

When discussing irradiation experiments low formation and high dissociation energies of certain cluster sizes are not the only criteria for their formation and stability. The kinetics of the primary defects which become mobile during annealing of the irradiated samples has to be taken into account, too. The most important point is the relation between the primary defect density and the density of sinks for mobile defects (mainly mono-vacancies). Typical sinks in irradiated Czochralski-grown silicon are oxygen-related micro-defects. As a result there is always competition between annealing and agglomeration.

	Positron Lifetime			
	not relaxed	relaxed	relaxed [109]	experiment [91]
n	τ [ps]	τ [ps]	τ [ps]	τ [ps]
bulk	218		215	218
1	253	218	279	282
2	303	240	309	310
3	329	278	320	
4	343	291	337	
5	353	301	345	
6	375	317	348	
7	383	330		
8	389	364		
9	398	368		
10	420	385		
11	422	392		
12	425	402		
13	427	406		
14	435	414		

Table 7.3: The defect related positron lifetimes have been calculated for the unrelaxed and the relaxed structures. For comparison the known experimental values [91] and those calculated within two-component density-functional theory [109] are provided for the smaller vacancy clusters.

To allow for a direct comparison to experimental data the defect-related positron lifetimes – given in Table 7.3 and Figure 7.7 – have been calculated. Besides the positron lifetimes calculated with respect to the unrelaxed atomic positions the lifetimes calculated with respect to the coordinates after relaxation by the SCC-DFTB method are included for comparison. As outlined above, the calculated lifetimes obtained from the unrelaxed geometries should better match the measured lifetimes.

The positron lifetimes in Figure 7.7 have been calculated using the unrelaxed coordinates. The lifetimes increase with increasing cluster size, since the electron density decreases at the location of the vacancy cluster where the positron is trapped. For larger vacancy agglomerations the influence of the trapped positron on the atomic positions should decrease. Additionally, as shown in Table 7.3 the influence of the inward lattice relaxation without a positron decreases. Since the potential around the equilibrium geometry is in general very flat for silicon, one expects even for large clusters like V_{14} or V_{17} an influence of the trapped positron pushing the atoms slightly outward and, therefore, a better agreement with experimental data for the lifetimes obtained from the unrelaxed structures. For the most stable vacancy clusters the positron lifetimes $\tau_{V_6} = 375\,\mathrm{ps}$, $\tau_{V_{10}} = 420\,\mathrm{ps}$, and $\tau_{V_{14}} = 435\,\mathrm{ps}$ are obtained (see Figure 7.7 and Table 7.3). The positron lifetime for vacancy chains is very close to the value obtained for di-vacancies even for longer chains (cf. Figure 7.7).

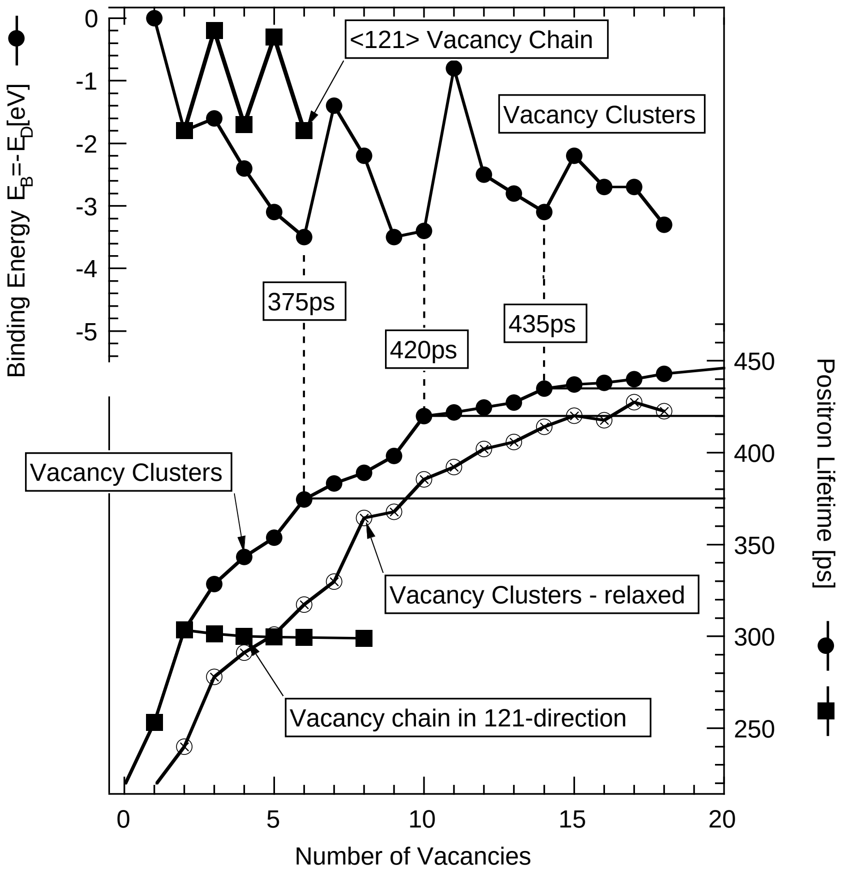

Figure 7.7: Energy gained by adding a mono-vacancy to a cluster of $(N-1)$ vacancies in silicon (upper part) and the corresponding positron lifetimes (lower part) for unrelaxed vacancy clusters. Positron lifetimes for the particularly stable vacancy clusters V_6, V_{10}, and V_{14} are highlighted.

7.5 Linking theory and experiment

A recent work about the defect-related positron lifetime in mono-vacancies reports $\tau_{V_1} = (282 \pm 5)\,\mathrm{ps}$ and that mono-vacancies become mobile at 170 K [91]. The temperature range for the dissociation of di-vacancies has been determined to be around 550 K. This corresponds to the SCC-DFTB result of a di-vacancy dissociation energy of 1.8 eV. The activation energy for the migration of mono-vacancies according to an empirical TB result is estimated to be 1.54 eV [102]. A relationship between the annealing temperature and the activation energy can be established by transition-state-theory (see Appendix C). The following assumptions are made to compare experimentally determined annealing temperatures of defects and the corresponding calculated dissociation energies for different clusters: (i) The barrier height for the diffusion of vacancies away from a cluster is always the same, (ii) the entropy pre-factors in the Arrhenius term are almost equal, (iii) the number of jumps to the nearest sink is comparable. The calculated dissociation energies are scaled to that of the di-vacancy (1.8 eV) which is experimentally well characterized and anneals at 550 K.

During annealing of irradiated samples between 550 and 1000 K, the formation of vacancy clusters larger than V_2 is observed by EPR and PAS. Di-vacancies appear to dissociate and to migrate to form larger vacancy clusters: V_4 is detected by EPR in the temperature range 573 ... 623 K, while the Si-$P1$ EPR center — associated in [93] to the non-planar penta-vacancy V_5 — is detected for $T = 620 \ldots 720\,\mathrm{K}$ [92, 93]. In the same temperature range, the defect related positron lifetime is rising from $\tau_{\mathrm{def}} \approx 310\,\mathrm{ps}$ to values $\tau_{\mathrm{def}} \approx 330 \ldots 350\,\mathrm{ps}$ [89, 111, 112]. This would correspond to V_4 or V_5 defects.

When the Si-$P1$ EPR center is not detectable anymore ($T > 720\,\mathrm{K}$), PAS detects a value of $\tau_{\mathrm{def}} \approx 360\,\mathrm{ps}$ [111, 112]. This signal could be due to the V_6 vacancy ring, which may be invisible by EPR, because it has most likely a neutral charge state (see also [99, 125]). For a sufficiently high defect density, τ_{def} keeps on rising with temperature until a saturation value of $\tau_{\mathrm{def}} \approx 420 \ldots 430$ is reached at about $T = 870\,\mathrm{K}$ [111, 112]. Recent first-principles calculations of defect-related positron lifetimes for several sizes of vacancy clusters in silicon [109, 126, 127] give positron lifetimes not larger than 360 ps which are related to positron trapping into vacancy clusters with five or less vacancies. The calculated positron lifetimes for the unrelaxed structures are 375 ps for V_6, 420 ps for V_{10}, and 435 ps for V_{14}. Combining this information with results on the stability of the vacancy clusters (this work and others [97, 99]) suggests that the larger stable clusters are good candidates for the defects related to a positron lifetime of about 430 ps measured in irradiated silicon annealed up to $T = 870\,\mathrm{K}$. While V_{10} may be formed by successively capturing a mono-vacancy, it is more unlikely for V_{14}, due to the small dissociation energy $\mathrm{V}_{11} \rightarrow \mathrm{V}_{10} + \mathrm{V}_1$.

Under the assumptions (i) – (iii) made above, the dissociation energies for V_6, V_9, and V_{10} would correspond to annealing at about 1000 K — indeed very close to the experimentally detected annealing temperatures of larger vacancy clusters with lifetimes of 420 to 430 ps) [89, 111, 112].

It is interesting to note that for medium dose electron irradiation ($1 \times 10^{19}\,\mathrm{cm}^{-2}$ at 6 MeV) the experimentally found defect related positron lifetime is $\approx 350\,\mathrm{ps}$ [89], and, hence, is close to the lifetime calculated for V_6.

Comparing the dominating vacancy related defects after high-dose irradiation treatment and annealing up to 870 K with the calculated positron lifetimes one can most likely rule out V_6. The calculated positron lifetimes for the most stable structures are: V_6 (375 ps), V_9 (398 ps), V_{10} (420 ps), and V_{14} (435 ps). The experimentally observed defect-related positron lifetimes range from 415 to 430 ps and have errors of roughly 30 ps. Only moderate dose electron irradiation followed by annealing up to 650 K could lead to V_6.

In conclusion, the dominating defects determined experimentally in the temperature range $T \approx 870 \ldots 1000\,\mathrm{K}$ are most likely the vacancy clusters V_9 and V_{10}. It becomes increasingly difficult to form even larger vacancy clusters like V_{14}, because the probability of agglomeration decreases with the size of the cluster and V_{11} can easily dissociate into V_{10} and a mono-vacancy.

7.6 The simple and the extended bond-counting model

In this Section the details of the simple and the extended bond-counting model are outlined by discussing the change of the bond pattern during the creation of vacancies. In the simple bond-counting model, where relaxation is not taken into account, the cohesive energy of the system corresponds to the number of bonds times the energy per bond E_{b}. The ideal crystal with N atoms in the super-cell has an energy of $E_{\mathrm{cryst}}^{N} = 2\,N\,E_{\mathrm{b}}$. Whereas a n-vacancy cluster with n_{b} broken bonds has an energy of $E_{\mathrm{vac}}^{n} = (2\,N - n_{\mathrm{b}})\,E_{\mathrm{b}}$. Therefore, one obtains for the formation energy

$$E_n^{\mathrm{F}} = E_{\mathrm{vac}}^{n} - \frac{N-n}{N} E_{\mathrm{cryst}}^{N} = (2n - n_{\mathrm{b}})\,E_{\mathrm{b}} \quad . \tag{7.7}$$

For the mono-vacancy the number of broken bonds n_{b} equals four. In the simple di-vacancy this number equals seven. Removing further atoms on a nearest neighbor site breaks three additional bonds each time as long as the "vacancy-chain" remains open. The number n_{b} increases less rapidly if the removal of a further atom leads to a "vacancy-ring". The smallest possible ring consists of six vacancies. Closing the ring changes n_{b} from 16 for V_5 to 18 for V_6 (see Fig 7.3 (a)). Adding a vacancy close to the ring breaks three additional bonds until a second ring is closed. Looking at Figure 7.1 one notices that for V_9, where the atoms 1 to 9 are removed, a second vacancy-ring is closed. A third vacancy-ring is closed for V_{10} created from V_9 by removing atom number 10. The number of broken bonds increases only by two, if one goes from V_8 to V_9 and from V_9 to V_{10} (see Tab 7.1).

A straight forward extension of this simple model includes the energy gained by the formation of n_{n} newly formed bonds. As described above, the four atoms surrounding the mono-vacancy approach each other during the relaxation such that two short distances of 2.8 Å and four slightly larger distances of 3.0 Å occur between the four atoms. Only the short bonds (less or equal 2.8 Å) are counted as bonds. Therefore, for V_1 it is $n_{\mathrm{n}} = 2$ in this extended bond-counting model. The simple di-vacancy is characterized by the formation of two bonds in each of the two isosceles triangles described above. A total of four new bonds is formed. The di-vacancy can be considered as a chain of two vacancies, it follows that at each end of a vacancy-chain two new bonds are built. The vacancy sites which are not at the end of the chain have at two of the four nearest neighbor sites another vacancy and at the other two sites there are two atoms from the surrounding crystal. These latter two atoms built one new bond per vacancy. The tri-vacancy exhibits 5 new bonds and an open non-branching chain of n vacancies exhibits $2 + n$ new bonds. As in the simple bond-counting model this dependency changes if the vacancies form a closed ring. All vacancy sites in a single closed ring have a neighborhood identical to the sites in the center of a vacancy-chain. Hence, a single ring of n vacancies exhibits n new bonds. Examples of a single ring are the hexagonal ring V_6 (atoms 1-6 in Fig. 7.1 removed) (Figure 7.3 and Table 7.1) and V_8 (atoms 1,2,4-6,8-10 in Fig. 7.1 removed) (Table 7.2).

If the vacancies form a network of sixfold rings which share some vacancy sites such as the vacancy structures V_{10} displayed in Fig 7.4 (a) or V_{14} displayed in Fig 7.6 (a), the number of new bonds is fixed at $n_{\mathrm{n}} = 6$. This is because these structures introduce vacancy sites, which have at three of their nearest neighbor sites vacancies, and the atoms in the surrounding crystal sitting on the fourth nearest neighbor site cannot form a new bond to a next-nearest neighbor. The ring-vacancy V_{10} has four of such vacancy sites with three nearest neighbor vacancy sites and the ring-vacancy V_{14} has eight of them. Adding a vacancy next to V_6, V_{10}, or V_{14} (as defined by Figure 7.1) breaks one of the formerly formed bonds and creates one new bond. Therefore, the number of new bonds equals six for V_6, V_7, V_{10}, V_{11}, V_{14}, and V_{15}.

Chapter 8

Conclusion

8.1 Summary

In this thesis the growth pattern of silicon clusters and of vacancy clusters in bulk silicon has been investigated. The stability of the silicon structures of interest has been determined by calculating their cohesive and/or formation energies. To allow for a comparison with experimental data physical properties accessible by experiment have additionally been calculated. Many physical properties, such as IR and Raman spectra, polarizabilities, "mobilities",and HOMO-LUMO gaps for clusters and positron lifetimes for vacancy clusters, and their variation with system size have been derived from the ground-state geometries. The combined information from theory and experiment yields valuable insights to the structures and bonding patterns of these systems.

The density-functional based tight-binding (DFTB) method has been adopted to silicon systems. Geometries, energies, and vibrational frequencies of various silicon systems from clusters to solids can be calculated within DFTB nearly as accurate as with other sophisticated more time-consuming methods. The efficiency of DFTB makes it possible to perform molecular dynamics with clusters and to treat extended vacancy clusters embedded in large super-cells.

New candidates for the ground-state structure of Si_9, Si_{13}, and Si_{14} have been identified. The tri-capped trigonal prism forms a basic building block for the low-energy clusters with 10 to 14 atoms. The vibrational density of states (VDOS) for the groundstate geometries, along with infrared and Raman spectra, have been calculated within the scf-DFT-LDA. The calculations predict low IR intensities for Si_9, Si_{12}, Si_{13}, and Si_{14}. This raises questions whether it is possible to detect the IR spectra by experiment. The calculations indicate instead that Raman measurements are more suitable to identify the ground-state geometries for these cluster sizes. In contrast, theory suggests that IR measurements are most appropriate to determine whether the TTP or TCO configuration of Si_{10} corresponds to the groundstate. This is due to the similarity of the Raman spectra for both isomers and to a strong IR peak of the TCO configuration absent in the TTP configuration.

A discrepancy remains between polarizabilities determined by theory and experiment. The variation of the polarizability as a function of cluster size is much stronger for measured than for theoretical data. Additional measurements are required to resolve this issue.

A shape transition at cluster sizes around Si_{25}, previously indicated by mobility measurements on silicon cluster anions and cations, has been confirmed theoretically for neutral clusters. The Simulated Annealing optimization technique has been proven to be a reliable and efficient tool to find low-energy structures. The technique has been successfully applied in cases where the energy-potential exhibits a vast number of local minima. For neutral Si_{25} clusters almost spherical and prolate structures coexist. For Si_{29} most of the low-energy isomers have a more spherical shape and for Si_{35} the low-energy isomers are solely compact and spherical. For silicon clusters with about 20 to 25 atoms it is energetically more favorable to bind two stable smaller isomers with about 10 atoms either directly or via an intermediate small fragment. For larger clusters (with more than 25 atoms) compact spherical structures with some five- or sixfold coordinated atoms are lower in energy compared to clusters built from smaller fragments. The electronic structure close to the Fermi level is different for prolate and spherical compact clusters. Hence, stable isomers of, e.g., Si_{25} with different chemical reactivities and optical properties exist.

All silicon clusters with up to 35 atoms exhibit a bonding pattern strikingly different from the tetrahedral bonding pattern in the diamond structure. For these cluster sizes almost all atoms are close to the surface. For larger clusters such as Si_{71} and Si_{239} the Simulated Annealing reveals compact structures with a bonding pattern which still is quite different from tetrahedral bonding. Most likely a diamond-like core with mainly sp^3-hybridized atoms foremost becomes energetically competitive to a disordered core with various coordination numbers for nanoparticles with several hundred to several thousand atoms.

Within SCC-DFTB the cohesive energy of the clusters increases from $-3.82\,\mathrm{eV/atom}$ for Si_{10} to $-4.24\,\mathrm{eV/atom}$ for Si_{239}. Clusters as large as Si_{239} have only 88% of the cohesive energy of bulk silicon ($-4.80\,\mathrm{eV/atom}$). Compared to the carbon fullerene C_{60}, where the cohesive energy corresponds to about 95% of the cohesive energy of diamond, it appears to be less likely that stable cluster assembled materials can be built from pure silicon clusters. However, it has been shown that the stability of cage-like silicon structures can be increased by substitution of some silicon atoms by nitrogen [128] or by addition of endohedral atoms such as zirconium [129]. It follows that silicon based cluster assembled materials are conceivable with a certain amount of impurities which act as either charge donator or acceptors and locally change the electron occupation.

For vacancy clusters in bulk silicon especially stable structures with a "magic number" of vacancies have been determined. The SCC-DFTB calculations find vacancy clusters with 6, 9, and 10 vacancies (V_6, V_9, and V_{10}) where the vacancies form closed hexagonal rings to be particularly stable systems. The high stability is obviously due to the minimum number of dangling bonds in these structures. The SCC-DFTB results are consistent with results from other calculations based on alternative methods. The agreement of the calculated positron lifetimes for V_9 and V_{10} with the results from positron annihilation spectroscopy indicate that V_9 and V_{10}

are present in neutron or electron irradiated silicon. The annealing-temperatures at which the measured lifetime components vanish are in agreement with the calculated dissociation energies of the corresponding vacancy clusters. For clusters with up to 14 vacancies the most stable configurations of each cluster size correspond to fragments from a hexagonal ring-network. The extended bond-counting model correctly describes the variation of the formation energies with cluster size for these vacancy configurations. For an accurate description of the energy differences between vacancy clusters of equal size and of larger vacancy agglomerations explicit calculations with quantum mechanical methods are indispensable. The SCC-DFTB calculations indicate compact vacancy clusters, different from the hexagonal ring structures, to be more stable for larger vacancy agglomerations.

8.2 Outlook

Many important insights in the growth-process of silicon clusters and of vacancy clusters in bulk silicon could be gained. Based on these insights new questions for future research projects arise. The SCC-DFTB method is focused on the determination of ground-state geometries, cohesive energies and molecular dynamics. The optical properties and chemical reactivities of the established ground-state structures need to be further characterized. Since many measurements are performed on charged clusters, it is desirable to apply SCC-DFTB to silicon cluster anions and cations, as well. Impurities like oxygen, nitrogen, or hydrogen are often present during cluster-growth and it will be very useful to investigate the influence on the stability and physical properties of such impurities. Germanium is another important material in the semiconductor industry. In many aspects germanium is similar to silicon. How much the larger covalent radius and the presence of occupied d-states change the results found for silicon systems has only partly been adressed, so far. The increasing performance of parallel computers will make it possible to study nanoparticles with several hundred atoms, e.g, nanowires, which are part of nanoscale devices. Also, molecular dynamics with large silicon clusters, with some hundreds of atoms in a heat bath should be possible.

The charge-state plays an important role for defects, as well. However, taking into account local charges in periodic systems and spinpolarization in the tight-binding framework, still has to be implemented. The trapping of impurities into vacancy clusters is important for the conduction process in semiconductors. For vacancy clusters, especially in silicon, a large number of experimental data is available from electron paramagnetic resonance experiments. Some of the paramagnetic centers, like the P1-center [92], have not yet been identified. The DFTB calculations rule out the negatively charged penta-vacancy geometry suggested in [92]. The calculated charge distribution of the highest occupied molecular orbital (HOMO) for this geometry deviates substantially from the charge distribution assumed in reference [92]. Additional DFTB calculations pointed towards an accurate description of the electronic structure can aid in the identification of the defect responsible for the P1-center.

Appendix A

Calculation of the overlap- and Hamilton-matrix elements

A.1 Contraction of the density and the wave-functions

Within DFTB the two-center overlap- and Hamilton integrals are calculated from a two-center potential and from basis-functions derived from a single atom calculation with the additional radial-symmetric potential (see Chapter 2 and [13, 16, 130])

$$V_{\mathrm{ad}}(r) = \left(\frac{r}{r_0}\right)^n, \quad n = 2.$$

This avoids the drawback of long-ranged basis-functions in solid systems and takes into account that for many systems the density can be better approximated by a superposition of contracted single atom densities.

The optimum values for r_0 can be different for the calculation of the density, used to form the two atom potential, and for the calculation of the basis functions. In the first case r_0 is denoted r_d (for r_{dens}) and in the second case r_0 is denoted r_w (for r_{wave}).

To find the best contraction radii r_d and r_w the variational principle could be applied to a given system, but this appears to result in different values for solids and molecular systems. A semi-empirical adjustment of the contraction radii until physical properties like geometries or energies agree within DFTB and scf-DFT is impeded by the fact that in most systems such physical properties depend on the repulsive potential, which in turn depends on the contracted density. Since the repulsive potential is cut-off at a finite distance, the energy of a system with bond-lengths longer than this cut-off are determined solely by the band-structure energy $E_{\mathrm{BS}} = \sum_i^{\mathrm{occ}} \varepsilon_i$. The band-structure energy depends only on the Hamilton- and overlap-matrix and, therefore, on the parameters r_d, r_w, and the power n. The latter has been fixed to $n = 2$ according to previous studies [16]. Various comparisons between scf-DFT calculations and approximative calculations with contracted basis functions show that the optimum contraction radius r_w is in the range from 1.5 to 2.5 times the covalent radius of the considered atom type. The relevant values for silicon are: $1.6\,\mathrm{Å}(3.0\,a_{\mathrm{B}}) < r_w < 2.8\,\mathrm{Å}(5.2\,a_{\mathrm{B}})$.

In this work the contraction radius r_d for the atomic density and the contraction radius r_w for the atomic-wavefunctions have been determined via a variational principle from the band-structure energies of the diamond and of the simple cubic (sc) phase. In the diamond structure the silicon atoms are fourfold coordinated with a nearest neighbor distance of 2.35 Å and a bond angle of 109°. The atoms in the simple cubic structure are sixfold coordinated with a nearest neighbor distance of 2.54 Å and a bond angle of 90°. It is assumed that describing these two different phases accurately results in a transferable tight-binding parametrization for systems with coordination numbers not greater than six.

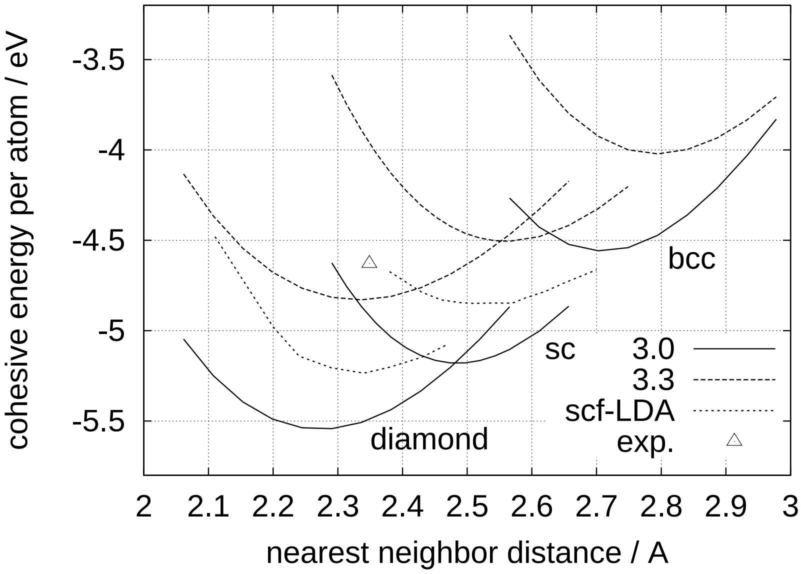

Figure A.1: Band-structure energy of several bulk phases for two different wavefunction parameters r_w/a_B. The parameter for the density is $r_d = 6.7\,a_B$. The cohesive energies as calculated with scf-LDA for the diamond and simple cubic phase and the experimental value for the diamond phase are given for comparison.

Figure A.1 shows the DFTB band-structure energy E_{BS} for the diamond, simple cubic (sc), and the body centered cubic (bcc) phase for two differently contracted wavefunctions. The experimental cohesive energy of $-4.63\,\mathrm{eV}$ [131] for diamond is marked for comparison and the cohesive energy curves for the diamond and sc phase as calculated within all-electron scf-LDA (*NRLMOL*) are shown, too. Compared to the experimental value the scf-LDA calculation shows an over-binding of 0.6 eV. The DFTB band-structure energies obtained with the stronger contraction ($r_w = 3.0\,a_{\mathrm{B}}$) are lower than with a weaker contraction ($r_w = 3.3\,a_{\mathrm{B}}$) for all phases. Figure A.2 shows the DFTB band-structure energies for the same phases for two differently contracted densities. Here, the effect of the contraction is the opposite: The DFTB band-structure energies obtained with the weaker contraction ($r_d = 7.7\,a_{\mathrm{B}}$) are lower.

For the silicon-silicon parametrization finally the parameter combination $r_d = 6.7\,a_B$ and $r_w = 3.30\,a_B$ has been found to be most appropriate. With these two parameters

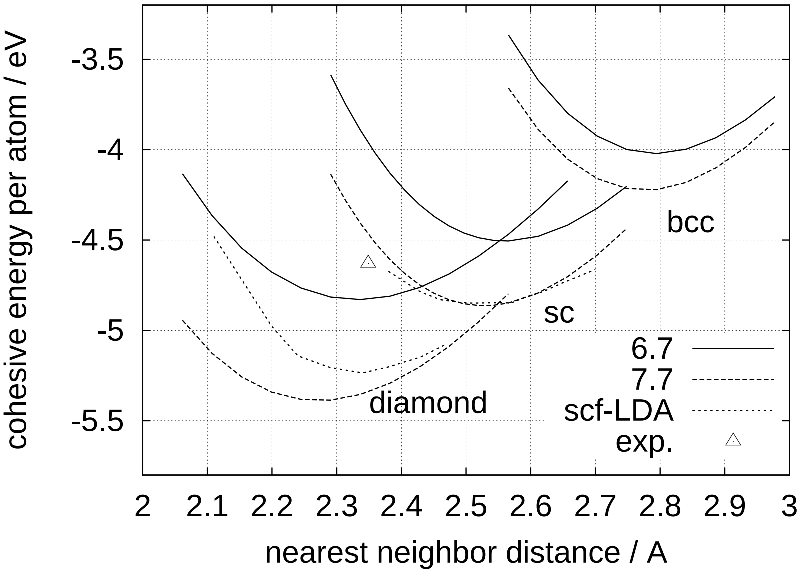

Figure A.2: Band-structure energy of several bulk phases for two different density parameters r_d/a_B. The parameter for the wave-functions is $r_w = 3.30\,a_B$. The scf-LDA and experimental data are given for comparison.

the minimum of the band-structure energy of the diamond phase lies in between the experimental value and the scf-LDA value. The difference in the band-structure energies (i.e., without the repulsive potential) between the diamond and the simple cubic phase is about 0.4 eV close to the difference in the total cohesive energy as calculated within scf-LDA (0.35 eV in Ref. [131] and 0.39 eV with *NRLMOL*).

If one compares the DFTB band-structure energy of diamond obtained with the parameters $r_d = 6.7\,a_\mathrm{B}$ and $r_w = 3.3\,a_\mathrm{B}$ with the cohesive energy as parameterized by the Murnaghan equation of state

$$E_\mathrm{tot}(V) = \frac{B_0 V}{B_0'}\left[\frac{(V_0/V)^{B_0'}}{B_0'-1} + 1\right] + \mathrm{const},$$

one notices that the dependence upon V for both methods is almost identical for nearest neighbor distances larger than the equilibrium distance (see Fig. A.3). Here, the bulk modulus B_0 and its pressure derivative B_0' at the equilibrium volume V_0 have been set to the experimental values reported in [131]. A repulsive potential with a cut-off radius of 2.54 Å has been chosen for the calculation of total energies. Fitting the energy difference $E_\mathrm{BS}^\mathrm{TB} - E_\mathrm{coh}^\mathrm{scf}$ per bond to the polynomial

$$V(r) = \sum_{i=3}^{7} a_i (r_c - r)^i, \quad r_c = 4.8\,a_\mathrm{B},$$

yields in atomic units (Hartree and Bohr) the coefficients

$$\begin{aligned} a_3 &= 0.0155855, & a_4 &= -0.0128669, & a_5 &= 0.0254527, \\ a_6 &= -0.0146618, & a_7 &= 0.00263252. \end{aligned}$$

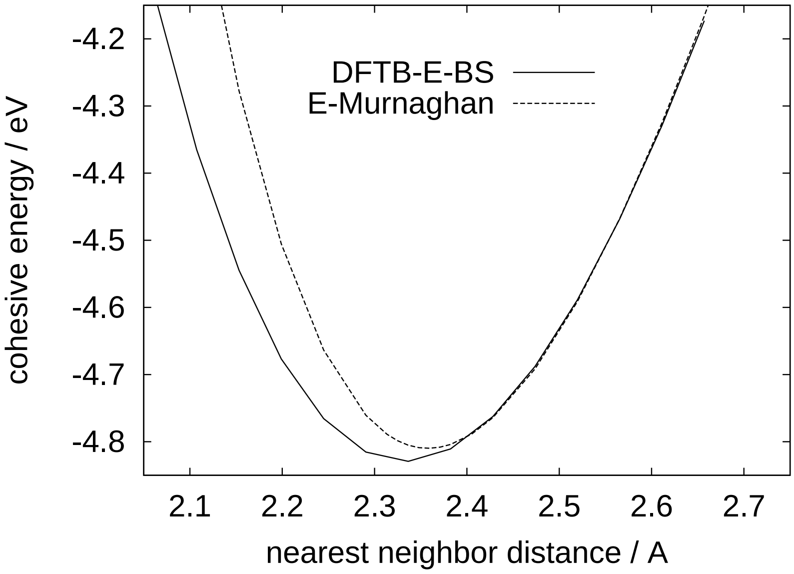

Figure A.3: DFTB band-structure energy with $r_d = 6.7\,a_B$ and $r_w = 3.30\,a_B$ and cohesive energy parameterized by the Murnaghan equation with parameters $E_0 = -4.82\,\mathrm{eV}$, $a_0 = 5.42\,\text{Å}$, $B_0 = 0.99\,\mathrm{Mbar}$ and $B_0' = 4.2$.

Figure A.4 shows this polynomial along with the energy difference $V_{\mathrm{rep}} = (E_{\mathrm{TB}} - E^{\mathrm{scf}}_{\mathrm{coh}})$ per bond for two different systems, the diamond phase ($E^{\mathrm{scf}}_{\mathrm{coh}}$ obtained with the Murnaghan equation of state) and the Si$_5$ cluster with T_d-symmetry. For Si$_5[T_d]$ V_{rep} is shifted to be zero at $r = 2.5\,\text{Å}$. The slope of V_{rep} is slightly different for the two systems. This is due to the fact that the double-counting and coulomb terms forming V_{rep} cannot exactly be represented by a simple two-pair interaction. However, the polynomial given above is a reasonable approximation to V_{rep} for interatomic distances larger than 2.2 Å and, therefore, for most silicon systems.

The cohesive energies for several silicon bulk phases obtained with the matrix-elements and the repulsive potential calculated in the way represented above are displayed in Fig. A.5. The corresponding (minimum) cohesive energies as obtained with a plane-wave pseudopotential code [131] are $-4.84\,\mathrm{eV}$ (diam), $-4.49\,\mathrm{eV}$ (sc), $-4.57\,\mathrm{eV}$ (β-tin), $-4.31\,\mathrm{eV}$ (bcc) and $-4.27\,\mathrm{eV}$ (fcc). The cohesive energies obtained with the all-electron scf DFT-LDA code *NRLMOL* are $-5.24\,\mathrm{eV}$ (diam) and $-4.85\,\mathrm{eV}$ (sc).

The bulk-modul and other second order elastic constants for the diamond phase are compared between DFTB and experimental data in Table A.1. The deviations are less than 7% which is a good agreement for second order derivatives.

The two-center overlap and Hamilton matrix elements depend only on the internuclear distance. For a given system the matrix elements have to be transformed with respect to the orientation of the atom-pairs. The transformation has been described by Slater and Koster [133] and the matrix-elements are refered to as *Slater-Koster parameters*. The two-center overlap and Hamilton matrix elements

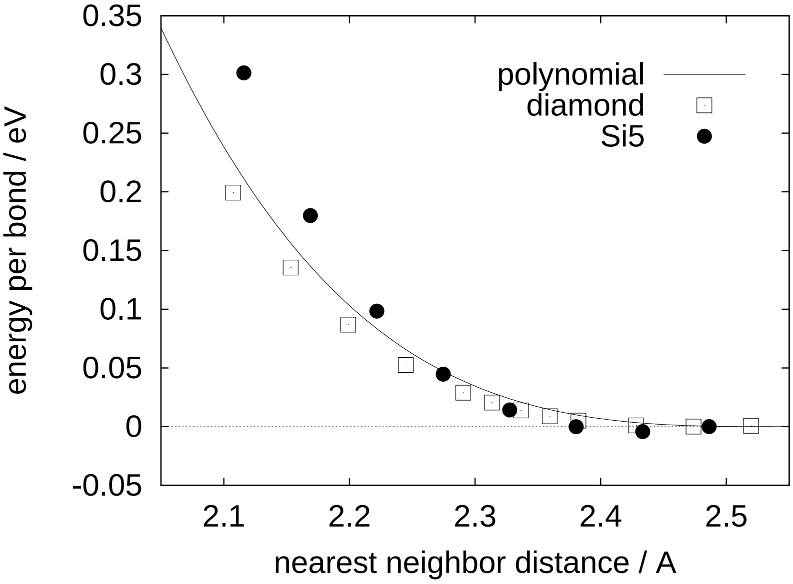

Figure A.4: Polynomial used for the repulsive potential. Additionally the energy difference between the cohesive energy and the TB band-structure energy is given for the diamond bulk (Murnaghan equation) and Si_5 [T_d] (scf-GGA).

Method	B_0	c_{11}	c_{12}	c_{14}
DFTB	92	151	63	74
Experiment	99	166	64	80

Table A.1: Bulk-modul and second order elastic moduli (in GPa) for silicon as calculated within DFTB and obtained from experiment [132].

as a function of the inter-nuclear distance are depicted in Fig. A.6. At a distance of 4 Å the Hamilton matrix elements are dropped below 5.5% of their maximum values, i.e., the DFTB interaction becomes negligibly small for Si–Si distances longer than 4 Å. In the silicon diamond phase this corresponds to an interaction up to second nearest neighbors.

The DFTB parametrization described in this Section has been applied to the larger silicon clusters with more than 20 atoms described in Chapter 6 and to the vacancy clusters described in Chapter 7. The SCC extension to DFTB has been used for calculating the cohesive energies of these systems. For the smaller silicon clusters described in Chapter 4 an older parametrization similar to the one described in [19] has been used with standard DFTB[1]. The old parametrization was based on DFT-LDA and shows an overbinding typical for LDA. The repulsive potential of the old parametrization described in [19] has been improved to yield more accurate higher frequency vibrational modes. The adjusted coefficients for V_{rep} in the old

---

[1] The SCC extension to DFTB has not been develloped at the time of the calculations.

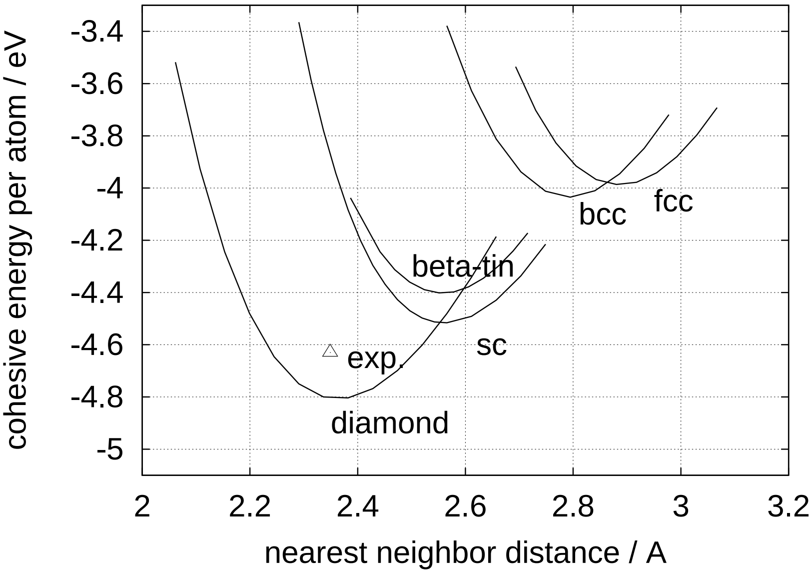

Figure A.5: Cohesive energy of several bulk phases as calculated with DFTB.

parametrization are:

$$a_3 = \ 0.0641068, \quad a_4 = -0.0777954, \quad a_5 = \ 0.0443406,$$
$$a_6 = -0.00767154, \quad a_7 = \ 0.0, \quad r_c = 5.2.$$

All coefficients are in atomic units (Hartree and Bohr).

To allow for a comparison between the energies of the larger and the smaller clusters the cohesive energies for the smaller clusters obtained with both parametrizations are given in Table A.2. The main difference between the two parametrizations is a shift of the cohesive energies by $-0.45\,\mathrm{eV/atom}$ on average.

cluster	E_{coh} (old DFTB) eV/atom	E_{coh} (new SCC-DFTB) eV/atom	ΔE eV/atom
Si_2	-1.94	-1.49	-0.46
Si_3	-2.98	-2.48	-0.50
Si_4	-3.49	-3.01	-0.48
Si_5	-3.77	-3.33	-0.44
Si_6	-3.93	-3.53	-0.40
Si_7	-4.06	-3.65	-0.41
Si_8	-4.07	-3.63	-0.44

Table A.2: Cohesive energies for the most stable isomers of Si_2 to Si_8 obtained with the old DFTB parametrization based on LDA and the new parametrization described in this Section and using SCC-DFTB.

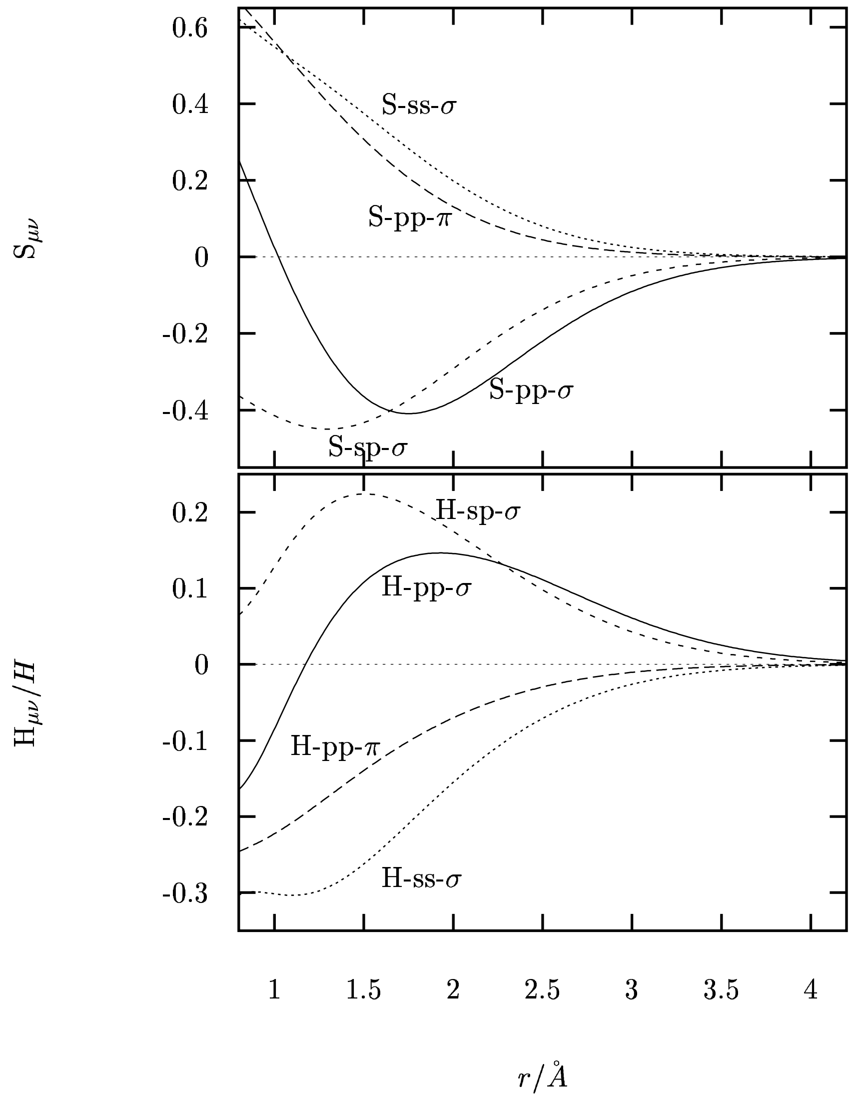

Figure A.6: Overlap and Hamilton matrix-elements as a function of internuclear distance r obtained with DFTB parameters $r_d = 6.7\,a_{\mathrm{B}}$ and $r_w = 3.3\,a_{\mathrm{B}}$.

The differences between the first order DFTB method without consideration of the charge transfer and the SCC-DFTB method with a self-consistent charge transfer are small for homo-nuclear silicon systems. The main influence of the SCC extension in these systems is the reduction of the charge transfer between differently coordinated silicon atoms. Table A.3 shows the cohesive energies and the net-charge on the most negative atom for Si_{10}(TCO) and Si_{10}(TTP) obtained with DFTB and with SCC-DFTB. The atomic charges have been determined with the Mulliken analysis used within the SCC-scheme. Of course the SCC-DFTB and standard DFTB methods are identical when applied to homo-nuclear bulk phases where all atoms have zero net-charge due to the symmetry of the system.

cluster	E_{coh} (DFTB) eV/atom	E_{coh} (SCC-DFTB) eV/atom	$\Delta\rho$ (DFTB) e	$\Delta\rho$ (SCC-DFTB) e
Si_{10}(TCO)	-3.713	-3.709	0.09	0.05
Si_{10}(TTP)	-3.831	-3.825	0.10	0.05

Table A.3: Cohesive energies and net-charges $\Delta\rho$ on the most-negative atom for the two most stable isomers of Si_{10} obtained with DFTB and with SCC-DFTB using the parametrization described in this Section.

A.2 Improving the description of the electronic structure

The DFTB parametrization described in the previous section yields a good description of cohesive energies, forces, and geometries for the diamond, beta-tin, and simple cubic phases and for silicon clusters. These structures typically contain silicon atoms with a coordination number less than or equal to 6. The electronic band-structure for periodic systems and the eigenvalues of the single electron states in finite systems are in good agreement with scf-GGA as well. However, the description of the electronic structure can be improved by optimizing the contraction radii r_d and r_w by solely focusing on the Kohn-Sham eigenvalues. Unfortunately the resulting pair of parameters is not appropriate for calculating accurate cohesive energies.

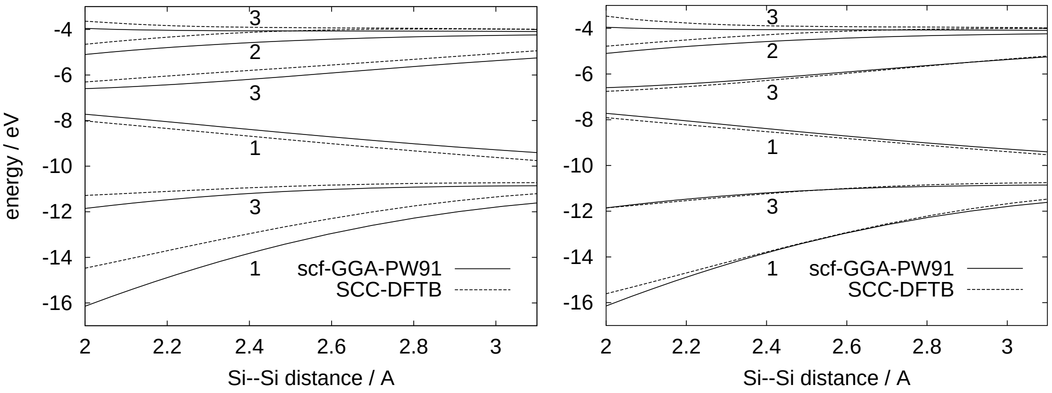

Figure A.7: Eigenvalues ε_i of $\text{Si}_5[\text{T}_d]$ as a function of nearest neighbor distance r. Solid lines correspond to scf-GGA and dashed lines to DFTB. (Left) DFTB parameters $r_d = 6.7\,a_B$ and $r_w = 3.30\,a_B$. (Right) DFTB parameters $r_d = \infty$ and $r_w = 4.50\,a_B$. All eigenvalues up to the lowest unoccupied molecular orbital (LUMO) are shown along with their degeneracy.

Figure A.7 shows the variation of the eigenvalues up to the lowest unoccupied molecular orbital (LUMO) level as a function of interatomic distance for the Si_5 cluster with T_d-symmetry (1 silicon atom in the center and 4 silicon atoms in the opposite corners of a cube). With the DFTB parameters $r_d = 6.7\,a_{\text{B}}$ and $r_w = 3.3\,a_{\text{B}}$ the lowest eigenvalue of the valence states lies about 1 eV above the corresponding scf

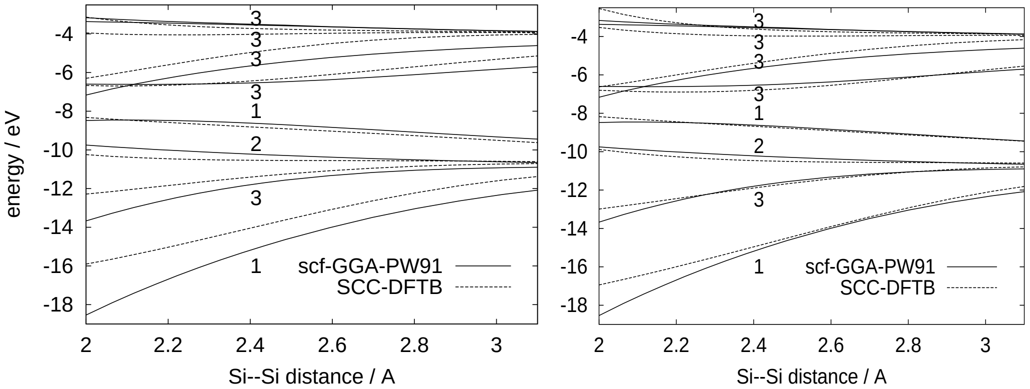

Figure A.8: Eigenvalues ε_i of $Si_7[O_h]$ as a function of nearest neighbor distance r. (Left) DFTB parameters $r_d = 6.7\,a_B$ and $r_w = 3.30\,a_B$. (Right) DFTB parameters $r_d = \infty$ and $r_w = 4.50\,a_B$.

DFT-GGA value obtained with *NRLMOL* at the equilibrium distance $r = 2.2\,\text{Å}$. The deviation of the eigenvalues of the other occupied states are smaller than 0.5 eV at this distance. If one sets the parameters to $r_d = \infty$ (no contraction for calculating the two-center potential) and $r_w = 4.5\,a_\mathrm{B}$ the agreement with the scf DFT-GGA eigenvalues is almost perfect in the range $2.2\,\text{Å} \leq r \leq 3.0\,\text{Å}$. Only the eigenvalues of the HOMO and LUMO are slightly too high within SCC-DFTB. The same settings also improve the SCC-DFTB eigenvalues for the $Si_7[O_h]$ cluster (one silicon atom in the center and six silicon atoms on the Cartesian axes in opposite directions) as can be seen in Fig. A.8. For the electronic structure this indicates the transferability of these DFTB parameters between quite different bonding schemes. However, the parameters $r_d = \infty$ and $r_w = 4.5\,a_\mathrm{B}$ shift the bandstructure energies of the diamond and sc phases towards more negative energies compared to the energies obtained with the parameters $r_d = 6.7\,a_\mathrm{B}$ and $r_w = 3.3\,a_\mathrm{B}$ (see Fig. A.9). To obtain total energies in agreement with experiment or DFT-GGA calculations a quite long-ranged repulsive potential would be required. This would result in too high energies for the higher coordinated bulk phases. Therefore, the parameters $r_d = 6.7\,a_\mathrm{B}$ and $r_w = 3.3\,a_\mathrm{B}$ have been chosen as the best compromise between accurate cohesive energies and a good description of the electronic structure.

The measured k-dependent band-structure of the silicon diamond crystal features a maximum bandwidth at Γ of about 12.5 eV [134], an indirect gap from Γ to $0.85X$ of 1.17 eV [135], and a direct gap at Γ of about 2.7 eV [136]. Since the density-functional formalism is a single-particle theory which focuses on ground-state properties, the calculated eigenvalues do not correspond directly to elementary excitations (see Chapter 2). To obtain eigenvalues directly comparable to experimental excitation spectra density-functional theory can be extended, e.g., to take self-interaction corrections (SIC) into account. In general, within standard scf DFT the gaps of insulators and semiconductors are underestimated. Because of the usage of a minimum basis set, this can be different in tight-binding methods. Within SCC-DFTB with a minimum basis set (s- and p-atomic-orbitals) the gap in the silicon diamond crystal

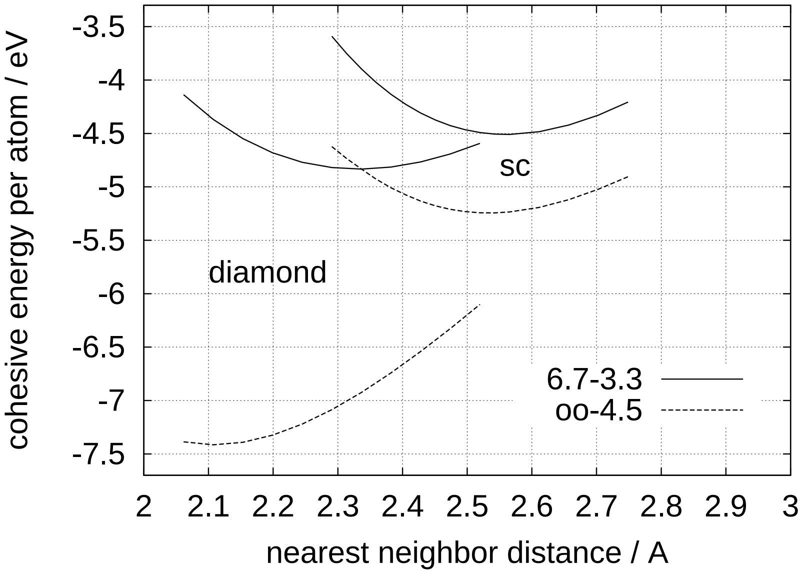

Figure A.9: Band-structure energies of the diamond and simple cubic phases for the two different parameter pairs ($r_d = 6.7\,a_\mathrm{B}$, $r_w = 3.3\,a_\mathrm{B}$) and ($r_d = \infty$, $r_w = 4.5\,a_\mathrm{B}$).

is direct and the lower conduction band at $0.85X$ lies much too high. However, the agreement of the lower conduction bands with scf DFT-GGA calculations can be improved by the usage of an extended basis set.

With the DFTB parameters $r_d = 6.7\,a_\mathrm{B}$ and $r_w = 3.3\,a_\mathrm{B}$ the overall variation of the valence bands with the momentum k is described correctly. The valence band widths of 10.5 eV is too small compared to experiment and scf DFT-GGA and the two lowest valence bands slightly deviate at the L-point of the Brilouin-zone (BZ) compared to scf DFT-GGA (see Fig. A.10). The electronic density of states obtained with $r_d = 6.7\,a_\mathrm{B}$ and $r_w = 3.3\,a_\mathrm{B}$ is given in Fig. A.13. The peaks relative to the valence band maximum agree quite well with the positions in measured angle-integrated photo-emission spectra [134].

As expected from the improvement of the eigenvalues for the clusters $\mathrm{Si}_5[T_d]$ and $\mathrm{Si}_7[O_h]$ mentioned above the valence bands for the silicon diamond crystal are also improved by using the DFTB parameters $r_d = \infty$ and $r_w = 4.5\,a_\mathrm{B}$ (see Fig. A.11). The DFTB eigenvalues match almost exactly the points obtained with an scf pseudo-potential plane-wave code [131] at the high-symmetry $\vec{k}$-points L, Γ (G) and X of the BZ. Figure A.12 illustrates that a correct electronic band-structure including the lower conduction band and featuring an indirect gap can be obtained with an extended basis set. This basis set consists of one 3s, three orthogonal 3p, five orthogonal 3d, and one 4s basis functions.

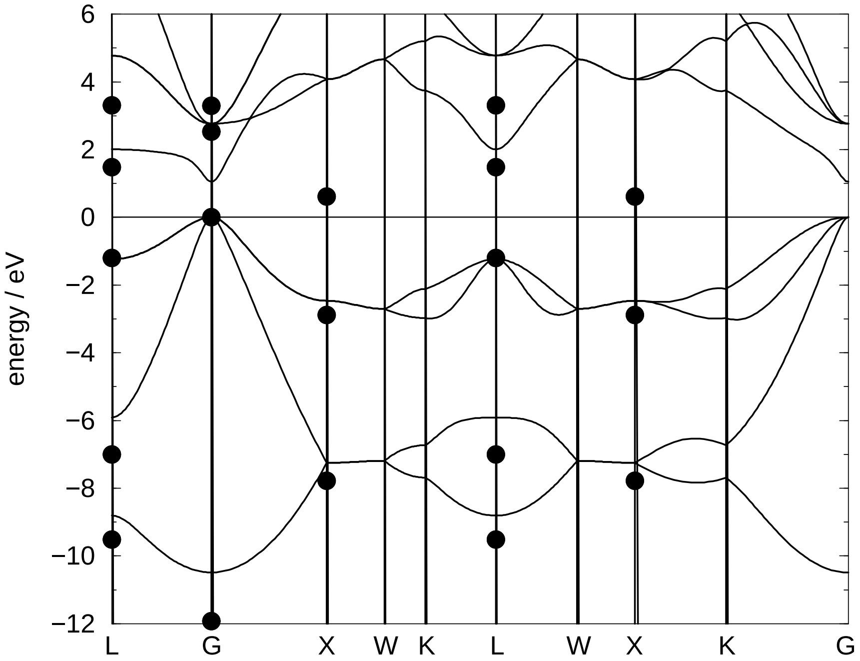

Figure A.10: Silicon band-structure (diamond phase) as calculated with DFTB parameters $r_d = 6.7\,a_B$ and $r_w = 3.30\,a_B$. The dots denote special levels calculated with a scf pseudopotential plane-wave code based on LDA [131].

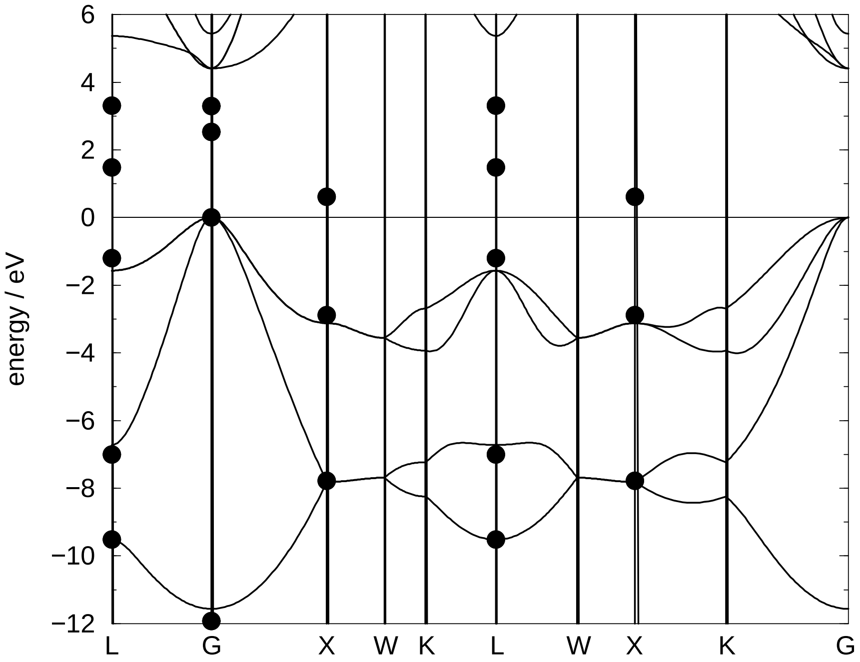

Figure A.11: Silicon band-structure (diamond phase) as calculated with DFTB parameters $r_d = \infty$ and $r_w = 4.50\,a_B$. The dots denote special levels calculated with a scf pseudopotential plane-wave code based on LDA [131].

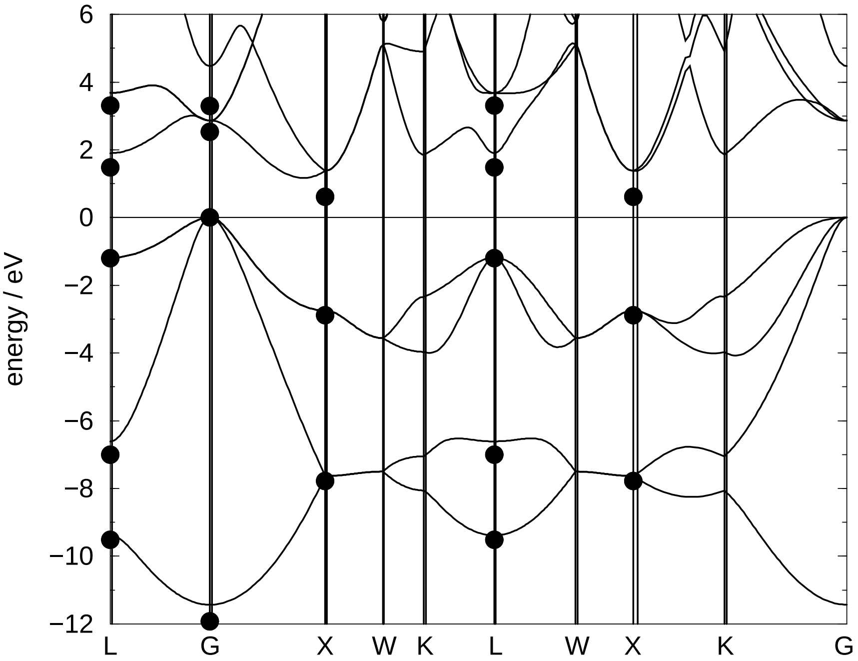

Figure A.12: Silicon band-structure (diamond phase) as calculated with an extended (3s3p3d4s) DFTB basis set. Parameters $r_d = 5.4\,a_B$, $r_w = 5.4\,a_B$, and $n = 4$. On-site energies of non-occupied atomic levels $E_{4s} = 0.18\,\text{H}$, $E_{3d} = 0.2\,\text{H}$. The dots denote special levels calculated with a scf pseudopotential plane-wave code based on LDA [131].

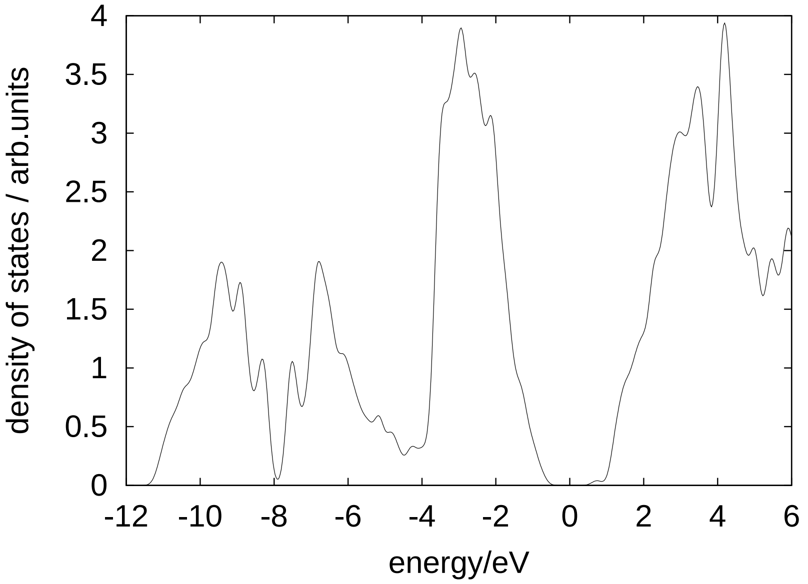

Figure A.13: Density of states for the silicon diamond phase as calculated with minimum basis set and DFTB parameters $r_d = 6.7\,a_{\text{B}}$ and $r_w = 3.3\,a_{\text{B}}$.

Appendix B

Short Summary of Group Theory

Some important features of the electronic and vibrational states of a molecule or cluster can be reclusively predicted by its symmetry. With the aid of group theory the number of electronic states and of vibrational frequencies along with the corresponding degree of degeneracy can be determined. Furthermore, the selection rules for transitions between different states, e.g., if a certain vibrational mode is IR or Raman active, directly follow from the symmetry of the structure. In this Appendix the nomenclature of group theory is introduced and the application of the selection rules for IR and Raman transitions is described. A more detailed description of group theory and its applications can be found, e.g., in [137].

B.1 Basic Group Theory

The symmetry of a structure is defined by all the geometrical operations, which transform the structure to a new, physically non distinguishable, structure. For finite structures these operations must keep at least one point, the center of mass, fixed. The possible symmetry operations can be divided into five classes: identity (E), rotation (C), reflection (σ), rotation-reflection (S), and inversion (i). For finite systems all possible symmetry operations of a given symmetry form a point group. The number of these operations determines the order of the group and is denoted by g. A group is defined as a set of abstract elements on which a combining operation (product) is defined for which the following four rules must be fulfilled:

1. The "product" or combination of any two elements of the group must be also a member of the group.

2. The group must contain the identity element denoted by E. The identity element is defined by $ER = RE = R$ for all elements R.

3. The combining operation must be associative, i.e. $R(ST) = (RS)T$ for all elements R, S, T of the group.

4. Every element R must have an inverse element R^{-1}, which must also be an element of the group. The inverse element is defined by $RR^{-1} = R^{-1}R = E$.

For all geometrical symmetry operations the combining operation simply means the successive application of two transformations.

There exist two widely used but different systems of notation for point groups: the international system and the Schönflies system. The Schönflies notation for the most common point groups for clusters are defined in Table B.1.

E	Identity
C_n	Rotation through $2\pi/n$
C_{nv}	C_n plus reflection in a plane containing the axis of highest symmetry
C_{nh}	C_n plus reflection in a plane perpendicular to the axis of highest symmetry
D_n	C_n plus n twofold axes perpendicular to the axis of highest symmetry (in the case of D_2, there are three twofold axes)
D_{nh}	D_n plus a horizontal reflection plane
T	12 proper rotations which carry a regular tetrahedron into itself
T_d	24 symmetry operations of the regular tetrahedron, including improper rotations
O	24 proper rotations which carry a cube into itself
O_h	48 (proper and improper) rotations which carry a cube into itself

Table B.1: Schönflies notation for the most common point groups.

	E	σ'_v	σ''_v	σ'''_v	C_3	C_3^2
E	E	σ'_v	σ''_v	σ'''_v	C_3	C_3^2
σ'_v	σ'_v	E	C_3	C_3^2	σ''_v	σ'''_v
σ''_v	σ''_v	C_3^2	E	C_3	σ'''_v	σ'_v
σ'''_v	σ'''_v	C_3	C_3^2	E	σ'_v	σ''_v
C_3	C_3	σ'''_v	σ'_v	σ''_v	C_3^2	E
C_3^2	C_3^2	σ''_v	σ'''_v	σ'_v	E	C_3

Table B.2: Group table for the C_{3v} point group

For example, a tripod formed by the three corners of an equilateral triangle and an arbitrary point above the center of the triangle is physically unchanged by the identity operation (E) , a rotation at 120° about the rotation-axis (C_3), a rotation at 240° about the rotation-axis (C_3^2) and reflections on one of the three reflection-planes (σ_v). The rotation-axis goes through the center of the equilateral triangle and is perpendicular to the triangle. The three reflection-planes are determined by the rotation-axis and one of the corners of the equilateral triangle. These six operations form a point group denoted by C_{3v} of order $g = 6$. In Table B.2 all possible combinations of two operations are summarized. The column determines the operation carried out first. The group table shows that the first rule for a group is obeyed, every combination yields an element of the group.

The second rule is obeyed because the "do nothing" operation E is included. The third rule can be checked with the aid of the group table, e.g., it is

$$(C_3\sigma_v')C_3^2 = \sigma_v'''C_3^2 = \sigma_v'' = C_3\sigma_v''' = C_3(\sigma_v'C_3^2).$$

Finally every operation has one inverse operation within the group, because each row or column of the table contains exactly one times the identity operation E.

The abstract elements of a group can have many possible representations. For example for a given symmetry both the geometric transformations itself and the matrices describing the transformations are representations for the symmetry group. The corresponding matrices, which describe the transformation of a point (x, y, z) in Cartesian coordinates to a new point (x', y', z'), for the example given above, are:

$$M(E) = \begin{pmatrix} 1 & 0 & 0 \\ 0 & 1 & 0 \\ 0 & 0 & 1 \end{pmatrix} \tag{B.1}$$

$$M(C_3) = \begin{pmatrix} -1/2 & \sqrt{3}/2 & 0 \\ -\sqrt{3}/2 & -1/2 & 0 \\ 0 & 0 & 1 \end{pmatrix} \tag{B.2}$$

$$M(C_3^2) = \begin{pmatrix} -1/2 & -\sqrt{3}/2 & 0 \\ \sqrt{3}/2 & -1/2 & 0 \\ 0 & 0 & 1 \end{pmatrix} \tag{B.3}$$

$$M(\sigma_v') = \begin{pmatrix} -1 & 0 & 0 \\ 0 & 1 & 0 \\ 0 & 0 & 1 \end{pmatrix} \tag{B.4}$$

$$M(\sigma_v'') = \begin{pmatrix} 1/2 & -\sqrt{3}/2 & 0 \\ -\sqrt{3}/2 & -1/2 & 0 \\ 0 & 0 & 1 \end{pmatrix} \tag{B.5}$$

$$M(\sigma_v''') = \begin{pmatrix} 1/2 & \sqrt{3}/2 & 0 \\ -\sqrt{3}/2 & -1/2 & 0 \\ 0 & 0 & 1 \end{pmatrix}. \tag{B.6}$$

These six matrices fulfill all the four requirements to form a group. Here it is assumed that the 3–fold rotation axis coincides with the z-direction and that the σ_v' reflection plane is the y,z-plane. Obviously one obtains a different set of matrices, if a different orientation is chosen and this set is said to be equivalent to the other one. Stated differently, two representations are called equivalent if all the corresponding matrices of one representation are related to the matrices of the other representation by a similarity transformation. Additionally, a set of higher dimensional matrices, which may describe the transformation behavior of five d-type orbitals placed at an arbitrary point (x, y, z), can be used as a valid representation. From all the possible representations only the non-equivalent irreducible representations are important to describe all the features of a given symmetry. A representation is said to be irreducible, if their corresponding matrices cannot be simultaneously broken down (reduced) by a similarity transformation into block form, i.e. into matrices which consist of square matrices on their diagonal and have zero elements elsewhere. The matrices (B.1) - (B.6) are in block-form, this representation can be reduced into one two-dimensional irreducible representation Γ^1 and into one one-dimensional irreducible representation Γ^2. The one-dimensional representation consists of six identical one-dimensional matrices equal to 1, whereas the two-dimensional representation is obtained by removing the last row and last column from the matrices (B.1) - (B.6).

From the matrices $M(R)$ of a given representation one needs to know only the traces $\chi(R) = \sum_i M_{ii}(R)$, the so-called characters, to determine, e.g., the selection rules for transitions between different states. In the example the characters for the two-dimensional irreducible representation Γ^1 are given by

$$\chi_{\Gamma^1}(E) = 2,\ \chi_{\Gamma^1}(C_3) = -1,\ \chi_{\Gamma^1}(C_3^2) = -1,\ \chi_{\Gamma^1}(\sigma_v') = 0,\ \chi_{\Gamma^1}(\sigma_v'') = 0,\ \chi_{\Gamma^1}(\sigma_v''') = 0$$

and for the one-dimensional irreducible representation Γ^2 by

$$\chi_{\Gamma^2}(E) = 1,\ \chi_{\Gamma^2}(C_3) = 1,\ \chi_{\Gamma^2}(C_3^2) = 1,\ \chi_{\Gamma^2}(\sigma_v') = 1,\ \chi_{\Gamma^2}(\sigma_v'') = 1,\ \chi_{\Gamma^2}(\sigma_v''') = 1.$$

It is not accidental, that the characters for C_3 and C_3^2 and the characters for σ_v', σ_v'' and σ_v''' are equal for a given representation. This is because the operations C_3 and C_3^2 and the operations σ_v', σ_v'' and σ_v''' are conjugate to each other, respectively. Two operations R and S of a point group are conjugate to each other, if they are linked by a third operation X of the point group by the relation

$$R = X^{-1}SX \text{ or equivalent } S = XRX^{-1}.$$

Two conjugate operations have the same character for any representation. All operations of a given symmetry group, which are conjugate to each other are said to belong to one class. The C_{3v} group can be divided into three classes, one containing the operations C_3 and C_3^2, one containing σ_v', σ_v'' and σ_v''', and the third containing only E. One important result from group theory is that for a given point group the number of classes equals the number of non-equivalent irreducible representations. If g denotes the order of the group, i.e., the total number of operations, k the number of classes, g_i the number of operations in the i-th class and n_μ the dimension of the irreducible representation Γ_μ, the following equations hold true:

$$g = \sum_{i=1}^{k} g_i = \sum_{\mu=1}^{k} n_\mu^2. \tag{B.7}$$

The dimensions n_μ determine the degeneracies present in the system.

The characters of all the irreducible representations for all classes of symmetry operations are summarized in character tables. The character table for the C_{3v} point group is displayed in Table B.3. Since the identity operation is always represented by the identity matrix, the characters in the corresponding column (usually the first) equal the dimensions of the irreducible representation. Every point group contains the so-called *total symmetric irreducible representation.* Its basis functions do not change under all the symmetry operations. All characters of the total symmetric irreducible representation are equal to 1 (see the first row of Table B.3).

	E	$2C_3$	$3\sigma_v$	basis	
A_1	1	1	1	z	$x^2+y^2; z^2$
A_2	1	1	-1	R_z	
E	2	-1	0	(x,y); (R_x,R_y)	(x^2-y^2,xy); (xz,yz)

Table B.3: Character table for the C_{3v} point group, along with possible basis functions (R_z denotes an axial vector in z-direction).

The notation for the irreducible representations is based on R. S. Mulliken [138]. One dimensional irreducible representations are labeled either A or B according to whether the character of a rotation about the rotation axis of highest order is $+1$ or -1, respectively. Two-dimensional irreducible representations are labeled E, and three-dimensional representations can be labeled T or F. The former is more common in electronic problems and the latter in vibrational problems. If a point group contains the operation of inversion (i), a subscript g or u is added according to whether the character of i is positive or negative, respectively. If irreducible representations of the same type occur more than once, they are numbered in increasing order.

The importance of group theory for quantum mechanical systems is based in the fact that both, the electronic and the nuclear Hamiltonian, commute with the symmetry operators. Therefore, each of the eigenfunctions corresponds to one of the irreducible representations and the character table shows which symmetry types and degeneracies in principle exist. Furthermore, with the aid of the character table it is possible to determine whether certain integrals which involve eigenfunctions of the Hamiltonian do vanish or not.

The vibrational frequencies and modes of a molecule are determined by the dependency of the total energy from the mass weighted orthogonal displacements q_i from the equilibrium positions of the molecule. The matrices $D^0(R)$ which describe the transformation of the displacements q_i into q_i' under the symmetry operation R built a representation Γ^0 for the point group to which the molecule belongs. These matrices can be determined by

$$q_i' = \sum_{j=1}^{3N} D^0_{ij}(R) q_j, \quad i = 1, 2, \ldots, 3N.$$

If one chooses normal mode coordinates Q_i, the corresponding transformation matrices $D^n(R)$ are in block diagonal form

$$Q_i' = \sum_{j=1}^{3N} D^n_{ij}(R) Q_j, \quad i = 1, 2, \ldots, 3N$$

and each block corresponds to one of the irreducible representations of the point group of the molecule.

The reduction of

$$\Gamma^0 = a_1\Gamma^1 + a_2\Gamma^2 + \ldots + a_k\Gamma^k = \Gamma^{\text{vib}} + \Gamma^{\text{trans}} + \Gamma^{\text{rot}}$$

contains irreducible representations corresponding to the vibrational normal coordinates and to the translational and rotational normal coordinates, which have been summarized to Γ^{vib}, Γ^{trans} and Γ^{rot}, respectively. The a_μ determine how often an irreducible representation Γ^μ occurs in Γ^0. They can be obtained from the *decomposition rule*:

$$a_\mu = \frac{1}{g}\sum_{i=1}^{k} g_i \chi^0(C_i)\chi^\mu(C_i)^*, \quad \mu = 1, \ldots, k. \tag{B.8}$$

Since the characters $\chi^0(C_i)$ can be obtained from the summation over the diagonal elements of either the transformation matrices $D^0(C_i)$ or $D^n(C_i)$, only the atoms which stay fixed during the symmetry operation contribute to the character. How much a fixed atom contributes depends on the symmetry operation. The contributions per unmoved atom for the identity operation E, a rotation $C(\theta)$ about the angle θ, a reflection σ, a rotation-reflection $S(\theta)$ about the angle θ and the inversion operation i are given in Table B.4 [137].

C_i	E	$C(\theta)$	σ	$S(\theta)$	i
$\chi(C_i)$	3	$1 + 2\cos\theta$	1	$-1 + 2\cos\theta$	-3

Table B.4: Contributions of symmetry operations to group characters.

The irreducible representations corresponding to the translational and rotational degrees of freedom can be determined by looking at the behavior of a single vector indicating the translation and of a single axial vector (or pseudo-vector) indicating the rotation. The characters $\chi^{\text{trans}}(C_i)$ for the translational representation Γ^{trans} are the same as given above for the position vectors of the unmoved nuclei. The characters of Γ^{rot} are related to those of Γ^{trans} by

$$\begin{aligned}
\chi^{\text{rot}}\{E\} &= \chi^{\text{trans}}\{E\} \\
\chi^{\text{rot}}\{C(\theta)\} &= \chi^{\text{trans}}\{C(\theta)\} \\
\chi^{\text{rot}}\{\sigma\} &= -\chi^{\text{trans}}\{\sigma\} \\
\chi^{\text{rot}}\{S(\theta)\} &= -\chi^{\text{trans}}\{S(\theta)\} \\
\chi^{\text{rot}}\{i\} &= -\chi^{\text{trans}}\{i\}
\end{aligned}$$

For instance, a homo-nuclear cluster containing three atoms at the corners of an equilateral triangle and one atom above the center of the triangle has C_{3v} symmetry. During one of the two rotation operations C_3 or C_3^2 the atom above the center of the triangle is unmoved and the three other atoms change their positions. During one of the reflection operations the atom above the center and one atom at the triangles corner, which lies in the reflection plane, are unmoved. Of course the identity operation keeps all four atoms at their positions. With $\theta = 2\pi/3$ and therefore $\chi(C(\theta)) = 0$ one obtains the following characters for the different representations:

C_i	E	C_3	σ_v
$\chi^0(C_i)$	12	0	2
$\chi^{\text{trans}}(C_i)$	3	0	1
$\chi^{\text{rot}}(C_i)$	3	0	-1
$\chi^{\text{vib}}(C_i)$	6	0	2

and from the decomposition rule (B.8) the reductions

$$\begin{aligned}\Gamma^0 &= 3\Gamma^{A_1} + \Gamma^{A_2} + 4\Gamma^E \\ \Gamma^{\text{trans}} &= \Gamma^{A_1} + \Gamma^E \\ \Gamma^{\text{rot}} &= \Gamma^{A_2} + \Gamma^E \\ \Gamma^{\text{vib}} &= 2\Gamma^{A_1} + 2\Gamma^E.\end{aligned}$$

Consequently, there will be two non-degenerate modes, labeled A_1 and A_2, and two two-fold degenerated modes, labeled E. Four different vibrational frequencies can occur at maximum in the spectrum.

B.2 Selection rules in IR- and Raman-spectroscopy

For a quantum mechanical system the probability for a transition from an initial state described by the wave-function Ψ_i^σ to a final state described by Ψ_f^ρ is (under certain conditions) proportional to integrals of the form:

$$I_{\text{tr}} = \int d\mathbf{r}\Psi_i^\sigma(\mathbf{r})^* F^\lambda(\mathbf{r})\Psi_f^\rho(\mathbf{r}), \tag{B.9}$$

here the function F^λ depends on the physical operator which induces the transition, e.g., the electric dipole moment. Since the wavefunctions Ψ_i^σ and Ψ_f^ρ are eigenfunctions of the (nuclear or electronic) Hamiltonian, they form a basis for the irreducible representations Γ^σ and Γ^ρ. If the function F^λ belongs to a function space, which generates the irreducible representation Γ^λ the integrand,

$$\Psi_i^\sigma(\mathbf{r})^* F^\lambda(\mathbf{r})\Psi_f^\rho(\mathbf{r}),$$

is a basis function for the direct product representation $\Gamma^{\sigma *}\otimes\Gamma^\lambda\otimes\Gamma^\rho$. The reduction of this direct product representation

$$\Gamma^{\sigma *} \otimes \Gamma^\lambda \otimes \Gamma^\rho = a_\alpha\Gamma^\alpha + a_\beta\Gamma^\beta + \ldots + a_\omega\Gamma^\omega \tag{B.10}$$

shows which of the irreducible representations do occur (those with $a_i \neq 0$). The integrand can be expressed in terms of the basis functions f_i which generate the irreducible representations Γ^α, $\Gamma^\beta \ldots$, Γ^ω:

$$\Psi_i^\sigma(\mathbf{r})^* F^\lambda(\mathbf{r})\Psi_f^\rho(\mathbf{r}) = c_\alpha f^\alpha(\mathbf{r}) + c_\beta f^\beta(\mathbf{r}) + \ldots + c_\omega f^\omega(\mathbf{r}). \tag{B.11}$$

It can be shown, that the integral (B.9) vanishes until the reduction of the integrand contains the totally symmetric irreducible representation Γ^1 (for which all characters $\chi_{\Gamma^1}(R)$ are equal to 1 for all operations R). This is a sufficient, but not a necessary condition. For two irreducible representations Γ^σ and Γ^μ the totally symmetric representation Γ^1 appears in $\Gamma^{\sigma *} \otimes \Gamma^\mu$ only if $\sigma = \mu$, i.e. if the two irreducible representations are the same. This means also that the direct product of three irreducible representations $\Gamma^{\sigma *} \otimes \Gamma^\lambda \otimes \Gamma^\rho$ does not contain Γ^1, if the representation Γ^σ does not occur in the reduction of the direct product $\Gamma^\lambda \otimes \Gamma^\rho$, and then the integral (B.9) will vanish. From this the selection rules for IR and Raman spectra follow.

In the harmonic approximation the vibrational wavefunctions of a molecule with M atoms can be separated into:

$$\Psi_{n_1,\dots,n_{3M}}(Q_1,\dots,Q_{3M}) = \prod_{i=1}^{3M} \psi_{n_i}(Q_i), \tag{B.12}$$

where the ψ_{n_i} are the solutions for the one-dimensional harmonic oscillator given in (3.7). From the special form of the eigenfunctions of the harmonic oscillator and the related Hermite polynomials (3.9) it follows that the wavefunction corresponding to the vibrational ground state (where $n_1 = n_2 = \dots = n_{3M-6} = 0$) transforms like the totally symmetric representation Γ^1 and that the fundamental vibrational wavefunctions (where all quantum numbers n_i are zero except one) transform like the corresponding normal mode coordinate. Therefore, the probability for a transition from the vibrational ground-state Ψ_0^1 to a fundamental vibrational state Ψ_1^ρ, which is proportional to the integral

$$\int \Psi_0^1(Q) F^\lambda(Q) \Psi_1^\rho(Q),$$

vanishes until the fundamental vibrational wavefunction belongs to the same irreducible representation as the function F^λ, i.e. until $\Gamma^\rho = \Gamma^\lambda$.

Considering infrared spectroscopy, the transition is induced by the electric dipole-moment $\vec{p}$ and it is $F^\lambda(Q) = \vec{p}$. The electric dipole moment transforms exactly like a translational vector. From this it follows the selection rule for IR spectroscopy:

Only the vibrational modes which normal mode coordinates belong to the same irreducible group Γ^{trans} *as the translation coordinates can be IR active.*

For Raman spectroscopy the transition is induced by the polarizability tensor ($F^\lambda(Q) = \alpha$) defined by the six different components α_{xx}, α_{yy}, α_{zz}, α_{xy}, α_{xz} and α_{yz}. These components transform like the functions xx, yy, zz, xy, xz and yz. The selection rule for Raman spectroscopy reads:

Only the vibrational modes which normal mode coordinates belong to the same irreducible group Γ^α *as the functions* xx, yy, zz, xy, xz *and* yz *can be Raman active.*

Usually the irreducible representations, which are generated by the translational coordinates x, y and z along with the irreducible representations generated by xx, yy, zz, xy, xz and yz are especially labeled in the corresponding character table (see, e.g., Table B.3).

	E	C_2	$\sigma_v(xz)$	$\sigma_v(yz)$	basis	
A_1	1	1	1	1	z	$x^2; y^2; z^2$
A_2	1	1	-1	-1	R_z	xy
B_1	1	-1	1	-1	$x; R_y$	xz
B_2	1	-1	-1	1	$y; R_x$	yz

Table B.5: Character table for the C_{2v} point group, along with possible basis functions. The rotation axis is assumed to point in the z-direction (R_z denotes an axial vector in z-direction).

In a molecule or cluster with a center of inversion the characters of the irreducible representations corresponding to i in Γ^{trans} are -1 (are of u-type) and the ones contained in Γ^{α} are +1 (are of g-type). Since the representation Γ^{ρ} of the fundamental vibrational wavefunction can be only either of u-type or of g-type, no fundamental frequency for this cluster or molecule can be both, IR and Raman active.

How to identify the irreducible representation of a given mode and how to determine if the mode is IR or Raman active is illustrated for Si_3 in the following Section.

B.3 Si_3 as an example

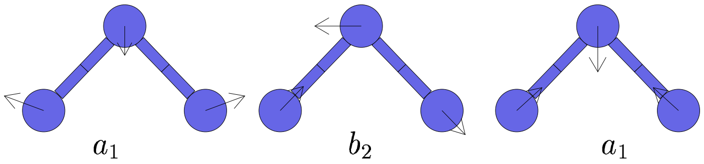

Figure B.1: Normal mode vectors $\vec{X}_i$ for an isosceles triangle (C_{2v}-symmetry). The paper-plane is identical to the y, z-plane.

The ground-state of Si_3 has C_{2v}-symmetry. The three vibrational modes of the isosceles triangle Si_3 are displayed in Fig. B.1. To identify the irreducible representation of the three vibrational modes one has to determine how the depicted eigenvectors transform under the operations of the symmetry group C_{2v}. The resulting characters have to be compared to the character table of the C_{2v} group in Tab. B.5.

The three operations of the C_{2v} point group, besides the identity operation E, are: (i) 180°-rotation about the z-axis, (ii) reflection at the x, z-plane and (iii) reflection at the y, z-plane. There is only one operation per class. The eigenvectors of the first normal mode (left picture in Fig. B.1) and of the third normal mode (right picture in Fig. B.1) do not change by performing any of the operations. Therefore, for each operation the corresponding character equals 1 and these two normal modes belong to the total symmetric irreducible representation A_1. The eigenvectors of the second normal mode do invert their direction by rotation about the z-axis and by reflection at the x, z-plane (perpendicular to the paper-plane). The eigenvectors do not change by reflection at the y, z-plane (identical to the paper-plane). It follows that the second normal mode yields the characters -1,-1 and 1 with respect to the operations C_2, $\sigma_v(xz)$ and $\sigma_v(yz)$ and belongs to the irreducible representation B_2.

Only the modes which belong to the same irreducible representation as the three (Cartesian) translation vectors $\hat{x}, \hat{y}$ and $\hat{z}$ can be IR active. Since the z-axis is chosen as rotation-axis, the vector $\hat{z}$ belongs to the totally symmetric irreducible representation A_1. The vector $\hat{x}$ belongs to B_1 and the vector $\hat{y}$ belongs to B_2. Therefore, all vibrational normal modes are IR-active. Since A_1 is an irreducible representation for the functions x^2, y^2 and z^2 and B_2 is an irreducible representation for the function yz (see Tab. B.5), all the vibrational normal modes are Raman-active, as well.

Appendix C

Model annealing curves

C.1 Transition state theory

The relationship between defect activation-energies and annealing-temperatures is established via the transition state theory. The probability that a system makes a transition from a state A to a state B separated by the energy difference $\Delta E = E_B - E_A$ is proportional to the Boltzmann factor $\exp(-\Delta E/(kT))$. $k = 8.617 \cdot 10^{-5}\,\mathrm{eV/\,K}$ is the Boltzmann constant. The annealing-rate μ is defined as the fraction of transitions $\Delta N/N$ during the time Δt:

$$\mu = \frac{\Delta N}{N \Delta t}.$$

At a given finite temperature T a typical vibrational mode of state A with frequency ν_0 is excited. The number of trials per time unit to make a transition to state B equals ν_0. If the transition from state A to state B requires N_j jumps, the annealing rate is reduced by a factor $1/N_j$. Therefore, the annealing rate is given by

$$\mu = \frac{\nu_0}{N_j} e^{\Delta S/k} e^{-\Delta E/(kT)}, \tag{C.1}$$

where $\exp(\Delta S/k)$ is the entropy-factor.

It is assumed that for the dissociation of a mono-vacancy from a vavancy cluster only 1 jump is required. A typical frequency for silicon systems is $\nu_0 = 6 \cdot 10^{12}/s$ which corresponds to about $1/\lambda_0 = 200\,\mathrm{cm}^{-1}$.

With the parameters

$$\begin{aligned} \nu_0 &= 6 \cdot 10^{12}/\,\mathrm{s}, \quad \text{typical frequency} \\ \Delta S &= 5 \cdot 10^{-4}\,\mathrm{eV/\,K}, \quad \text{entropy} \\ N_j &= 1, \quad \text{number of jumps} \\ \Delta t &= 30 \text{ min}, \quad \text{annealing time} \end{aligned}$$

the fraction of transitions after annealing with constant temperature T for 30 min is given by

$$\frac{\Delta N}{N} = 1800\,\mathrm{s}\ 6 \cdot 10^{12}/\,\mathrm{s}\ e^{5.8022}\ e^{-\Delta E/(kT)} = 3.575 \cdot 10^{18}\ e^{-\Delta E/(kT)}. \tag{C.2}$$

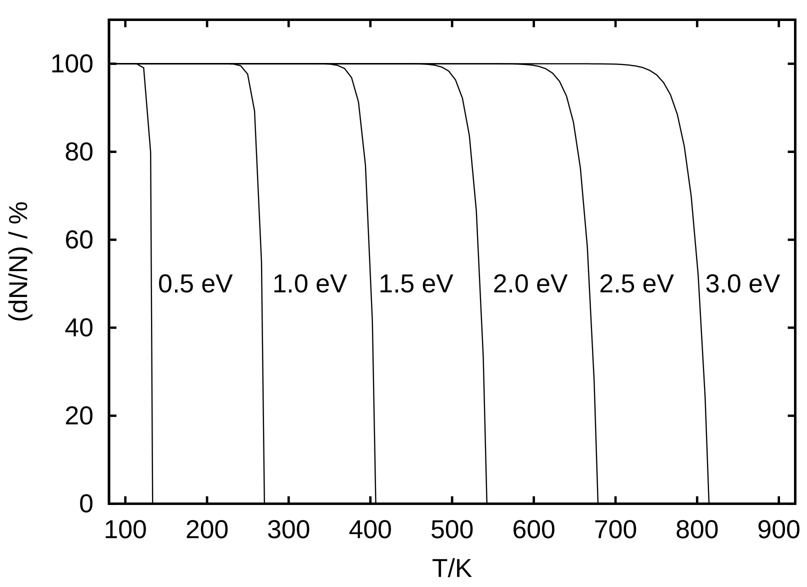

Figure C.1: Fraction of non-annealed defects after annealing with temperature T for 30 min. Plots are shown for different defect-energies from 0.5 eV to 3.0 eV.

This fraction as a function of temperature T is plotted for different energy differences ΔE and the parameters given above in Figure C.1.

The annealing temperature T_a is defined by $\Delta N/N = 1/2$. For several combinations of ΔE and fractions ν_0/N_j the corresponding annealing-temperatures are given in Table C.1. If, e.g., the typical frequency is 10 times lower and 10 times more jumps are required ($\nu_0 = 6 \cdot 10^{11}$, $N_j = 10$ instead of $\nu_0 = 6 \cdot 10^{12}$, $N_j = 1$) the annealing-temperatures are shifted by about 30 K/ eV.

	0.5 eV	1.0 eV	1.5 eV	2.0 eV	2.5 eV	3.0 eV
$6 \cdot 10^{12}$	133 K	267 K	400 K	534 K	667 K	801 K
$6 \cdot 10^{10}$	150 K	299 K	449 K	598 K	748 K	897 K

Table C.1: Annealing temperatures T_a for different combinations of ΔE (columns) and fractions ν_0/N_j (rows).

Bibliography

[1] M. Schulz. *Nature*, 399:729, 1999.

[2] S. Furukawa and T. Miyasato. *Phys. Rev. B*, 38:5726, 1988.

[3] A. Szabo and N. S. Ostlund. *Modern quantum chemistry: introduction to advanced electronic structure theory.* McGraw-Hill Publishing Company, New York, 1989.

[4] R. O. Jones and O. Gunnarson. The density functional formalism, its applications and prospects. *Rev. Mod. Phys.*, 61(3):689, 1989.

[5] C. Kittel. *Quantum Theory of Solids.* John Wiley & Sons, 2 edition, 1987.

[6] J. C. Slater. *Quantum Theory of Molecules and Solids, Vol. IV.* McGraw-Hill Publishing Company, New York, 1974.

[7] P. Hohenberg and W. Kohn. *Phys. Rev.*, 136:B864, 1964.

[8] W. Kohn and L. J. Sham. *Phys. Rev.*, 140:A1133, 1965.

[9] D. M. Ceperley and B. J. Alder. *Phys. Rev. Lett.*, 45:566, 1980.

[10] J. P. Perdew. *Electronic Structure of Solids '91.* Akademie Verlag, Berlin, 1991.

[11] J. P. Perdew K. Burke and M. Ernzerhof. *Phys. Rev. Lett.*, 77:3865, 1996.

[12] P. Pulay. *Adv. Chem. Phys.*, 69:241, 1987.

[13] G. Seifert, H. Eschrig, and W. Bieger. *Zeitschr. f. Phys. Chemie*, 267(3):529, 1986.

[14] W. M. Foulkes and R. Haydock. *Phys. Rev. B*, 39(17):12520, 1988.

[15] M. Elstner, D. Porezag, G. Jungnickel, J. Elsner, M. Haugk, Th. Frauenheim, S. Shuhai, and G. Seifert. A self-consistent-charge density-functional tight-binding method for simulations of complex material properties. *Phys. Rev. B*, 58(11):7260–7268, 1998.

[16] D. Porezag. *Development of Ab-Initio and Approximate Density Functional Methods and their Application to Complex Fullerene Systems.* PhD thesis, Technische Universität Chemnitz, Germany, 1997.

[17] D. Porezag, Th. Frauenheim, Th. Köhler, G. Seifert, and R. Kaschner. *Phys. Rev. B*, 51(19):12947, 1995.

[18] Th. Frauenheim, D. Porezag, M. Elstner, G. Jungnickel, J. Elsner, M. Haugk, and A. Sieck. An ab initio two-center tight-binding approach to simulations of complex materials properties. In P. E. A. Turchi A. Gonis and L. Colombo, editors, *Tight-Binding Approach to Computational Materials Science*, volume 491, page 91. MRS, 1998.

[19] Th. Frauenheim, F. Weich, Th. Köhler, S. Uhlmann, D. Porezag, and G. Seifert. *Phys. Rev. B*, 52(15):11492, 1995.

[20] A. Sieck, D. Porezag, Th. Frauenheim, M. R. Pederson, and K. Jackson. Structure and vibrational spectra of low-energy silicon clusters. *Phys. Rev. A*, 56(6):4890, 1997.

[21] A. Sieck. *Phys. Rev. B*, 2000. to be submitted.

[22] D. Porezag, Th. Frauenheim, Th. Köhler, G. Seifert, and R. Kaschner. Construction of tight-binding-like potentials on the basis of density-functional theory: Application to carbon. *Phys. Rev. B*, 51:12947, 1995.

[23] Th. Köhler, Th. Frauenheim, and G. Jungnickel. Stability, chemical bonding, and vibrational properties of amorphous carbon at different mass densities. *Phys. Rev. B*, 52:11837, 1995.

[24] R. Gutierrez, Th. Frauenheim, Th. Köhler, and G. Seifert. Stability of silicon carbide structures: from clusters to solid surfaces. *J. Mat. Chem.*, 6:1657, 1996.

[25] R. Gutierrez, M. Haugk, J. Elsner, G. Jungnickel, M. Elstner, A. Sieck, Th. Frauenheim, and D. Porezag. *Phys. Rev. B*, 60:1771, 1999.

[26] P. Deak, A. Gali, J. Miro, R. Gutierrez, A. Sieck, and Th. Frauenheim. Theoretical studies on defects in SiC. In G. Davis and M. H. Nazare, editors, *Proc. of the 19th Int. Conf. on Defects in Semiconductors*, pages 258–263, 739–744. Mater. Sci. Forum, 1997.

[27] P. Deak, A. Gali, J. Miro, R. Gutierrez, A. Sieck, and Th. Frauenheim. Theoretical studies on defects in SiC. In G. Pensl, H. Morkoc, B. Monemar, and E. Janzen, editors, *Silicon Carbide, III-Nitrides and Related Materials*, pages 279–282. Trans Tech, Switzerland, 1998.

[28] T.E.M. Staab, M. Haugk, Th. Frauenheim, and H.S. Leipner. Magic number vacancy clusters in GaAs — structure and positron lifetime studies. *Phys. Rev. Lett.*, 83(26):5519–5522, 1999.

[29] J. Elsner, R. Jones, M. I. Heggie, P. K. Sitch, M. Haugk, Th. Frauenheim, and S. Öberg. Deep acceptors trapped at threading edge dislocations in GaN. *Phys. Rev. B*, 58:12571, 1998.

[30] D. Steele. *Theory of Vibrational Spectroscopy.* W. B. Saunders Company, Philadelphia, 1971.

[31] E. C. Honea, A. Ogura, C. A. Murray, K. Raghavachari, W. O. Sprenger, M. F. Jarrold, and W. L. Brown. *Nature*, 366:42, 1993.

[32] K. Raghavachari and C. M. Rohlfing. *J. Chem. Phys.*, 89(4):2219, 1988.

[33] R. Fournier, S. B. Sinnott, and A. E. DePristo. *J. Chem. Phys.*, 97(6):4149, 1992.

[34] O. Cheshnovsky, S. H. Yang, C. L. Pettiette, M. J. Craycraft, Y. Liu, and R. E. Smalley. *Chem. Phys. Lett.*, 138:119, 1987.

[35] T. N. Kitsopoulos, C. J. Chick, A. Weaver, and D. M. Neumark. *J. Chem. Phys.*, 93:6108, 1990.

[36] S. Li, R. Z. Van Zee, W. Weltner, and K. Raghavachari. *Chem. Phys. Lett.*, 243:275, 1995.

[37] E. C. Honea, A. Ogura, D. R. Peale, C. Felix, C. A. Murray, K. Raghavachari, W. O. Sprenger, M. F. Jarrold, and W. L. Brown. *J. Chem. Phys.*, 110(24):12161, 1999.

[38] K. P. Huber and G. Herzberg. *Molecular Spectra and Molecular Structure. Constants of Diatomic Molecules*, volume 4. Van Nostrand-Reinhold, New York, 1979.

[39] L. Brewer. Lawrence berkeley laboratory report no. lbl-3720. unpublished.

[40] C. Chatillon, M. Allibert, and A. Pattoret. *C. R. Acad. Sci. Ser. C*, 280:1505, 1975.

[41] K. Jackson, M. R. Pederson, D. Porezag, Z. Hajnal, and Th. Frauenheim. *Phys. Rev. B*, 55:2549, 1996.

[42] C.C. Arnold and D. M. Neumark. *J. Chem. Phys.*, 99:3353, 1993.

[43] C. Xu, T.R. Taylor, G. R. Burton, and D. M. Neumark. *J. Chem. Phys.*, 108:1395, 1998.

[44] R. Kishi, H. Kawamata, Y. Negishi, S. Iwata, A. Nakajima, and K. Kaya. *J. Chem. Phys.*, 107:10029, 1997.

[45] W. Begemann, K. H. Meiwes-Broer, and H. O. Lutz. *Phys. Rev. Lett.*, 56:2248, 1986.

[46] Q. L. Zhang, Y. Liu, R. F. Curl, F. K. tittel, and R. E. Smalley. *J. Chem. Phys.*, 88:1670, 1988.

[47] M. F. Jarrold and E. C. Honea. *J. Phys. Chem.*, 95:9181, 1991.

[48] M. F. Jarrold and J. E. Bower. *J. Phys. Chem.*, 92:5702, 1988.

[49] M. F. Jarrold. *Science*, 252:1085, 1991.

[50] J. R. Heath, Y. Liu, C. O'Brien, Q. L. Zhang, R. F. Curl, F. K. Tittel, and R. E. Smalley. *J. Chem. Phys.*, 83:5520, 1985.

[51] K. Fuke, K. Tsukamoto, F. Misaizu, and M. Sanekata. *J. Chem. Phys.*, 99:7807, 1993.

[52] A. Marijnissen and J. J. ter Meulen. *Chem. Phys. Lett.*, 263:803, 1996.

[53] P. Ordejon, D. Lebedenko, and M. Menon. *Phys. Rev. B*, 50:5645, 1994.

[54] J. Harris. *Phys. Rev. B*, 31:1770, 1985.

[55] P. Ballone, W. Andreoni, R. Car, and M. Parrinello. *Phys. Rev. Lett.*, 60(4):271, 1988.

[56] D. J. Wales and M. C. Waterworth. *J. Chem. Soc. Faraday Trans.*, 88(23):3409, 1992.

[57] I. Vasiliev, S. Ögüt, and J. R. Chelikowsky. *Phys. Rev. Lett.*, 78(25):4805, 1997.

[58] I. Lee K. J. Chang and Y. H. Lee. *J. Phys.: Cond. Matter*, 6:741, 1994.

[59] C. M. Rohlfing and K. Raghavachari. *Chem. Phys. Lett.*, 167:559, 1990.

[60] B. Liu, Z. Y. Lu, B. Pan, C. Z. Wang, K. M. Ho, A. A. Shvartsburg, and M. F. Jarrold. *J. Chem. Phys.*, 109(21):9401, 1998.

[61] J. C. Grossman and L. Mitas. *Phys. Rev. B*, 52(23):16735, 1995.

[62] M. V. Ramakrishna and A. Bahel. *J. Chem. Phys.*, 104(24):9833, 1996.

[63] J. C. Grossman and L. Mitas. *Phys. Rev. Lett.*, 74(8):1323, 1995.

[64] U. Röthlisberger, W. Andreoni, and P. Giannozzi. *J. Chem. Phys.*, 92:1248, 1992.

[65] K. M. Ho, A. A. Shvartsburg, B. Pan, Z. Y. Lu, C. Z. Wang, J. G. Wacker, J. L. Fye, and M. F. Jarrold. *Nature*, 392:582, 1998.

[66] M. R. Pederson, K. Jackson, D. V. Porezag, Z. Hajnal, , and Th. Frauenheim. *Phys. Rev. B*, 54(4):2863, 1996.

[67] D. Porezag and M. R. Pederson. *Phys. Rev. B*, 54:7830, 1996.

[68] A. A. Quong, M. R. Pederson, and J. L. Feldman. *Solid State Commun.*, 87:535, 1993.

[69] R. Schäfer, S. Schlecht, J. Woenckhaus, and J. A. Becker. *Phys. Rev. Lett.*, 76:471, 1996.

[70] L. Ingber. Simulated annealing: Practice versus theory. *J. Math. Comput. Modelling*, 18(11):29, 1993.

[71] S. Kirkpatrick, C. D. Gelatt Jr., and M. P. Vecchi. Optimization by simulated annealing. *Science*, 220:671, 1983.

[72] P. J. M. van Laarhoven and E. H. L. Aarts. *Simulated Annealing: Theory and Applications.* D. Reidel, Dordrecht, The Netherlands, 1987.

[73] N. E. Collins, R. W. Egelese, and B. L. Golden. *Am. J. Math. Management Sci.*, 8(3 & 4):209, 1988.

[74] S. Geman and D. Geman. Stochastic relaxation, gibbs distribution and the bayesian restoration in images. *IEEE Trans. Patt. Anal. Mac. Int.*, 6(6):721, 1984.

[75] I. Rata, A. Shvartsburgh, M. Horoi, Th. Frauenheim, K. W. M. Siu, and K. A. Jackson. *to be published*, 2000.

[76] M. F. Jarrold and J. E. Bower. *J. Chem. Phys.*, 96:9180, 1992.

[77] M. F. Jarrold and V. A. Constant. *Phys. Rev. Lett.*, 67:2994, 1991.

[78] R. R. Hudgins, M. Imai, M. F. Jarrold, and P. Dugourd. *J. Chem. Phys.*, 111(17):7865, 1999.

[79] K. M. Creegan and M. F. Jarrold. *J. Am. Chem. Soc.*, 112:3768, 1990.

[80] J. M. Maruyama, L. R. Anderson, and R. E. Smalley. *J. Chem. Phys.*, 94:5349, 1990.

[81] J. M. Alford, R. T. Laaksonen, and R. E. Smalley. *J. Chem. Phys.*, 94:2618, 1991.

[82] J. R. Chelikowsky and N. Binggeli. Cluster assembled materials. volume 232. Materials Science Forum, Trans Tech Publications, 1996.

[83] R. Kishi, Y. Negishi, H. Kawamata, S. Iwata, A. Nakajima, and K. Kaya. *J. Chem. Phys.*, 108:8039, 1998.

[84] M. Woeller, M. Muhlhauser, S. D. Peyerimhoff, and F. Grein. *Chem. Phys. Lett.*, 288:603, 1998.

[85] E. J. Bylaska, P.R. Taylor, R. Kawai, and J. H. Weare. *J. Phys. Chem.*, 100:6966, 1996.

[86] J. M. L. Martin. *Chem. Phys. Lett.*, 255:1, 1996.

[87] L. Mitas, J. C. Grossman, I. Stich, and J. Tobik. *Phys. Rev. Lett.*, 84(7):1479, 2000.

[88] W. Fuhs, U. Holzhauer, S. Mantl, F.W. Richter, and R. Sturm. Annihilation of positrons in electron-irradiated silicon crystals. *phys. stat. sol. (b)*, 89:69–75, 1978.

[89] Motoko-Kwete, D. Segers, M. Dorikens, L. Dorikens-Vanpraet, P. Clauws, and I. Lemanhieu. Temperature characteristics of positron trapping at defects in electron-irradiated silicon. *Appl. Phys.* , A49(6):659–664, 1989.

[90] P.Mascher, S. Dannefaer, and D. Kerr. Positron trapping rates and their temperature dependencies in electron-irradiated silicon. *Phys. Rev. B*, 40(17):11764–11771, 1989.

[91] A. Polity, F. Börner, S. Huth, S. Eichler, and R. Krause-Rehberg. Defects in electron-irradiated Si studied by positron-lifetime spectroscopy. *Phys. Rev. B*, 58(7):10363–10377, 1998.

[92] Young-Hoon Lee and James W. Corbett. EPR studies in neutron-irradiated silicon: A negative charge state of a nonplanar five-vacancy cluster (V_5^-). *Phys. Rev. B*, 8(6):2810–2826, 1973.

[93] Young-Hoon Lee and James W. Corbett. EPR study of defects in neutron-irradiated silicon: Quenched-in allignment under $\langle 110\rangle$-uniaxial stress. *Phys. Rev. B*, 9(10):4351–4361, 1974.

[94] M. Huang, Y. Wang, J. Yang, Y. He, Y. Guo, and C. Liu. The study of neutron-irradiated Si by positron annihilation. *Mater. Sci. Forum*, 105-110:1071–1076, 1992.

[95] R. Krause-Rehberg, M. Brohl, H.S. Leipner, Th. Drost, A. Polity, U. Beyer, and H. Alexander. Defects in plastically deformed semiconductors studied by positron annihilation: Silicon and germanium. *Phys. Rev. B*, 47(20):13266–13275, 1993.

[96] T.Y. Tan, P. Plekhanov, and U.M. Gösele. Nucleation barrier of voids and dislocation loops in silicon. *Appl.Phys.Lett.*, 70(13):1715–1717, 1997.

[97] D.J. Chadi and K.J. Chang. Magic numbers for vacancy aggregation in crystalline Si. *Phys. Rev. B*, 38(2):1523–1525, 1988.

[98] H. Seong and L. J. Lewis. First-principles study of the structure and energetics of neutral divacancies in silicon. *Phys. Rev. B*, 53(15):9791, 1996.

[99] J.L. Hastings, S.K. Estreicher, and P.A. Fedders. Vacancy aggregates in silicon. *Phys. Rev. B*, 56(16):10215, 1997.

[100] M.J. Puska, S. Pöykkö, M. Pesola, and R.M. Nieminen. Convergence of supercell calculations for point defects in semiconductors: Vacancy in silicon. *Phys. Rev. B*, 58(3):1318–1325, 1998.

[101] S. Ögüt and J.R. Chelikowsky. Large pairing jahn-teller distortions around divacancies in crystalline silicon. *Phys. Rev. Lett.*, 83(19):3852–3855, 1999.

[102] A. Bongiorno, L. Colombo, and T. Diaz de la Rubia. Structural and binding properties of vacancy clusters in silicon. *Europhys. Lett.*, 43(6):695–700, 1998.

[103] Th. Frauenheim, F. Weich, Th. Köhler, S. Uhlmann, D. Porezag, and G. Seifert. Density-functional-based construction of transferable nonorthogonal tight-binding potentials for Si and SiH. *Phys. Rev. B*, 52(15):11492, 1995.

[104] SA. Seeger. *Appl. Phys.*, 4:183, 1974.

[105] W. Brandt. *Appl. Phys.*, 5:1, 1974.

[106] M.J. Puska and R.M. Nieminen. Defect spectroscopy with positrons: A general calculational method. *J.Phys.F: Metal Phys.*, 13:333–346, 1983.

[107] M.J. Puska, S. Mäkinen, M. Manninen, and R.M. Nieminen. Screening of positrons in semiconductors and insulators. *Phys. Rev. B*, 39(11):7666–7679, 1989.

[108] E. Bornonski and R.M. Nieminen. Electron-positron density functional theory. *Phys. Rev. B*, 34(6):3820–3831, 1986.

[109] M. Saito and A. Oshiyama. Lifetimes of positrons trapped at Si vacancies. *Phys. Rev. B*, 53(12):7810–7814, 1996.

[110] R. Krause-Rehberg and H.S. Leipner. *Defects in Semiconductors.* Springer Verlag, Berlin, Heidelberg, first edition, 1999.

[111] Zhu Shenyun, Li Anli, Li Donghong, Huang Hanchen, Zheng Shengnan, Du Hongshan, Ding Honglin, Gou Zhenhui, and T. Iwata. Positron annihilation and perturbed angular correlation studies of defects in neutron and heavy ion irradiated Si. *Mater. Sci. Forum*, 175-178:609–612, 1995.

[112] Motoko-Kwete, D. Segers, M. Dorikens, L. Dorikens-Vanpraet, P. Clauws, and I. Lemanhieu. Positron annihilation study of defects in electron irradiated silicon. In *Positron Annihilation Proccedings of the ICPA-8 Gent*, pages 687–689, Singapore, 1989. World Scientific.

[113] B. Somieski, T.E.M. Staab, and R. Krause-Rehberg. The data treatment influence on the spectra decomposition in positron lifetime spectroscopy; Part 1: On the interpretation of multi-component analysis studied by Monte-Carlo simulated model spectra. *Nucl.Instr. and Meth.*, A381:128–140, 1996.

[114] T.E.M. Staab, B. Somieski, and R. Krause-Rehberg. The data treatment influence on the spectra decomposition in positron lifetime spectroscopy; Part 2: The effect of source corrections. *Nucl.Instr. and Meth.*, A381:141–151, 1996.

[115] M. Brohl, C. Kisielowski, and H. Alexander. Pentavacancies in plastically deformed silicon. *Appl.Phys.Lett.*, 50(24):1733–1735, 1987.

[116] S. Dannefaer, G.W. Dean, D.P. Kerr, and B.G. Hogg. Influence of defects and temperature on the annihilation of positrons in neutron-irradiated silicon. *Phys. Rev. B*, 14(7):2709–2714, 1976.

[117] C.G. Hübner. PhD thesis, Mathematisch-Naturwissenschaftlich-Technische Fakultät der Martin-Luther Universität Halle-Wittenberg, Fr.-Bach-Platz 6, 06108 Halle/Saale, Germany, 1998.

[118] S. Dannefaer, D. Kerr, and B.G. Hogg. A study of defects in amorphous silicon films. *J. Appl. Phys.*, 54(1):155–160, 1983.

[119] T. E. M. Staab, A. Sieck, M. Haugk, M. J. Puska, Th. Frauenheim, and H. S. Leipner. Stability of large vacancy clusters in silicon. *Phys. Rev. B*, 2000. submitted.

[120] M. Haugk, J. Elsner, Th. Heine, Th. Frauenheim, and G. Seifert. *Comp. Mat. Sci.*, 13:239, 1999.

[121] A. Antonelli, E. Kaxiras, and D.J. Chadi. Vacancy in silicon revisited: Structure and pressure effects. *Phys. Rev. Lett.*, 81(10):2088, 1998.

[122] M. Pesola, J. von Boehm, S. Pöykkö, and R. M. Nieminen. Spin-density study of the silicon divacancy. *Phys. Rev. B*, 58(3):1106–1109, 1998.

[123] R. M. Nieminen and M. J. Puska. Vacancy defects in c-si: electronic and ionic structures. In R. Hull, editor, *Properties of Crystalline Silicon*, pages 309–, London, 1999. EMIS Datareviews Series No. 20.

[124] E. G. Song, E. Kim, Y. H. Lee, and Y. G. Hwang. *Phys. Rev. B*, 48:1486, 1993.

[125] S.K. Estreicher, J.L. Hastings, and P.A. Fedders. The ring-hexavacancy in silicon: A stable and inactive defect. *Appl. Phys. Lett.*, 70(4):432–434, 1997.

[126] M.J. Puska and C. Corbel. *Phys. Rev. B*, 38:9874, 1988.

[127] M. Hakala, M.J. Puska, and R.M. Niemienen. Momentum distributions of electron-positron pairs annihilating at vacancy clusters in si. *Phys. Rev. B*, 57(13):7621–7627, 1998.

[128] K. Jackson, G. Jungnickel, and Th. Frauenheim. *Chem. Phys. Lett.*, 292:235, 1998.

[129] K. Jackson and B. Nellermoe. *Chem. Phys. Lett.*, 254:249, 1996.

[130] H. Eschrig. *Optimized LCAO Method and the Electronic Structure of Extended Systems.* Akademie Verlag, Berlin, 1988.

[131] M. T. Yin and M. L. Cohen. *Phys. Rev. B*, 26(10):5668, 1982.

[132] *Data in Science and Technology: Semiconductors, Group IV Elements and III-V Compounds.* Springer-Verlag, Berlin Heidelber New York, 1991.

[133] J. C. Slater and G. F. Koster. Simplified LCAO method for the periodic potential problem. *Phys. Rev.*, 94(6):1498, 1954.

[134] W. D. Grobman and D. E. Eastman. *Phys. Rev. Lett.*, 29:1508, 1972.

[135] K. L. Shalee and R. E. Nohony. *Phys. Rev. Lett.*, 24:942, 1970.

[136] G. K. M. Thutupalli and S. G. Tomlin. *J. Phys. C*, 10:467, 1977.

[137] D. M. Bishop. *Group Theory and Chemistry.* Oxford, Clarendon Press, 1973.

[138] R. S. Mulliken. *J. Chem. Phys.*, 23:1997, 1955.

Danksagung

Ich möchte ganz herzlich allen danken, die mich beim Anfertigen dieser Dissertation unterstützt haben. Herrn Prof. Thomas Frauenheim danke ich für die nette Aufnahme in seine Arbeitsgruppe und für die sehr guten von ihm geschaffenen Rahmenbedingungen. Dr. Mark Pederson und Dr. Dirk Porezag danke ich für die gute Betreuung und Kooperation während meiner mehrmonatigen Forschungsaufenthalte am Naval Research Laboratory in Washington DC, USA. Die Zusammenarbeit mit Dr. Torsten Staab von der Technischen Universität Helsinki bzgl. der Leerstellencluster in Silizium war äußerst fruchtbar. Sehr wertvoll waren auch die zahlreichen Diskussionen mit Dr. habil. Gotthard Seifert (Uni-Paderborn), Prof. Koblar Alan Jackson (Central Michigan University, USA), Prof. Harald Overhof (Uni-Paderborn), Prof. Heinrich Marsmann (Uni-Paderborn) und Prof. Herbert Urbassek (Uni-Kaiserslautern).

Alle Gruppenmitglieder in Chemnitz und Paderborn haben durch Ihr Engagement und ihre Freundlichkeit die tägliche Arbeit sehr angenehm gemacht. Die intensive Zusammenarbeit mit Michael Haugk, Joachim Elsner, Paul Sitch und Rafael Gutierez war ergiebig und unterhaltsam zugleich. Insbesondere erwähnen möchte ich auch Thomas Köhler, Zoltan Hajnal, Michael Sternberg, Gerd Jungnickel, Eva Rauls, Alexander Blumenau, Marc Amkreutz, Uwe Gerstmann und Marcus Elstner. Von den genannten gebührt Michael Sternberg und Zoltan Hajnal besonderer Dank für die reibungslose und durchaus professionelle Administration der Computer, welche für diese Arbeit unerlässlich war.

Der Deutschen Forschungsgemeinschaft danke ich für die finanzielle Begleitung dieser Arbeit.

Nicht zuletzt gilt meinen Eltern besonderer Dank für die Unterstützung und Geduld, die sie mir entgegengebracht haben.